

**University of Alberta**

Quantification of Fugitive Emissions from a Biosolids Lagoon

by

Longdong Zhang

A thesis submitted to the Faculty of Graduate Studies and Research  
in partial fulfillment of requirements for degree of

Master of Science

Department of Civil and Environmental Engineering

© Longdong Zhang

Spring 2014

Edmonton, Alberta

Permission is hereby granted to the University of Alberta Libraries to reproduce single copies of this thesis and to lend or sell such copies for private, scholarly or scientific research purposes only. Where the thesis is converted to, or otherwise made available in digital form, the University of Alberta will advise potential users of the thesis of these terms.

The author reserves all other publication and other rights in association with the copyright in the thesis and, except as herein before provided, neither the thesis nor any substantial portion thereof may be printed or otherwise reproduced in any material form whatsoever without the author's prior written permission.

## **Dedication**

*To my wife, Yun Gao, love of my life*

## **Abstract**

Fugitive emissions of methane (CH<sub>4</sub>) and carbon dioxide (CO<sub>2</sub>) from a lagoon containing biosolids were continuously measured using an eddy covariance system for three months. Open Path Fourier Transform Infrared Spectrometry (OP-FTIR) was also used to quantify concentrations of methane and ammonia (NH<sub>3</sub>) at several locations along the lagoon edges for four days. Both eddy covariance and inverse dispersion (using a backward Lagrangian stochastic model–WindTrax) techniques were used to quantify fugitive emission fluxes of methane, carbon dioxide and/or ammonia. For the data obtained by the eddy covariance system, the relationships between concentrations/emission fluxes and temperature, wind speed, and wind direction were studied and certain trends were identified. While the predominant wind direction was not ideal for the sonic anemometer measurements, emission fluxes for methane simulated using inverse dispersion and eddy covariance techniques were consistent with each other for the same time periods.

## **Acknowledgements**

First and foremost, I sincerely thank my supervisor, Dr. Zaher Hashisho, who has supported and encouraged me greatly with his patience and knowledge. I would also like to offer my sincere gratitude to Dr. John D. Wilson and Casandra Brown for helping me in learning eddy covariance technique and micrometeorology. Thanks to Dr. Sunny Cho for her encouragement on this project. In addition, I thank Pooya Shariaty and Charlie Wang, as well as my other labmates for their help with the field work. Thanks to Mr. Steven Perry, Dr. Ram Hashmonay, Dr. Raymond Berard and others for their excellent technical support. Finally, thanks are due to Alberta Environment and Sustainable Resource Development for the funding support.

# Table of Contents

<b>Chapter 1 Introduction.....</b>	<b>1</b>
1.1 Background.....	1
1.2 Objectives of Research.....	4
1.3 Thesis Outline.....	5
<b>Chapter 2 Relevant Theory and Literature Review .....</b>	<b>6</b>
2.1 Atmospheric Boundary Layer .....	6
2.2 Monin-Obukhov Similarity Theory.....	7
2.3 Flux Measurement Techniques.....	10
2.3.1 Flux Chambers .....	10
2.3.2 Tracer Ratio Technique.....	13
2.3.3 Mass Balance Technique.....	14
2.3.4 Inverse Dispersion Technique.....	16
2.3.5 Flux Gradient Technique.....	18
2.3.6 Eddy Covariance Technique .....	20
2.3.7 Eddy Accumulation and Relaxed Eddy Accumulation.....	22
2.3.8 Radial Plume Mapping Technique.....	24
2.4 Flux Footprint.....	26
2.5 Literature Review .....	27

<b>Chapter 3 Methodology .....</b>	<b>29</b>
3.1    OP-FTIR.....	29
3.1.1    Instrumentation.....	29
3.1.2    Operating Procedure in Field .....	31
3.1.3    Data Processing Procedure.....	31
3.1.4    Quality Control/Assurance.....	32
3.2    Eddy Covariance System.....	32
3.2.1    Instrumentation.....	32
3.2.2    Post-measurement Data Processing Procedure .....	33
3.2.3    Quality Control/Assurance.....	34
<b>Chapter 4 Field Campaign at a Biosolids Lagoon.....</b>	<b>35</b>
4.1    Site Description .....	35
4.1.1    Instrument Deployment.....	35
4.1.2    Overview of Data Quality Filtering.....	38
4.1.3    Meteorological Observations .....	39
4.2    Concentrations from OP-FTIR.....	42
4.3    Concentrations from EC.....	50
4.3.1    Time Series of CH <sub>4</sub> Concentration Measurements .....	50
4.3.2    Time Series of CO <sub>2</sub> Concentration Measurements .....	53
4.3.3    Concentrations and Temperature .....	55

4.3.4	Concentrations and Wind Speed .....	57
4.3.5	Concentration Roses.....	58
4.4	Emission Fluxes Derived Using Inverse Dispersion .....	60
4.4.1	Input Parameters.....	60
4.4.2	Results .....	64
4.5	Emission Fluxes Derived Using EC .....	65
4.5.1	Time Series of CH <sub>4</sub> Emission flux .....	66
4.5.2	Time Series of CO <sub>2</sub> Emission flux .....	68
4.5.3	Emission Flux and Temperature .....	69
4.5.4	Emission Flux and Wind Speed .....	73
4.5.5	Emission flux and Wind Direction.....	76
4.5.6	Emission Flux and L <sub>90</sub> .....	80
4.5.7	L <sub>90</sub> and Wind Speed .....	84
4.5.8	L <sub>90</sub> and Wind Direction.....	88
4.5.9	50% Source Area.....	90
4.6	Limitations of the Measurement Techniques .....	91
<b>Chapter 5 Conclusions.....</b>		<b>93</b>
<b>References .....</b>		<b>95</b>
<b>Appendix A The Parameterized Scalar Flux-source Area Model.....</b>		<b>100</b>
<b>Appendix B Models Used for Calculating 90% Fetches.....</b>		<b>102</b>
<b>Appendix C OP-FTIR Operating Procedure in Field.....</b>		<b>104</b>

<b>Appendix D Steps for OP-FTIR Data Processing Using GRAMS/AI and RMMSoft.....</b>	<b>106</b>
<b>Appendix E Detailed Quality Control/Assurance Information for OP-FTIR .....</b>	<b>108</b>
<b>Appendix F VBA Code for Filtering Wind Directions and Removing “Errors” .....</b>	<b>110</b>
<b>Appendix G VBA Code for Calculating 50% Source .....</b>	<b>113</b>

## List of Tables

Table 4-1 Basic parameters of OP-FTIR during the OP-FTIR field campaign ....	37
Table 4-2 Distances of separation required by EddyPro.....	37
Table 4-3 Quantity and percentage of data points remained after each quality filtering .....	38
Table 4-4 Summary of CH <sub>4</sub> concentrations and meteorological conditions during the OP-FTIR field campaign .....	43
Table 4-5 Summary of NH <sub>3</sub> concentrations and meteorological conditions of the OP-FTIR field campaign .....	49
Table 4-6 Minimum, maximum and median concentrations of CH <sub>4</sub> and CO <sub>2</sub> measured by EC.....	50
Table 4-7 Meteorological conditions and concentrations of CH <sub>4</sub> and NH <sub>3</sub> as input parameters for the WindTrax simulations .....	62
Table 4-8 Emission fluxes/rates of CH <sub>4</sub> and NH <sub>3</sub> simulated using WindTrax... ..	65
Table 4-9 Overview of emission fluxes/rates of CH <sub>4</sub> and CO <sub>2</sub> calculated by EddyPro. ....	66
Table 4-10 Comparison of emission fluxes of CH <sub>4</sub> calculated by ID and EC techniques .....	80
Table 4-11 Calculated parameters using mini-FSAM model for estimating 50% source area for Day 3 of the OP-FTIR field campaign .....	91
Table 4-12 Medians of the calculated parameters for estimating 50% source area using mini-FSAM model for the whole EC field campaign.....	91

Table A-1 Values of parameters used for the passive scalar flux-source area model under unstable stratification in Schmid (1994).....	101
Table A-2 Values of parameters used for the passive scalar flux source area model under stable stratification in Schmid (1994) .....	101

## List of Figures

Figure 2-1 Illustration of Inverse Dispersion technique.....	17
Figure 3-1 Schematic of a mono-static configuration of OP-FTIR.....	29
Figure 4-1 The surrounding environment of the lagoon in study (Lagoon #1) and positions of OP-FTIR (Paths #1 to 5) and EC relative to the lagoon .....	36
Figure 4-2 The EC system mounted on a concrete jetty at Lagoon #1 .....	37
Figure 4-3 Windrose of filtered data during the EC field campaign.....	39
Figure 4-4 Time series of temperature measurements (filtered data). (A): full scale; (B): zoom in.....	41
Figure 4-5 Variation of normalized standard deviation of vertical velocity ( $\sigma_w/u_*$ ) plotted against stability ( $ z/L $ ) (log10 scale; for unstable conditions).....	42
Figure 4-6 Time series of methane concentrations measured using OP-FTIR at upwind side (west side) of the lagoon on Day 1 of the OP-FTIR field campaign.....	45
Figure 4-7 Time series of methane concentrations measured using OP-FTIR at both upwind (west) and downwind (east) on Day 3.....	45
Figure 4-8 Time series of methane concentrations measured using OP-FTIR at both upwind (south) and downwind (north) on Day 4 .....	46
Figure 4-9 Time series of methane concentrations measured using OP-FTIR close to EC system on Day 5 .....	46
Figure 4-10 Time series of NH <sub>3</sub> concentrations measured using OP-FTIR at upwind side (west side) on Day 1.....	47

Figure 4-11 Time series of ammonia concentrations measured using OP-FTIR at both upwind (west) and downwind (east) on Day 3.....	47
Figure 4-12 Time series of ammonia concentrations measured using OP-FTIR at both upwind (south) and downwind (north) sides on Day 4 .....	48
Figure 4-13 Time series of ammonia concentrations measured using OP-FTIR close to EC system on Day 5 of the OP-FTIR field campaign.....	48
Figure 4-14 Time series of CH <sub>4</sub> concentration measurements (filtered data). (A): full scale; (B): zoom in .....	51
Figure 4-15 Comparison of methane concentrations measured by OP-FTIR and EC on Day 5 of the OP-FTIR field campaign .....	53
Figure 4-16 Typical work flow of OP-FTIR during the field campaign.....	53
Figure 4-17 Time series of CO <sub>2</sub> concentration measurements (filtered data). (A): full scale; (B): zoom in .....	55
Figure 4-18 Concentrations of CH <sub>4</sub> plotted against temperature (filtered data) ...	56
Figure 4-19 Concentrations of CO <sub>2</sub> plotted against temperature (filtered data) ...	56
Figure 4-20 Concentrations of CH <sub>4</sub> plotted against wind speed (filtered data). (A): full scale; (B): zoom in .....	57
Figure 4-21 CO <sub>2</sub> concentrations plotted against wind speed (filtered data). (A): full scale; (B): zoom in .....	58
Figure 4-22 CH <sub>4</sub> concentration rose (filtered data). Color indicates CH <sub>4</sub> concentration in ppmv, wedges correspond to wind direction .....	59
Figure 4-23 CO <sub>2</sub> concentration rose (filtered data). Color indicates CO <sub>2</sub> concentration in ppmv, wedges correspond to wind direction .....	60

Figure 4-24 A screenshot of the WindTrax simulating fluxes at the lagoons.....	63
Figure 4-25 Time series of CH <sub>4</sub> emission (filtered data). (A): full scale; (B): zoom in.....	67
Figure 4-26 Time series of CH <sub>4</sub> emission (filtered data). (A): full scale; (B): zoom in.....	69
Figure 4-27 CH <sub>4</sub> emission fluxes potted against temperature (filtered data). (A): full scale; (B): zoom in.....	71
Figure 4-28 CO <sub>2</sub> emission fluxes plotted against temperature (filtered data). (A): full scale; (B): zoom in.....	72
Figure 4-29 Emission fluxes of CH <sub>4</sub> plotted against wind speed (filtered data). (A): full scale; (B): zoom in.....	74
Figure 4-30 Emission fluxes of CO <sub>2</sub> plotted against wind speed (filtered data). (A): full scale; (B): zoom in.....	75
Figure 4-31 Vertical wind speed standard deviation plotted against mean horizontal wind speed (filtered data).....	76
Figure 4-32 Emission flux of CH <sub>4</sub> plotted against wind direction (filtered data). (A): full scale; (B): zoom in.....	78
Figure 4-33 Emission flux of CO <sub>2</sub> plotted again wind direction (filtered data). (A): full scale; (B): zoom in.....	79
Figure 4-34 Emission Flux of CH <sub>4</sub> plotted against L <sub>90</sub> (filtered data). (A): full scale; (B): zoom in.....	82
Figure 4-35 Emission flux of CO <sub>2</sub> plotted against L <sub>90</sub> (filtered data). (A): full scale; (B): zoom in.....	83

Figure 4-36 $L_{90}$ calculated by EddyPro plotted against $u$ (filtered data). (A): full scale; (B): zoom in.....	85
Figure 4-37 $u$ plotted against $z_m/L$ (filtered data) .....	86
Figure 4-38 $L_{90}$ calculated by EddyPro plotted against $z_m/L$ (filtered data). (A): full scale; (B): zoom in.....	87
Figure 4-39 Schematic of $L_{90}$ and wind directions at certain conditions.....	89
Figure 4-40 $L_{90}$ rose (filtered data) .....	89
Figure 4-41 Schematic representation of the 50% source area for the average of Day 3 of OP-FTIR field campaign and for the median of the whole EC field campaign (filtered data) .....	91
Figure F-1 A screenshot of an EddyPro output document.....	112
Figure G-1 A screenshot of the layout of the data for calculating 50% source area.....	115

## List of Symbols

$a$	Distance to downwind edge of isopleth
$A$	Absorption of infra-red
$A_r$	Area bounded by isopleth
ABL	Atmospheric boundary layer
$A_{fc}$	Area covered by a flux chamber
bLS	Backward Lagrangian Stochastic
$c_p$	Specific heat at constant pressure
$C_{z,down}$	Concentration of trace gas at height $z$ on downwind boundary
$C_{z,up}$	Concentration of trace gas at height $z$ on upwind boundary
$C_{in}$	Concentration at the inlet of a flux chamber
$C_{m-b}$	Measured concentration minus background concentration
$C_{out}$	Concentration at the outlet of a flux chamber
$C_{up}$	Updraft concentration of gas of interest
$C_{down}$	Downdraft concentration of gas of interest
$d$	Maximum width of isopleth
$e$	Distance to upwind edge of isopleth
EC	Eddy covariance
$f$	Flux footprint
$F(x,y,z)$	Spatial distribution of surface fluxes
$F^{ea}$	Flux by eddy accumulation technique
$F^{fc}$	Flux by flux chamber technique

$F^{\text{fg}}$	Vertical flux of the gas of interest at height $z$
$F^{\text{mb}}$	Surface flux in the emitting region in mass balance technique
$F^{\text{rec}}$	Flux by relaxed eddy covariance
$F_{h,z}$	Mean horizontal flux at height $z$
GHGs	Greenhouse gases
LLGHGs	Long lived greenhouse gases
$H_0$	Sensible heat flux at surface
$I$	Measured intensity of infra-red light
$I_0$	Background intensity of infra-red light
ID	Inverse dispersion
$K_c$	Turbulent diffusivity
$K_h$	Diffusivity of heat
$K_m$	Diffusivity of momentum
$K_v$	von Karman constant = 0.4
$L$	Obukhov length
$L_{90}$	Distance upwind from EC system to the footprint contour that encompasses an area of surface that contributes 90% of the measured flux
MOST	Monin-Obukhov similarity theory
$n$	Dimensionless quantity in inverse dispersion technique
$n^t$	Dimensionless quantity calculated theoretically in inverse dispersion technique
$N_p$	Total number of particles released from sensor

OP-FTIR	Open path Fourier transform infra-red
PIC	Path integrated concentration
Q	Emission flux
$Q^{id}$	Emission flux in inverse dispersion technique
$Q_{net}$	Net emission flux in mass balance technique
$Q^{tr}$	Emission flux in tracer ratio technique
$Q_t$	Emission flux of tracer
R	Air flow rate in flow-through flux chamber
RSD	Relative standard deviation
SBM	Synthetic background method
$T_0$	Mean temperature
u	Longitudinal wind speed
$\bar{u}$	Mean horizontal wind speed
$u_z$	Horizontal wind speed measured at height z
$u^*$	Friction velocity
v	Latitude wind speed
V	Volume of the head space of a flux chamber
VRPM	Vertical radial plume mapping
w	Vertical wind speed
$w_0$	Vertical touchdown velocity
Y	The distance traversed by wind in mass balance technique
z	Measurement height
Z	Top of a gas plume in mass balance technique

$z_0$	Surface roughness
$\alpha$	Absorbance coefficient
$\beta$	Wind direction
$\delta$	Depth of the boundary layer
$\varepsilon$	Coefficient in relaxed eddy accumulation technique
$\zeta$	Stability parameter $z/L$
$\varphi$	Similarity function related to $z/L$
$\phi_m, \phi_h, \text{ and } \phi_c$	Universal stability functions of momentum, heat and concentration
$\psi$	Similarity function related to $\varphi$
$\rho$	Air density
$\sigma$	Standard deviation
$\tau_0$	Surface stress

# Chapter 1 Introduction

## 1.1 Background

The increasing concentration of greenhouse gases (GHGs) is claimed as the dominant factor in the radiative forcing of climate in the industrial era (IPCC 2007). CH<sub>4</sub> and CO<sub>2</sub>, classified as long-lived greenhouse gases (LLGHGs), are the two most significant contributors to global warming (Yusuf et al. 2012). These two LLGHGs are chemically stable and have a lifetime on the order of a decade to centuries or even longer. As a result, the emissions of CH<sub>4</sub> and CO<sub>2</sub> can impact the climate for a long term (IPCC 2007). Globally, the concentration of CH<sub>4</sub> has more than doubled since the pre-industrial level and reached over 1.75 parts per million (ppmv) recently (Amstel et al. 2010). Currently, ground level methane concentrations over Edmonton, Alberta, Canada (mid- to high-latitude northern hemisphere) are reported to be at around 1.9 ppmv (Mahzabin 2012). In the last decade, the global concentration of CO<sub>2</sub> has increased to over 390 ppmv at a rate of 2 ppmv/yr (Franks et al. 2013), which is faster than 1.4 ppmv/yr for 1960-2005 since continuous direct atmospheric measurements began (IPCC 2007). Although the concentration of CH<sub>4</sub> is much lower than that of CO<sub>2</sub>, the global warming potential (GWP) is 25 times that of CO<sub>2</sub> (IPCC 2007). In addition, increasing CH<sub>4</sub> emissions can decrease the concentration of hydroxyl radical (OH) and thus the overall oxidizing capacity of the troposphere. Therefore, the removal of CH<sub>4</sub> will slow down, followed by the building up of CH<sub>4</sub> concentration. So, it is important

to mitigate both CH<sub>4</sub> and CO<sub>2</sub> in order to stay below the 2 °C target of global warming (Kirschke et al. 2013).

Major natural sources of CH<sub>4</sub> include wetlands, fires, as well as geologic processes. Fossil fuel combustion and agriculture are the most significant anthropogenic sources of CH<sub>4</sub> (U.S. EPA 2010). It is stated that over 60% of total CH<sub>4</sub> emissions are from human activities globally (U.S. EPA 2010). For CO<sub>2</sub>, fossil fuel use is the most important source followed by deforestation and decay of biomass, etc. (IPCC 2007a).

NH<sub>3</sub> is a colorless, chemically active gas with a pungent smell. It is the most abundant alkaline component in the atmosphere (Asman et al. 1998). Ammonium (NH<sub>4</sub><sup>+</sup>), a reaction product of NH<sub>3</sub>, is a major component of atmospheric aerosols and precipitation (Asman et al. 1998, Sommer and Hutchings 2001). Ammonium nitrate (NH<sub>4</sub>NO<sub>3</sub>) and ammonium sulfates (NH<sub>4</sub>HSO<sub>4</sub> and [NH<sub>4</sub>]<sub>2</sub>SO<sub>4</sub>) are important components of airborne fine particulate matter (PM<sub>2.5</sub>). In addition, they are contributors to impaired visibility and regional haze (Battye et al. 2003). Since NH<sub>3</sub> was included in the UN Convention on Long-range Transboundary Air Pollution to Abate Acidification, Eutrophication and Ground-level Ozone in 1999, emissions of NH<sub>3</sub> have been limited by legislation (Sommer and Hutchings 2001). Although NH<sub>3</sub> has a short residence time of less than 5 days in the atmosphere and thus is limited to the near surrounding, ammonium aerosols can travel and deposit at larger distances with a longer lifetime in the order of 10 days (Aneja et al. 2001, Warneck 1999).

Globally, domestic animal wastes are major sources of  $\text{NH}_3$  emission (Asman et al. 1998, Battye et al. 2003). In Canada, 501 kilotonnes (kt) of  $\text{NH}_3$  were emitted in 2011 with an increase of 8% compared to the emissions in 2010 (Environment Canada 2013). Of the total  $\text{NH}_3$  emissions in Canada in 2011, 91% were from agricultural activities. Other emission sources of  $\text{NH}_3$  include but are not limited to transportation and industrial activities (Environment Canada 2013).

Biosolids, which contain nutrient-rich organic matter, are a by-product of domestic wastewater treatment. It is reported that 2.5% of U.S.  $\text{CH}_4$  emissions are from wastewater treatment (U.S. EPA 2012). Of the total emissions related to wastewater treatment, biosolids treatment and end use account for up to 40% (Brown et al. 2010). Meanwhile, a significant amount of  $\text{NH}_3$  is claimed to be emitted from biosolids lagoons (Aneja et al. 2008). In the City of Edmonton, biosolids in Clover Bar Biosolids Lagoons are generated by Gold Bar Wastewater Treatment Plant and the Alberta Capital Region Wastewater Commission (City of Edmonton 2013). An average of 25,230 dry tonnes is reported to be produced by the two wastewater treatment plants. The content of  $\text{NH}_3$  nitrogen is stated as 21,000 mg/kg on average (City of Edmonton 2013). In a previous study, the Inverse Dispersion technique (ID) and Eddy Covariance (EC) technique have been demonstrated to be feasible for quantifying  $\text{CH}_4$  emissions from Biosolids lagoons in short term (about one week) field campaigns in Clover Bar area (Brown 2013, Mahzabin 2012). Concentration of  $\text{CH}_4$  at the biosolids lagoons is reported to be as high as 10.9 ppmv measured by EC instruments (Brown 2013).

In addition, it is reported that Open Path Fourier Transform Infrared Spectrometer (OP-FTIR) has been employed in quantifying CH<sub>4</sub> and NH<sub>3</sub> at water-holding structures in swine farms and a dairy production facility (Aneja et al. 2008, Bjerneberg et al. 2009). Thus, it would be of interest to quantify emissions of CH<sub>4</sub> and CO<sub>2</sub> off the biosolids lagoons for a longer term (a few months) using a EC system. Once the EC system is installed, it requires minimum maintenance for the system to keep working. Therefore, OP-FTIR can be deployed for measuring CH<sub>4</sub> and NH<sub>3</sub> for comparison whenever resources and weather permit during the EC field campaign.

## **1.2 Objectives of Research**

This thesis focuses on the application of micrometeorological techniques for quantifying the emissions of methane (CH<sub>4</sub>), carbon dioxide (CO<sub>2</sub>) and ammonia (NH<sub>3</sub>) from a biosolids lagoon. The major objective of this research is to quantify the emission fluxes of CH<sub>4</sub> and CO<sub>2</sub> using the EC technique. Concentrations of CH<sub>4</sub> and CO<sub>2</sub> as well as necessary meteorological data are recorded for three months. The data recorded will be filtered to remove those collected with non-acceptable optical signal strength and/or at non-favorable wind directions. Filtered data will be processed using EddyPro Version 4 (LI-COR, Inc.) to get the emission fluxes. With a few months' measurements, possible relationships between concentrations or emission fluxes and typical meteorological observations including temperature, mean horizontal wind speed ( $\bar{u}$ ), wind direction ( $\beta$ ) are likely to be identified. In addition, the emission fluxes calculated

could be statistically meaningful with data under various meteorological conditions.

The second objective of this research is to use OP-FTIR to measure CH<sub>4</sub> and NH<sub>3</sub> at different locations along the biosolids lagoon to collect upwind and downwind concentration data when resources and weather permit. WindTrax 2.0 (Thunder Beach Scientific), a backward Lagrangian stochastic-based (bLS) model, was used to process the path integrated concentrations (PICs) along with the meteorological data collected by the EC system to simulate the emission fluxes. Emission fluxes derived by the two techniques will be compared.

### **1.3 Thesis Outline**

Chapter 1 provides background information on emissions of CH<sub>4</sub>, CO<sub>2</sub> and NH<sub>3</sub> in general as well as emissions from the biosolids lagoons in particular. The second Chapter summarizes the relevant theory employed by this thesis in calculating emission fluxes followed by a brief literature review of emissions from biosolids lagoons and applications of EC and OP-FTIR. The methodology of this research project is described in Chapter 3. Chapter 4 provides detailed information on the major work of this study including site description, time series of concentrations and emission fluxes, as well as the relationship between concentrations/emission fluxes and typical meteorological measurements. Finally, in Chapter 5, conclusions are presented based on the information provided in previous Chapters.

## **Chapter 2    Relevant Theory and Literature Review**

### **2.1    Atmospheric Boundary Layer**

The atmospheric boundary layer (ABL), which responds to surface forcings of mass and energy exchanges with a timescale of about an hour or less, is the lowest part (up to a couple kilometers) of the troposphere (up to an average altitude of 11 km) directly above the Earth's surface (Stull 1988). In the ABL where we live, horizontal transport is dominated by the mean wind and vertical by the turbulence (or eddies), which can result in rapid diffusion of constituents emitted at or near the surface throughout the ABL. The atmosphere in the ABL is almost always turbulent (Lenschow 2012). Turbulence is generally caused by mechanical disruption of wind moving past vegetation or structures (mechanical turbulence), or, due to the heating and cooling of air near the Earth's surface (buoyant turbulence) (Turner 1970). The chaotic fluctuations over a broad range of scales and the diffusiveness are used to define the characteristics of turbulence (Lenschow 2012). However, due to the randomness and the broad range of scales of the turbulence, statistical averages of fluctuations are often necessary to describe the processes in the ABL. Usually, the advection terms for flat and uniform plains are small enough to be negligible and thus horizontal homogeneity can be assumed. In addition, for most applications the processes in the ABL can be treated as sequences of steady states so that time averages of measurements can be used to describe the properties of the processes. With these two simplifications,

fluid dynamical theories and empirical laws based on wind tunnel studies can be applied to the ABL (Kaimal and Finnigan 1994).

The lowest 10% (about 50 m to 100 m) of the ABL is called the surface layer. In the surface layer, the turbulent fluxes and stress can be considered effectively height-independent, with variations of less than 10% of their magnitude (Stull 1988). The flow in the surface layer is determined primarily by surface friction and the vertical gradient of temperature (Kaimal and Finnigan 1994). The assumptions of horizontal homogeneity and steady state are more defensible in the surface layer of the ABL than the rest of the ABL (Kaimal and Finnigan 1994). The Monin-Obukhov Similarity Theory (MOST), which will be presented in the following Section, is widely used to describe the mean flow and turbulence statistics of the surface layer.

## **2.2 Monin-Obukhov Similarity Theory**

Similarity theory involves combining variables into dimensionless groups, conducting experiments to obtain values for each variable in the dimensionless group, as well as fitting the dimensionless group, as a function of some parameters with an empirical equation (Jacobson 2005). The process is called similarity theory as the equations determined from repeated experiments are similar to those from the first experiment. The MOST allows us to generalize profiles of mean and turbulent characteristics and thereby to model the air dispersion of pollutants (Hewitt and Jackson 2009). MOST is applicable when  $z_0$

$\ll z \ll \delta$ , where  $z$  is the height above the surface,  $z_0$  is the surface roughness length, and  $\delta$  is the depth of the surface layer. Only four (4) independent variables govern the mean flow and turbulence characteristics in a horizontally homogeneous surface layer Arya (2001). These four variables are:

- $z$ : the height above the surface
- $\tau_0/\rho$ : the surface drag;
- $H_0/\rho c_p$ : the surface kinematic heat flux and
- $g/T_0$ : the buoyancy variable

where  $\tau_0$  is magnitude of the mean surface stress,  $\rho$  is the air density,  $T_0$  is the mean temperature of the surface layer,  $H_0$  is the sensible heat flux at the surface, and  $c_p$  is the specific heat at constant pressure.

Based on Buckingham's theorem, the four independent variables given above can be formulated to only one independent dimensionless combination, the stability parameter:

$$\zeta = z/L \quad \text{Equation 2-1}$$

where  $L$  is the Obukhov length defined as:

$$L = \frac{-u_*^3}{k_v \left(\frac{g}{T_0}\right) \overline{w'T'}} \quad \text{Equation 2-2}$$

where  $k_v = 0.4$  is the von Karman constant.

The stability parameter  $\zeta$  is negative under unstable conditions, near zero under neutral conditions and positive under stable conditions. The effects of the wind

shear near surface usually dominate and the buoyancy effects are insignificant in the lowest part of surface layer where  $z \ll |L|$ . In contrast, the effects of the buoyancy may become dominant over shear-generated turbulence for  $z \gg |L|$ . In essence, the ratio  $z/L$  is an important indicator of the relative importance of buoyancy versus shear effects in the stratified surface layer (Arya 2001).

In the MOST, the following characteristic scales of length, velocity, and temperature are employed to form dimensionless groups:

- Length scales:  $z$  and  $L$
- Velocity scale:  $\sqrt[4]{\overline{u'w'^2} + \overline{v'w'^2}}$ , which defines the friction velocity ( $u_*$ )
- Turbulent temperature scale:  $T_* = -Q_H/\rho C_p u_*$

Based the MOST hypothesis, if normalized by an appropriate combination of the scales given above, the similarity prediction is that any mean flow or average turbulence quantity in the surface layer must be a unique function of the stability parameter ( $z/L$ ) only. Therefore, many similarity relations can be derived for a variety of dependent variables of interest. For example, the dimensionless wind shear can be expressed as:

$$\frac{k_v z}{u_*} \frac{\partial \bar{u}}{\partial z} = \varphi\left(\frac{z}{L}\right) \quad \text{Equation 2-3}$$

If the Equation 2-3 is integrated with respect to the height  $z$ , the velocity profiles can be derived as:

$$\bar{u}(z) = \frac{u_*}{k_v} \left[ \ln \frac{z}{z_0} - \psi_m\left(\frac{z}{L}\right) + \psi_m\left(\frac{z_0}{L}\right) \right] \quad \text{Equation 2-4}$$

where  $\psi_m$  is the similarity function related to  $\varphi_m$ :

$$(A) \quad \psi_m = 2 \ln \left( \frac{1+\varphi_m^{-1}}{2} \right) + \ln \left( \frac{1+\varphi_m^{-2}}{2} \right) + 2 \arctan(\varphi_m^{-1}) + \frac{\pi}{2} \quad \text{Equation 2-5}$$

(for  $L \leq 0$ )

$$(B) \quad \psi_m = 1 + 5 z/L \quad (\text{for } L \geq 0)$$

MOST is used in the software WindTrax for calculations of wind speed, temperature, and turbulence using inverse dispersion technique. More details will be presented in Section 2.3.4. Note that MOST relationships are not accurate at extreme stabilities and low winds (Flesch et al. 2005). It is suggested that when  $u^* \geq 0.15$  m/s and  $|L| \geq 10$ , the horizontally homogeneous surface layer is well described (Flesch et al. 2007).

## 2.3 Flux Measurement Techniques

The basic theory, applicability, advantages and limitations of various flux measurement techniques are summarized in this Section. Selection of flux measurement techniques should be based on site specific conditions (e.g. size, topography, meteorological conditions, etc.) and instruments available.

### 2.3.1 Flux Chambers

Flux chamber techniques, with measurement scale of the order of  $1 \text{ m}^2$ , are the most widely used method for quantifying trace gas fluxes. The trace gases are trapped by flux chambers as they leave the soil surface so that the changes in concentrations of the trace gases can be magnified (Denmead 2008). Flux

chambers can be classified as flow-through or closed chambers, depending on whether or not the flux chambers are open to the atmosphere.

In a flow-through chamber, outside air is fed through the head space of the chamber at a constant flow rate and the difference in concentration between the air at the inlet and outlet of the chamber is determined. The flux ( $\text{kg/m}^2\text{-s}$ ,  $F^{fc}$ ) of the trace gas is then calculated Equation 2-6 given below.

$$F^{fc} = R(C_{out} - C_{in})/A_{fc} \quad \text{Equation 2-6}$$

where  $R$  is the air flow rate ( $\text{m}^3/\text{s}$ ),  $C_{out}$  ( $\text{kg/m}^3$ ) is the gas concentration at the outlet of the chamber,  $C_{in}$  ( $\text{kg/m}^3$ ) is the gas concentration at the inlet of the chamber, and  $A_{fc}$  ( $\text{m}^2$ ) is the surface area (of order of  $1 \text{ m}^2$ ) covered by the flux chamber.

Where applicable, flow-through chambers are favourable as the increase in concentration of trace gases above background levels can be controlled by the air flow rate  $R$ , especially for larger fluxes (Denmead 2008).

In a closed chamber, the trace gas concentrations increase gradually as there is no or very small replacement of air in the head space. The rate of increase of the concentration is monitored and the flux can then be determined as

$$F^{fc} = \left(\frac{V}{A}\right) \frac{dC}{dt} \quad \text{Equation 2-7}$$

where  $F^c$  and  $A$  were defined previously,  $C$  ( $\text{kg/m}^3$ ) is the concentration of the trace gas in the head space,  $V$  ( $\text{m}^3$ ) is the volume of the head space and  $t$  (s) is time.

Closed chambers are more popular than flow-through chambers as closed chambers usually are simpler and allow easier detection due to larger concentration changes in the headspace of the chambers. A closed chamber can be static or dynamic. For the static chamber configuration, air samples need to be taken from the headspace periodically using a gas syringe. The samples are measured later in a laboratory. For the dynamic chamber configuration, air is circulated in a closed loop between the head space and a gas analyzer so that the change of the trace gas concentration can be monitored and any inhibition of the flux can be detected during the building up of the concentrations in the headspace.

The advantages of flux chambers include (Denmead 2008):

- The operating principle is simple
- Highly sensitive: can detect smaller fluxes than typically can be determined by other means
- Flexible and portable
- No power supply is required for static configuration
- Cost is low.

The limitations of flux chambers are summarized as follows (Denmead 2008):

- Increasing gas concentrations may inhibit fluxes, especially for closed chambers
- Pressure differences between the air inside and outside of a chamber can create artifact gas fluxes
- Results from flux chambers may not reflect the spatial and temporal variability in trace gas fluxes.

### 2.3.2 Tracer Ratio Technique

The tracer ratio technique was developed in the 1990s to measure CH<sub>4</sub> emissions from natural gas systems (Allen et al. 2013, Lamb et al. 1995). In the tracer gas technique, a tracer gas such as sulfur hexafluoride is released at the upwind edge of an emission source to simulate the CH<sub>4</sub> emissions. A mobile analyzer system can be used to measure both the CH<sub>4</sub> and tracer plumes downwind of the emission source in real-time, in addition to traditional canister sampling method (Czepiel et al. 1996, Hashisho et al. 2012). The background concentrations upwind of the emission source should also be determined. The CH<sub>4</sub> emission rate ( $Q^{tr}$ , kg/hour) can then be calculated using Equation 2-8.

$$Q^{tr} = Q_t \frac{C_{m-b}}{C_t} \quad \text{Equation 2-8}$$

where  $Q_t$  is the measured release rate of the tracer,  $C_{m-b}$  is the measured concentration of CH<sub>4</sub> minus the background concentration of CH<sub>4</sub> and  $C_t$  is the measured concentration of the tracer.

The advantages of the tracer ratio technique include:

- No meteorological measurements or dispersion modeling is involved (Lamb et al. 1995)
- Vertical profile of gas concentrations is not necessary (Griffith et al. 2008, Hashisho et al. 2012)

The limitations of the tracer ratio technique include (Czepiel et al. 1996):

- Spatial distribution of the tracer source must adequately resemble that of the naturally emitted gas whose emission rate is to be determined
- The downwind concentration should be significantly higher (more than 50 ppbv) than the background concentration
- Restricted to situations without interfering sources
- Adequate mixing of the tracer gas with the target gas (or sufficient downwind distance of measurement) in stable conditions is required

### 2.3.3 Mass Balance Technique

In the mass balance technique, the mean horizontal flux  $F_{h,z}$  (kg/m<sup>2</sup>/s) of emitted gas at any height  $z$  on a downwind boundary equals the difference between the production rate of a gas in a control volume and the rate of the gas being carried out of the control volume (see Equation 2-9).

$$F_{h,z} = \overline{u_z(C_{z,down} - C_{g,uz,up})} \quad \text{Equation 2-9}$$

where  $u_z$  (m/s) is the horizontal wind speed at height  $z$ , and  $C_{z,down}$  and  $C_{z,up}$  are the concentrations of the gas at  $z$  on downwind and upwind boundaries. The overbar denotes an average of time.

The net emission rate  $Q_{net}$  (kg/m/s) across a plane of unit width on the downwind boundary can be determined as

$$Q_{net} = \int_0^Z u_z (C_{z,down} - C_{g,uz,up}) dz \quad \text{Equation 2-10}$$

where  $Z$  is the top of the gas plume.

The height of the gas plume  $Z$  depends on atmospheric stability  $L$  and the distance traversed by the wind  $Y$ . The surface flux in the emitting region  $F^{mb}$  (kg/m<sup>2</sup>-s) is determined by Equation 2-11.

$$F^{mb} = Q_{net}/Y \quad \text{Equation 2-11}$$

In practice,  $\overline{uC_g}$  is hard to measure and thereby  $\overline{u} \overline{C_g}$  (i.e. the flux carried by the mean wind) is used for estimating horizontal flux instead. If slow response anemometers and gas sensors are used, the estimated horizontal flux should be reduced by 10% or 15% (Denmead 2008). Otherwise, fast response anemometers and gas sensors (such as an EC system) should be employed.

The advantages of mass balance technique are summarized as follows:

- Can be suitable for measuring both homogeneous and heterogeneous emission sources (Denmead 2008, Park et al. 2010)
- The underlying theory and the required instrumentation are simple (Denmead 2008, Hashisho et al. 2012).

The mass balance technique has limitations including (Denmead 2008):

- Only appropriate for small, well defined source areas with small background concentration outside the emitting area of interest
- There is some uncertainty about correction (10% or 15%) of the estimated horizontal flux. However, no correction is necessary if fast-response instrumentation is used.

#### 2.3.4 Inverse Dispersion Technique

The Inverse Dispersion (ID) technique relates emission flux  $Q^{id}$  ( $\text{kg}/\text{m}^2\text{-s}$ ) to mean horizontal wind speed  $u$  and a measured mean concentration  $c$  of the gas of interest. The ratio of the product of  $u$  and  $c$  to the emission flux  $Q^{id}$  of the source equals to a dimensionless quantity  $n$ ,

$$n \equiv \frac{uc}{Q^{id}} \quad \text{Equation 2-12}$$

The dimensionless quantity  $n$  can be calculated theoretically as  $n^t$ . The backward Lagrangian stochastic (bLS) model incorporated in the software WindTrax determines  $n^t$  by calculating the trajectories of an ensemble of released particles backward-time from the sensor to the source area. If a trajectory contacts the surface of the source area, then a touchdown (see Figure 2-1) is recorded in a catalog. With this catalog, Equation 2-13 can be used to compute  $n^t$ .

$$n = n^t \equiv \frac{1}{N_p} \sum \left| \frac{2u_z}{w_0} \right| \quad \text{Equation 2-13}$$

where  $N_p$  is the total number of particles released from the sensor, the summation is the touchdowns within the boundaries of the source,  $w_0$  is the vertical touchdown velocity,  $u_z$  the horizontal wind speed measured at height  $z$  and is used to normalize  $w_0$ . Once  $n'$  is obtained, the flux  $Q^{id}$  can be calculated using Equation 2-13 as discussed above. More information about the ID technique and the software WindTrax can be found in Section 4.4.1.

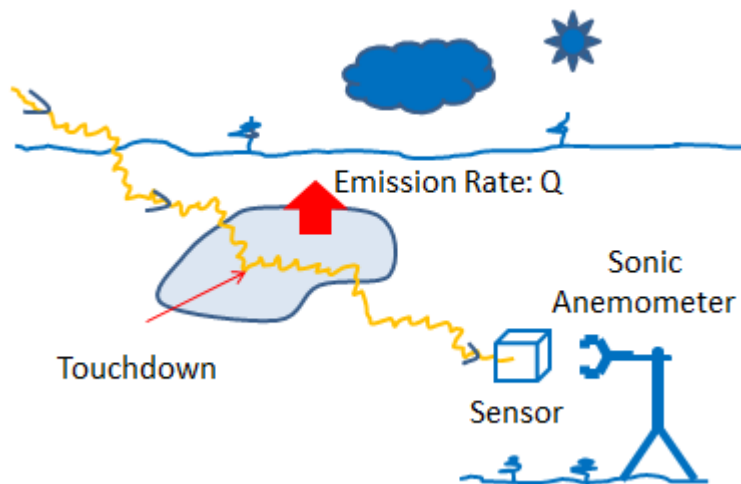


Figure 2-1 Illustration of Inverse Dispersion technique

Note: Figure 2-1 is inspired by the teaching of Atmospheric Boundary Layer by Dr. John D. Wilson.

The advantages of ID technique include:

- Only one observation of the horizontal wind speed and gas concentration is necessary
- Slow response sensors can be used (Flesch et al. 1995).

The limitations of ID technique include:

- Assumptions should be met: the air flow is horizontally homogeneous (Flesch et al. 1995)
- Best suited for small, well-defined source area of any shape (Denmead 2008).

### 2.3.5 Flux Gradient Technique

According to Laubach and Kelliher (2004), the similarity theory (K-theory) is the fundamental of flux gradient technique. In flux gradient technique, fluxes are related to the vertical gradient of the concentration of the gas of interest via a turbulent diffusivity,  $K_c$  (refer to Equation 2-14).

$$F^{fg} = -K_c \frac{\partial C}{\partial z} \quad \text{Equation 2-14}$$

where  $F^{fg}$  is the vertical flux of the gas of interest at height  $z$ .  $K_c$  needs to be estimated. Under neutral conditions, the diffusivities of momentum ( $K_m$ ), heat ( $K_h$ ), and passive tracers ( $K_c$ ) are equal to each other ( $K_m=K_h=K_c$ ) (Dyer and Bradley 1982). Under stable or unstable conditions, universal stability functions ( $\phi_m$ ,  $\phi_h$  and  $\phi_c$ ), as functions of the stability parameter  $z/L$ , can be used to express the diffusivities. In addition, Dyer and Bradley (1982) suggests that  $\phi_h = \phi_c$  ( $K_c = K_h$ ) at all stabilities. Then,  $K_c$  can be inferred by using the diffusivity of another variable ( $K_h$  or  $K_m$ ) for which flux and gradient can both be measured. If temperature flux and temperature gradient are to be used,  $K_c$  can be determined as

$$K_c = K_h = -F_T \left( \frac{\partial T}{\partial z} \right)^{-1} \quad \text{Equation 2-15}$$

where  $F_T$  is the temperature flux measured by the sonic anemometer,  $\frac{\partial T}{\partial z}$  is the temperature gradient determined by the thermocouple profile. Alternatively, the common parameterization for the momentum diffusivity can be used to determine  $K_c$ .

$$K_m = k_v u_* z \phi_m^{-1} \quad \text{Equation 2-16}$$

where  $k_v = 0.4$  is the von Karman constant and  $u_*$  the friction velocity. Equation 2-16 can be converted to Equation 2-17 by utilizing the universal stability functions.

$$K_c = K_h = \frac{k_v u_* z}{\phi_c \left( \frac{z}{L} \right)} \quad \text{Equation 2-17}$$

where  $k_v = 0.4$  is von Karman constant as stated before,  $\frac{\Delta C}{\Delta z}$  is used to approximate  $\frac{\partial C}{\partial z}$  in Equation 2-14.  $\frac{\Delta C}{\Delta z}$  is determined using mean concentrations measured at two heights.

The advantages of flux gradient technique (Denmead 2008):

- Can be applicable to smaller area:  $1 \times 10^4$  to  $2 \times 10^4$  m<sup>2</sup> without the necessity of mounting the instrument at large heights that are (therefore) affected by a large area spreading far upwind
- Slow response instrumentation can be used
- More reliable under conditions with dew, fog or precipitation without using 3-D sonic anemometer (compared to the Eddy Covariance to be introduced as follows)
- Can use long tube lengths for tall vegetation situations.

The limitations of flux gradient technique (Denmead 2008):

- May be limited to the inertial sub-layer above the heights of about twice the canopy height
- Interchange gear may be necessary to measure concentrations at different heights with the same instrument
- Buffering volumes may be needed to damp out fluctuations in gas concentration
- Emitting surface should be uniform so that instruments at different heights can have qualitatively the same footprints.

### 2.3.6 Eddy Covariance Technique

The Eddy Covariance (EC) technique is one of the most direct and defensible methods to measure fluxes. The general principle for EC technique is to measure the number of molecules moving upward and downward over time, as well as the travelling speeds of these molecules (Burba 2013). Key assumptions of EC technique are that the flow is:

- Horizontally homogeneous: the statistical properties do not vary horizontally; this is generally valid for a uniform flat terrain in the surface layer
- Steady state: the statistical properties of the flow do not change over time; this is generally valid for a time averaging period (e.g. 15 min or 30 min)

The mean vertical flux  $F^{ec}$  (kg/m<sup>2</sup>-s) can then be calculated using Equation 2-18.

$$F^{ec} = \overline{\rho_a w' c'} \quad \text{Equation 2-18}$$

where  $\overline{\rho_a}$  is the mean density of air,  $w'$  is the fluctuation of vertical wind speed,  $c'$  is the fluctuation of the gas concentration. Major corrections, which can be easily done by the software EddyPro, to the results calculated by Equation 2-18 are summarized as follows (Burba 2013):

- Frequency response errors caused by sensor separation, system time response, etc.
- Density fluctuation (WPL) due to the change of water vapor concentration and temperature
- Coordinate rotation is also necessary as sonic anemometers cannot be leveled ideally in field
- Other corrections.

The advantages of EC technique include (Burba 2013):

- A direct measurement, gives the vertical flux at the point of measurement
- Independent of atmospheric stability
- Can measure half-hourly or hourly averaged fluxes of a source area, continuously in years with minor down days and nights; this is a great advantage over other techniques.

The limitations of EC technique include (Burba 2013):

- The key assumptions discussed above should be valid

- At low wind speeds (<1 m/s) during nights, other mechanisms (e.g. molecular diffusion, advection, etc.) of mass transport may not be negligible when compared to turbulence transport
- Requires fast response sensors that can detect very small changes (e.g. concentrations and wind speeds)
- The upwind source area should be large enough for the 90% fetch ( $L_{90}$ ) of the EC system to be representative of the source area (see more information in Section 2.4).

### 2.3.7 Eddy Accumulation and Relaxed Eddy Accumulation

The eddy accumulation technique was developed by Desjardins et al. (1984) as a variant of the EC technique described in Section 2.3.6. Unlike the EC technique, the eddy accumulation system allows the use of either fast or slow response gas analyzers. However, fast response anemometers are still necessary for determining vertical wind velocities (Denmead 2008). Based on the sign (positive or negative) of the vertical wind velocity, the air in the measuring zone of an anemometer is drawn into one of the two accumulators for updrafts (positive  $w$ ) and downdrafts (negative  $w$ ), respectively (Baker et al. 1992). To accomplish this, a fast response solenoid valve is required to direct the air into the right accumulator at a flow rate proportional to  $w$ . For each sampling period, the updraft or downdraft trace gas concentration is measured and thereby the flux  $F^{ea}$  ( $\text{kg/m}^2\text{-day}$ ) can be determined using Equation 2-19 (Denmead 2008).

$$\overline{F^{ea}} = \overline{w_{up}C_{up}} - \overline{w_{down}C_{down}} \quad \text{Equation 2-19}$$

where  $w_{up}$  and  $w_{down}$  are vertical wind speed for updrafts and downdrafts, respectively;  $C_{up}$  and  $C_{down}$  are the concentrations of the trace gas associated with updrafts and downdrafts, respectively.

In the relaxed eddy accumulation method, the requirement of sampling at rates proportional to vertical wind velocity discussed above is relaxed by sampling at a fixed flow rate (Baker et al. 1992). By doing so, the relaxed eddy accumulation method is theoretically and technically easier to apply (Denmead 2008). The flux  $F^{rec}$  (kg/m<sup>2</sup>-day) can be obtained using Equation 2-20.

$$\overline{F^{rec}} = \varepsilon \sigma_w (\overline{C_{up}} - \overline{C_{down}}) \quad \text{Equation 2-20}$$

where,  $\varepsilon$  is a coefficient  $\cong 0.56$  (Denmead 2008, Wyngaard and Moeng 1992),  $\sigma_w$  is the standard deviation of  $w$ ,  $C_{up}$  and  $C_{down}$  are defined before.

The advantages of eddy accumulation and relaxed eddy accumulation:

- Provides direct measurements of trace gas flux with/without fast response gas sensors (Baker et al. 1992, Denmead 2008)
- Gas samples can be measure either online or offline with high precision instrument (Denmead 2008)
- For offline measurements, gas samples can be pre-conditioned to eliminate the effects of heat and water vapour on the flux results (Denmead 2008).

The limitations of eddy accumulation and relaxed eddy accumulation:

- Theoretically and technically difficult to sample at flow rates proportionally to vertical wind speed for eddy accumulation technique (Baker et al. 1992)
- High requirement of the measurements of vertical wind speed (Denmead 2008)
- Sampling line in front of the switching solenoid valve may introduce errors (Baker et al. 1992)

### 2.3.8 Radial Plume Mapping Technique

The radial plume mapping technique is a recently developed U.S. EPA test method (OTM 10) for characterizing emissions from area and fugitive sources (Hashmonay et al. 2008). An open path, path-integrated ORS system is employed to identify “hot spots” of emissions and quantify emission fluxes. In OTM 10, three methodologies are described for different uses:

- The horizontal radial plume mapping: used for mapping gas concentrations in a horizontal plane. Hot spots near the ground can be located
- The vertical radial plume mapping (VRPM): designed to determine the emission flux of contaminants in a vertical plane downwind from an emission source
- The one-dimensional radial plume mapping: suitable for obtaining the profile of pollutant concentrations along a line-of-sight (e.g. fence line of an industrial site)

The VRPM involves a downwind vertical scanning plane, in which five beams (or more) or three beams are used to measure the emission flux directly (Hashmonay et al. 2008). For each configuration, the ORS instrument sequentially scans the path determining components (i.e. retroreflectors) located either on the ground or elevated on a vertical structure to determine the spatial distribution of the gas plume in crosswind direction (Hashmonay et al. 2008). Gaussian mathematical functions are used to retrieve the concentration profiles of the vertical plane (Hashisho et al. 2012). Combined with wind speed and direction information, the emission flux can then be calculated directly (Hashmonay et al. 2008).

The advantages of radial plume mapping technique:

- Can be used to characterize fugitive emissions from large area sources (Hashisho et al. 2012, Hashmonay et al. 2008)
- Three dimensional profiles of gases of interest can be obtained (Hashisho et al. 2012)

The limitations of radial plume mapping technique:

- Not suitable for point emission sources (Hashisho et al. 2012)
- The system is expensive and complicated; substantial training and experience required (Hashisho et al. 2012, Hashmonay et al. 2008)

## 2.4 Flux Footprint

The flux footprint, defined as the contribution (per unit surface flux) of each elemental unit of the upwind surface area to the measured vertical flux of a trace gas, should be calculated for fluxes estimated by micrometeorological technique (Horst 1999). The flux footprint  $f$  relates the vertical flux determined at height  $z_m$ ,  $F(x,y,z = z_m)$ , to the spatial distribution of surface fluxes,  $F(x,y,z = 0) \equiv F_0(x,y)$  (Horst 1999).

$$F(x,y,z_m) = \int_{-\infty}^{\infty} \int_{-\infty}^x F_0(x',y') f(x-x',y-y',z_m) dx' dy' \quad \text{Equation 2-21}$$

where  $x-x'$  is the separation between the measurement point and the elemental unit of the upwind surface area in along-wind direction, and  $y-y'$  is the separation between the measurement point and the element unit of the upwind surface area in cross-wind direction.

The degree of the contribution discussed above varies with the distance of the elemental unit of the upwind area, the measurement height, as well as with the characteristics of the turbulent boundary layer and atmospheric stability (Schuepp et al. 1990). A parameterized model is described by Schmid (1994) to calculate the 50% source area (the area responsible for 50% of the surface influence). In the model, the maximum source location, the near and far end of the source area, and its maximum lateral extension can be determined, as well as the dimensions of the bounding isopleth of the 50% source area (Schmid 1994). Details of the model are given in Appendix A. Kljun et al. (2004) and Kormann and Meixner (2001) present models to calculate the  $L_{90}$ , the upwind distance required for the measured

flux to represent 90% of the flux generated by the whole surface area (Burba 2013). Details of the models are provided in Appendix B.

## **2.5 Literature Review**

Only a few studies were found to be directly related to biosolids lagoons, EC system, and OP-FTIR. The identified studies are summarized as follows.

Three open path infrared lasers were used by Mahzabin (2012) to study the practicalities of implementing bLS for about 3 days to quantify methane emissions from a biosolids lagoon in addition to other source areas. The three lasers were placed around the biosolids lagoon to determine the background concentration of CH<sub>4</sub>, the influence of the surrounding lagoons, as well as the emission flux of the NE lagoon. Results showed that the emission fluxes of CH<sub>4</sub> ranged from  $1.4 \times 10^{-2}$  kg/m<sup>2</sup>-day to  $1.9 \times 10^{-2}$  kg/m<sup>2</sup>-day. Brown (2013) used an EC system to quantify the emission fluxes of CH<sub>4</sub> and CO<sub>2</sub> of the biosolids lagoon studied in this thesis for about 9 days as a pilot study before another field campaign at an oil sands tailings ponds. During this period, data was recorded only 43% of the time as a result of power loss or non-ideal conditions. The median values of the CH<sub>4</sub> and CO<sub>2</sub> emission fluxes were  $7.8 \times 10^{-3}$  kg/m<sup>2</sup>-day and  $2.4 \times 10^{-2}$  kg/m<sup>2</sup>-day, respectively. In addition, an open-path infrared laser gas detector and the bLS model incorporated in WindTrax were also employed to determine the emission flux of CH<sub>4</sub>. The bLS results for two data periods on two

days showed CH<sub>4</sub> emission fluxes of  $-4.0 \times 10^{-3}$  kg/m<sup>2</sup>-day and  $9.5 \times 10^{-3}$  kg/m<sup>2</sup>-day, respectively.

Aneja et al. (2008) and Rumsey (2004) measured the NH<sub>3</sub> fluxes from water-holding structures at full-scale swine facilities for two two-week-long periods in two different seasons. A flow-through dynamic chamber system and two sets of OP-FTIRs were employed for evaluating environmentally superior technologies for waste treatment. Results showed that the fluxes of NH<sub>3</sub> from two biosolids lagoons were  $2.72 \times 10^{-3}$  kg/(m<sup>2</sup>-day) and  $4.36 \times 10^{-3}$  kg/(m<sup>2</sup>-day), respectively. Zahn et al. (2001) employed the theoretical profile shape method specified by Wilson et al. (1982) to quantify the fluxes of NH<sub>4</sub> and H<sub>2</sub>S among other trace gases for evaluating polymer biocovers in abating H<sub>2</sub>S and NH<sub>3</sub> from a swine lagoon. For an untreated (no polymer biocovers used) lagoon, the emission fluxes of CH<sub>4</sub> and NH<sub>3</sub> were reported to be 0.1 kg/m<sup>2</sup>-day and  $1.6 \times 10^{-2}$  kg/m<sup>2</sup>-day, respectively. Rose (2003) measured the emission concentrations of NH<sub>3</sub> from two dairy lagoons using an isolation flux chamber in August 2002 and January 2003. A chemiluminescence analyzer housed in a mobile laboratory was used to determine the concentrations of NH<sub>3</sub>. The emission fluxes were estimated to be  $3.4 \times 10^{-4}$  kg/m<sup>2</sup>-day and  $3.7 \times 10^{-4}$  kg/m<sup>2</sup>-day for the 1<sup>st</sup> and 2<sup>nd</sup> lagoon in the summer, respectively;  $5.2 \times 10^{-5}$  kg/m<sup>2</sup>-day and  $8.6 \times 10^{-6}$  kg/m<sup>2</sup>-day in the winter, respectively.

## Chapter 3 Methodology

### 3.1 OP-FTIR

#### 3.1.1 Instrumentation

A monostatic OP-FTIR (RAM2000 G2; KASSAY FSI, ITT Corp., Mohrsville, PA, USA) was used in this study to measure concentrations of CH<sub>4</sub> and NH<sub>3</sub>. The roles of the fundamental components (shown in Figure 3-1) of the OP-FTIR system used are summarized as below. More detailed description of OP-FTIR instrumentation can be found in Russwurm and Childers (2002) and U.S. EPA (1999).

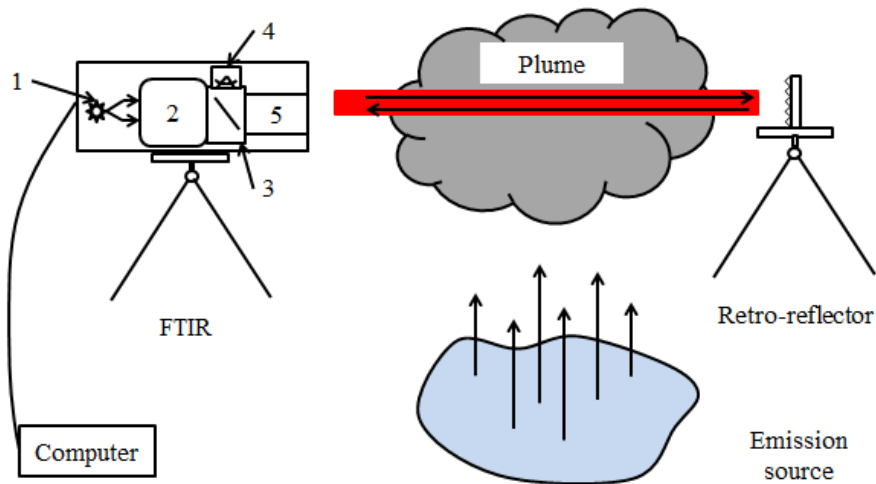


Figure 3-1 Schematic of a mono-static configuration of OP-FTIR

Note: 1: IR source; 2: interferometer; 3: beamsplitter; 4: detector and 5: telescope.

**IR source:** the IR source is a heated element that operates at around 1200 °C, which can emit enough energy to support an open path of up to 1 km in length.

**Transfer Optics:** Transfer optics are not shown in Figure 3-1, however, all of the currently available OP-FTIR systems are equipped with a set of transfer optics. These transfer optics work to collimate the IR beam before it goes through the interferometer and then refocus the beam coming out of the interferometer at the focal point of the transmitting/receiving optics.

**ZnSe Beam-splitters:** beam-splitters guide the emitting or returning IR beam to the detector. Meanwhile, beam-splitters also divert 50% of the IR energy to the instrument housing.

**Interferometer:** a Michelson interferometer at  $0.5 \text{ cm}^{-1}$  resolution serves as the key optical component in the OP-FTIR system. The interferometer can generate interferogram patterns, from which information regarding IR wavenumbers and the related intensities for each wavenumber can be obtained.

**Transmitting/receiving optics:** a standard 10-inch Newtonian telescope has the function of enlarging and recollimating the IR beam before it is transmitted along the path.

**Retroreflector:** a standard 37-cube retroreflector is used to return the IR beam passing through the absorbing medium.

**Detector:** the detector used in the OP-FTIR system is a LN<sub>2</sub>-cooled MCT detector which generally responds to IR with wavenumbers ranging from 700 to about  $4200 \text{ cm}^{-1}$  (Russwurm and Childers 2002).

### 3.1.2 Operating Procedure in Field

An operating procedure, as given in Appendix C, was developed and followed in the field work of this thesis.

### 3.1.3 Data Processing Procedure

The well-known Beer's law governs the basic processing of OP-FTIR spectra. The absorbance ( $A$ ) of IR is a function of the measured intensity ( $I$ ) and background intensity ( $I_0$ ) and is equal to the product of the absorption coefficient ( $\alpha$ ), the concentration  $C$  and the pathlength  $L$  (see equation below). Once  $A$  is known, the concentration ( $C$ ) of the chemical of interest can be calculated.

$$A = -\log\left(\frac{I}{I_0}\right) = \alpha CL \quad \text{Equation 3-1}$$

In the field, a zero-path background spectrum and a preliminary (Signal Processing Information) SPI file containing priority analytes and common atmospheric interferents ( $\text{H}_2\text{O}$ ,  $\text{CH}_4$  and  $\text{CO}_2$ , etc.) can be used for preliminary analysis. Priority analytes are chosen based on related air regulations and the known data of the target field area. After the measurements, in addition to upwind background method, the data can be analyzed thoroughly using Synthetic Background Method (SBM) as described below.

SBM is described and recommended by U.S. EPA method TO-16 (U.S. EPA 1999a). Steps involving the spectroscopy software GRAMS/AI (Version 9.1; Thermo Fisher Scientific, Inc.) and RMMSOft are summarized in Appendix D.

### 3.1.4 Quality Control/Assurance

The data quality objective is:  $\pm 10\%$  for precision/relative standard deviation (using the concentration of  $\text{N}_2\text{O}$ ,  $\sim 315$  ppb in air as a reference);  $\pm 10\%$  for accuracy (using the concentration of  $\text{N}_2\text{O}$ ,  $\sim 315$  ppb in air as a reference), if the path-length is greater than 100 m;  $\pm 15\%$  for accuracy, if the path-length is greater than 50 m but no more than 100 m; and  $\pm 20\%$  for accuracy if the path-length is no more than 50 m. More detailed information can be found in Appendix E.

## 3.2 Eddy Covariance System

### 3.2.1 Instrumentation

Burba (2013) describes the details of the principles, designing and implementing experiments, as well as data processing of EC method. The main components of the EC system used in this research project are briefly introduced as follows.

(1) the 3-D sonic anemometer (CSAT3; Campbell Scientific, Logan, UT, USA) measures the horizontal (u and v) and vertical (w) wind velocity components, as well as the temperature at a frequency up to 20 Hz. The sonic anemometer determines the wind speed by measuring the speed of the ultrasonic signal it emits and receives. The speed of the ultrasonic signal is determined by the speed of the ultrasonic in static air plus or minus the wind speed, depending on how the ultrasonic travels relative to the wind direction.

(2) the LI-7700  $\text{CH}_4$  open path gas analyzer (LI-COR Biosciences, Lincoln, NE, USA) is a high-speed (data output frequency up to 40 Hz), high-precision (RMS

of 5 ppbv at 10 Hz and typical ambient levels) open path methane analyzer that utilizes Wavelength Modulation Spectroscopy (WMS) to measure methane concentrations at ambient pressure and temperature. LI-7700 has a physical pathlength (multipass gas cell) of 0.5 m which equals a measurement path of 30 m. Along with methane concentrations, LI-7700 also measures the ambient temperature and pressure of the gas in the sampling path. In addition, the signal strength is recorded as dimensionless values (RSSI) which serves as an indicator for QA/QC and the need for mirror cleaning.

(3) the LI-7500A CO<sub>2</sub>/H<sub>2</sub>O open-path gas analyzer (LI-COR Biosciences, Lincoln, NE, USA) measures CO<sub>2</sub> and H<sub>2</sub>O in the atmosphere simultaneously at high frequency up to 40 Hz. It is a high performance, non-dispersive, open path analyzer with typical RMS noise of 0.11 ppmv for CO<sub>2</sub> and 0.0047 pptv for H<sub>2</sub>O.

A CR3000 datalogger (Campbell Scientific, Inc.) was used to record the raw data (at 10 Hz) generated by the instruments described above. The raw data were then processed using the software EddyPro (Version 4, LI-COR, Inc.)

### 3.2.2 Post-measurement Data Processing Procedure

The raw data recorded by the datalogger were input to EddyPro in the format of ASCII plain text. Information (metadata) regarding the sampling station, the instruments and the description of the raw files are required. EddyPro offers Express Mode and Advanced Mode for calculating fluxes. In the Express Mode, widely accepted (default) models and options are employed and thus requires

minimal user input. In contrast, the Advanced Mode allows a user to customize a variety of processing options. In this study, the Express Mode was used for data processing. The averaging interval for time series data and fluxes is 30 min. Major data processing functions done by EddyPro include the compensation for density fluctuations (Webb et al. 1980), time lags compensation (constant), and axis rotation for tilt correction (double rotation) (also refer to Section 2.3.6).

### 3.2.3 Quality Control/Assurance

As part of the QA/QC, signal strengths were used as “flags” to filter the raw data. For CH<sub>4</sub>, data collected with RSSI below 20% were discarded while for CO<sub>2</sub>, data with RSSI below 60% were removed. Based on the orientation of the sonic (85.1°), the data recorded with wind direction between 175.1° and 355.1° were discarded. Currently, EddyPro does not have the feature of filtering wind directions. So, a simple VBA program (see Appendix F) and Microsoft Excel were used to filter wind directions after the raw data had been processed using EddyPro.

## **Chapter 4    Field Campaign at a Biosolids Lagoon**

### **4.1    Site Description**

#### 4.1.1 Instrument Deployment

As presented in Figure 4-1, Lagoon #1 is the lagoon in study. It is surrounded by several other lagoons (Lagoons #2 through 6). The OP-FTIR was deployed at upwind and downwind locations, shown as Paths #1 through 5, along the edges of Lagoon #1. The EC system was placed on a concrete jetty (shown as the green triangle) extending about 9 m away from the north edge toward the centre of the Lagoon #1. Note that there were compost piles south of the lagoons. These compost piles had been changing over time, making it hard to delineate the compost emission sources using a Google™ satellite image.

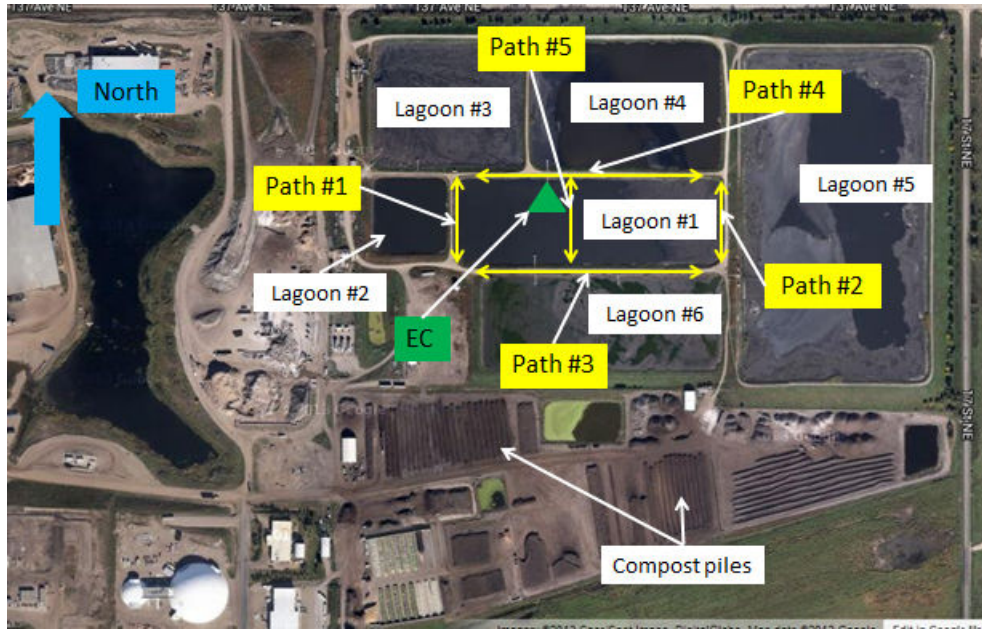


Figure 4-1 The surrounding environment of the lagoon in study (Lagoon #1) and positions of OP-FTIR (Paths #1 to 5) and EC relative to the lagoon

The basic parameters used for the OP-FTIR are summarized in Table 4-1. The relative positions of the EC instruments are shown in Figure 4-2. The sonic anemometer was facing at  $85.1^\circ$  (almost straight east). The centres of the paths of the sonic anemometer, the LI-7700 and the LI-7500A were at a height of 2.24 m above the water as depicted in Figure 4-2. Table 4-2 gives the eastward, and vertical separations required by EddyPro for the calculation. In the field, the centre-to-centre distance and rectilinear distances were recorded for calculating the northward and eastward.

Table 4-1 Basic parameters of OP-FTIR during the OP-FTIR field campaign

Parameters	Day 1	Day 3		Day 4		Day 5
		Up-wind	Down-wind	Up-wind	Down-wind	
Pathlength (m)	226	218	222	668	672	242
Height above around (m)	1.5	1.5	1.5	1.5	1.5	1.5
No. of Co-added scans	30	30	30	30	30	30
ZPD P-P (Volts)	~10	~10	~10	~3	~3	~10
Resolution (cm <sup>-1</sup> )	0.5	0.5	0.5	0.5	0.5	0.5

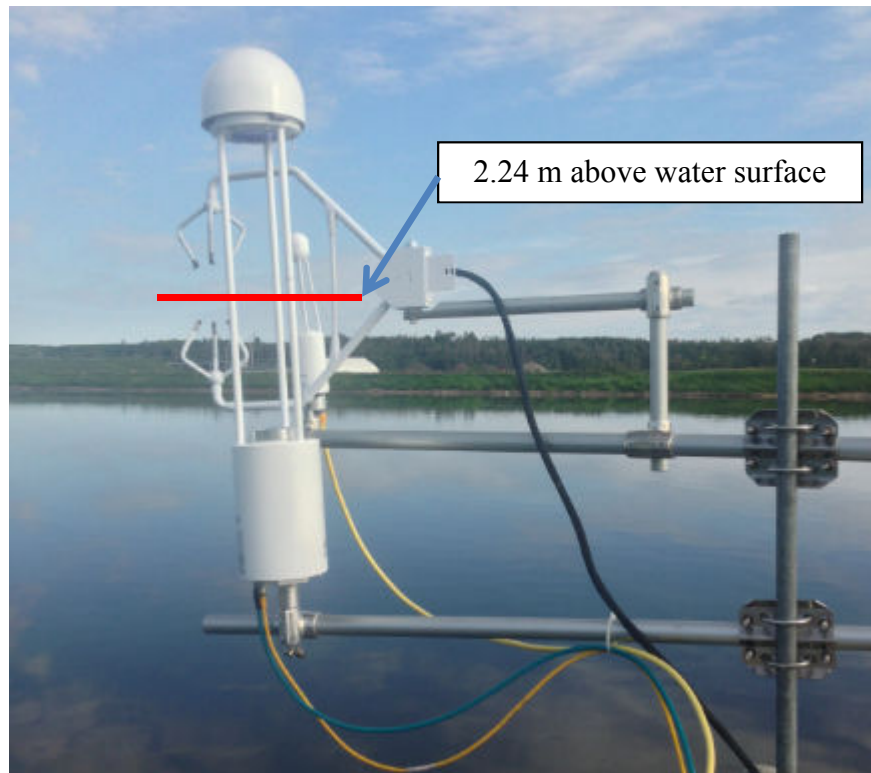


Figure 4-2 The EC system mounted on a concrete jetty at Lagoon #1

Table 4-2 Distances of separation required by EddyPro

Separation	LI-7700 (cm)	LI-7500A (cm)
Northward	-0.75	-15.30
Eastward	-22.49	-6.20
Vertical	0	0

#### 4.1.2 Overview of Data Quality Filtering

The data collected when wind direction and/or instrument signal strength do not meet data quality criteria during the whole EC field campaign were removed. Recall that the orientation of the sonic anemometer was 85.1 (measured relative to geographic north), thus, all wind directions between 175.1° and 355.1° were removed due to possible un-acceptable disturbance by the structures of LI-7700, LI-7500A and the mounting rails. For the LI-7700 and LI-7500A, data with signal strength (RSSI) less than 20% and 60% (chosen based on personal communication with Israel Begashaw, Sr. Application Analyst at LI-COR Inc.) were removed, respectively. Table 4-3 provides the percentages of data points remaining after each signal filtering process.

Table 4-3 Quantity and percentage of data points remained after each quality filtering

<b>Data Points</b>	<b>Total</b>	<b>After Signal Filtering</b>	<b>After Wind Direction Filtering</b>	<b>After Other Filtering</b>
Quantity	4215	2570	1396	1331
Percentage of Total Quantity	100%	61%	33%	32%

All data presented in the following section (unless otherwise stated) have been processed by EddyPro and passed the data quality checks. The majority of the signal loss was caused by precipitation events, causing about 38% of the total data points to be removed. About 1% of the total data points were lost due to power loss or trouble shooting. As a result, 61% of the total data points remained after the signal filtering. In addition to signal filtering and wind direction filtering,

other filtering was due to loose cable connection and/or the quality checks by EddyPro.

#### 4.1.3 Meteorological Observations

The majority of the wind speeds observed during the field campaign were between 1~3 m/s and the prevailing wind direction was around 45°, as illustrated in Figure 4-3. At this wind direction and a typical fetch (around 200 m), lagoon #4 north of the lagoon under study (lagoon #1) could contribute to the concentrations measured by the EC system. Despite this, about 27% of the data were obtained with wind directions  $120^\circ \pm 30^\circ$ , the ideal wind direction for optimal fetch, representative of the emission flux of the lagoon. More details with regard to wind direction and fetch will be discussed in Section 4.5.8.

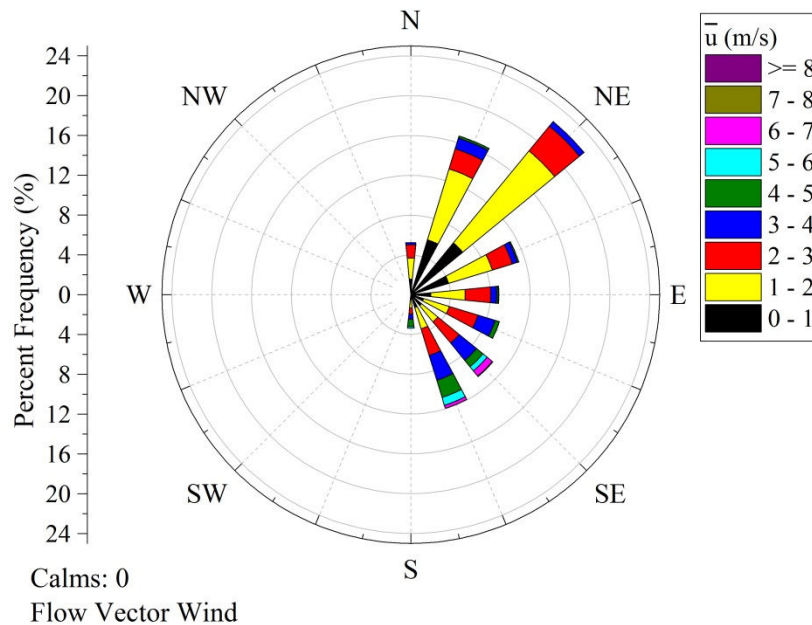
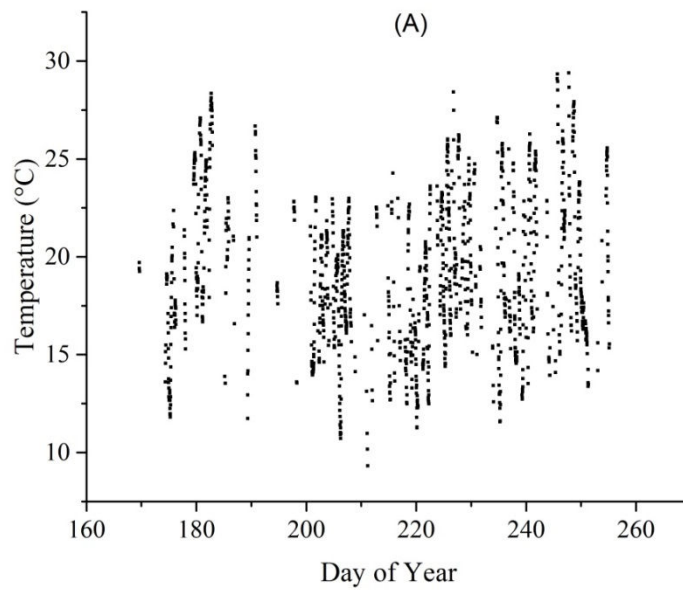


Figure 4-3 Windrose of filtered data during the EC field campaign

Time series (30-min average, same for all time series plots) of temperature are shown in Figure 4-4 (A) indicating that the temperatures ranged from 9.3 °C to 29.4 °C, with a median value of 18.8 °C. A diurnal pattern of temperature is shown in Figure 4-4 (B). The lowest temperature in a day was typically observed in the early morning while the highest temperature was typically recorded in the late afternoon. Precipitation during the whole field campaign was frequent, causing the rejection of about 39% of the total data, as discussed in Section 4.1.2.



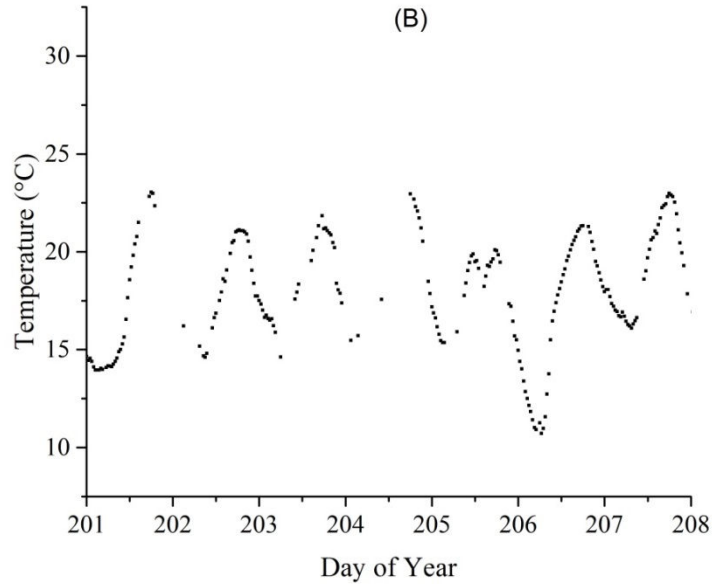


Figure 4-4 Time series of temperature measurements (filtered data). (A): full scale; (B): zoom in

Figure 4-5 indicates that the relationship between the normalized standard deviation of vertical velocity ( $\sigma_w/u^*$ ) and stability  $|z/L|$  (unstable conditions only) agrees well with an existing model (Wilson 2008) for an undisturbed surface layer, but lower than the model described by Kaimal and Finnigan (1994).

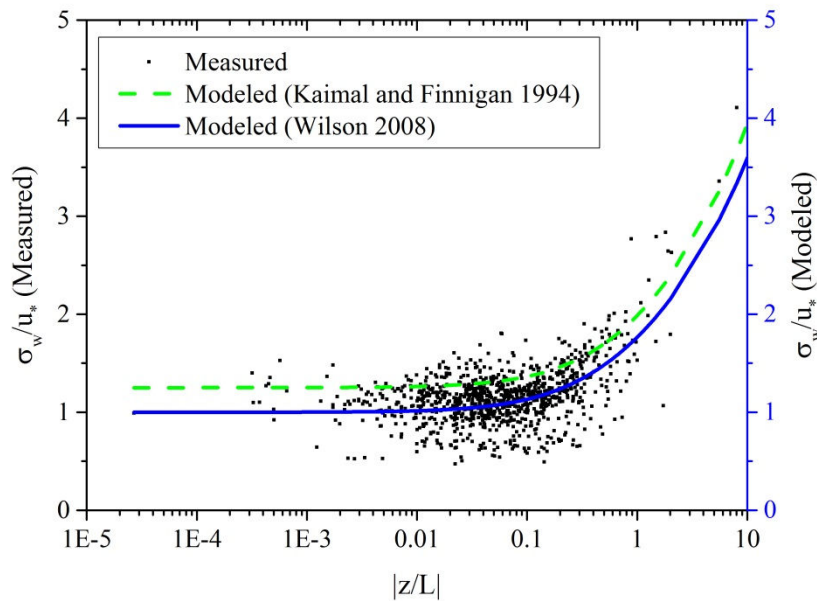


Figure 4-5 Variation of normalized standard deviation of vertical velocity ( $\sigma_w/u_*$ ) plotted against stability ( $|z/L|$ ) ( $\log_{10}$  scale; for unstable conditions).

## 4.2 Concentrations from OP-FTIR

A 5-day-long field campaign measuring methane and ammonia using OP-FTIR was conducted with the help of a volunteer. On Day 1, only upwind (Path #1 in Figure 4-1) concentrations were measured using OP-FTIR due to the availability of the volunteer. Not enough meaningful data were obtained on Day 2 as there was a problem with the heater of the OP-FTIR and most of the time was spent on trouble-shooting. On Days 3 and 4, OP-FTIR was placed at the upwind side (Paths #1 and 3, respectively) first for 1 or 2 hours, depending on the time abundance of each day, and then moved to downwind side (Paths #2 and 4, respectively) for 2 hours. On the last day (Day 5) of the field campaign, OP-FTIR

was deployed close (Path #5) to the EC system for the purpose of comparing methane concentrations from the two different methods.

Table 4-4 summarizes the minimum, maximum and median concentrations of CH<sub>4</sub>, the sampling durations for each scenario (i.e. upwind, downwind, and close-to-EC configurations), as well as basic meteorological parameters (i.e. wind direction, mean wind speed, and mean temperature) for the OP-FTIR field campaign. Time series results are presented in following figures.

Table 4-4 Summary of CH<sub>4</sub> concentrations and meteorological conditions during the OP-FTIR field campaign

CH <sub>4</sub>	Day 1	Day 3		Day 4		Day 5
		Up-wind	Down-wind	Up-wind	Down-wind	
Min (ppmv)	1.9	2.1	2.3	2.2	2.0	2.9
Max (ppmv)	3.3	2.7	3.6	3.0	3.3	4.8
Median (ppmv)	2.4	2.5	2.7	2.6	2.6	3.8
Average (ppmv)	2.4	2.5	2.7	2.6	2.6	3.8
Time duration (hours)	4	2	2	1	2	2.5
β (°)	258	293	273	151	198	63
U (m/s)	3.2	3.9	4.6	0.8	1.5	2.5
Mean T (°C)	20	18	18	20	24	24

Note: average values are over the whole time duration for each day.

On Days 1 and 3, the OP-FTIR was placed on west side (Path #1) of the lagoon. The basic meteorological parameters in the two days were close to each other (Table 4-4). Thus, it is not surprising that the median concentrations of CH<sub>4</sub> are very close (2.4 and 2.5 ppmv, or 4% difference). On Day 4, the prevailing wind

was from south. As described in Section 4.1, there is another lagoon (Lagoon #6) and compost piles south of the lagoon. The complex emission sources and the relatively calm wind conditions ( $\sim 1$  m/s) might be responsible for the fact that the upwind and downwind measurements of  $\text{CH}_4$  on Day 4 are almost at the same level (see Figure 4-8). The test lagoon is surrounded by other lagoons and compost piles, as a result, the upwind concentrations ( $\sim 2.5$  ppmv) during the whole OP-FTIR field campaign are actually higher than the ambient background level ( $\sim 1.9$  ppmv). On Day 5, the OP-FTIR was placed close to the EC system, with the center of the optical path slightly lower than that of the EC system. The OP-FTIR was about 1.5 m east (Path #5) to the EC system. Detailed comparison results are presented in Section 4.3.1.

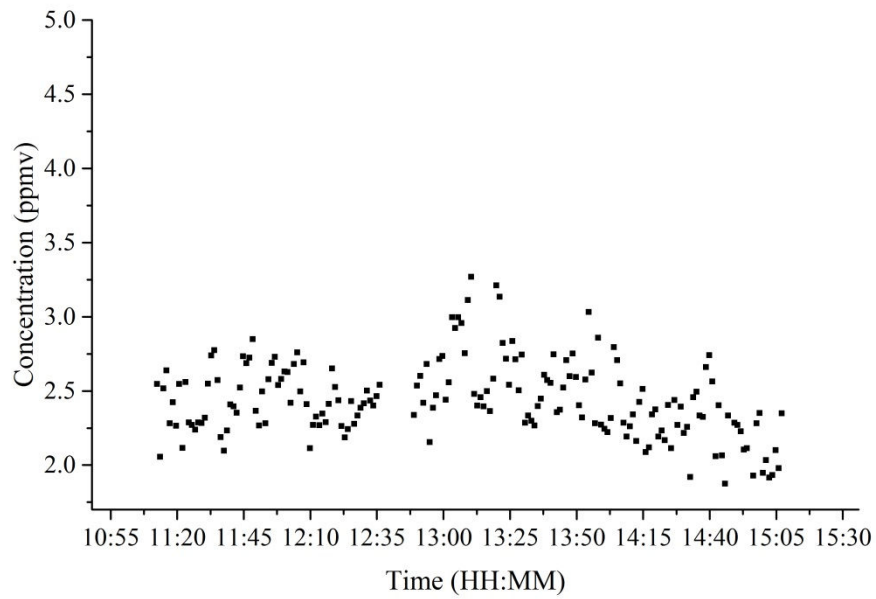


Figure 4-6 Time series of methane concentrations measured using OP-FTIR at upwind side (west side) of the lagoon on Day 1 of the OP-FTIR field campaign

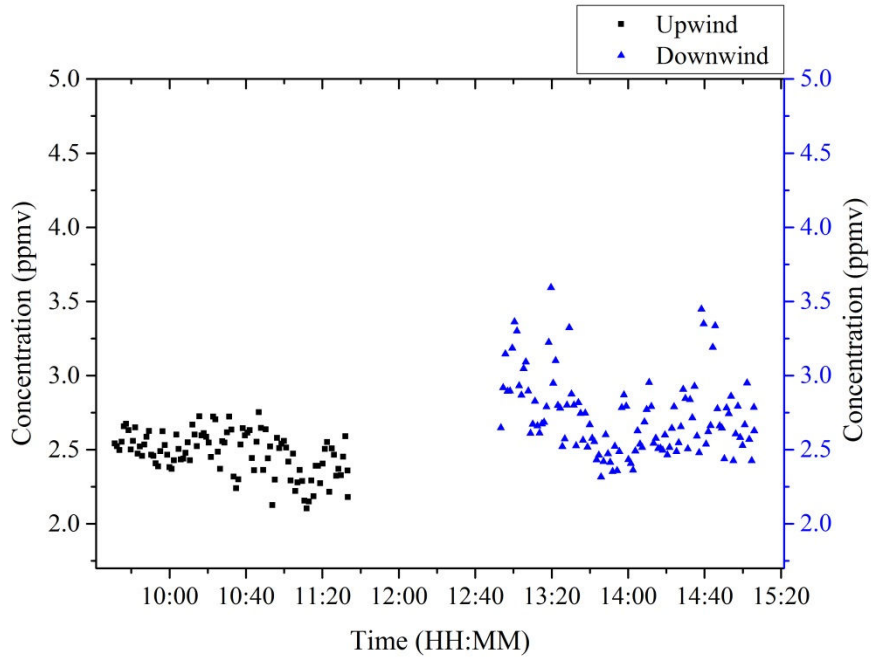


Figure 4-7 Time series of methane concentrations measured using OP-FTIR at both upwind (west) and downwind (east) on Day 3

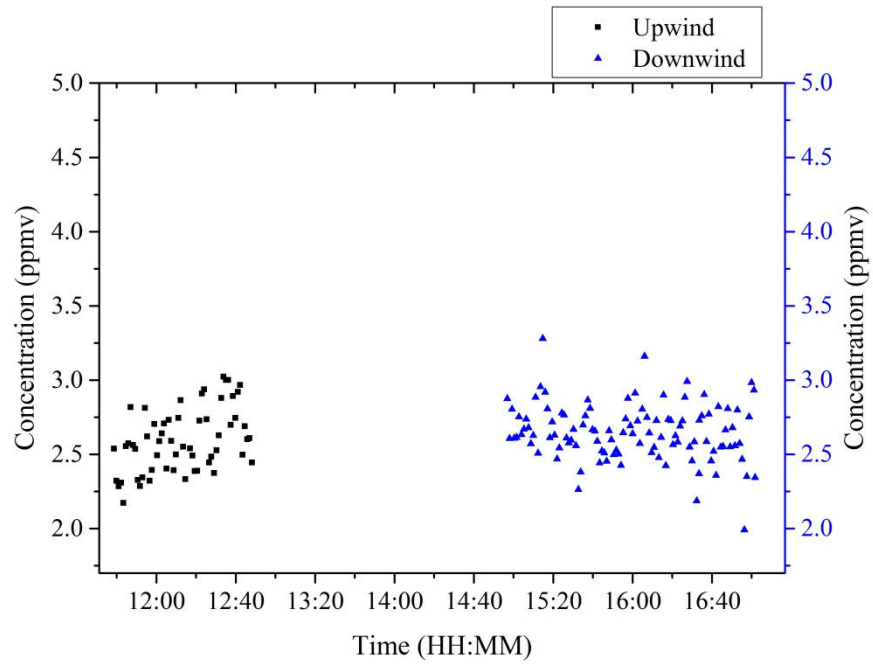


Figure 4-8 Time series of methane concentrations measured using OP-FTIR at both upwind (south) and downwind (north) on Day 4

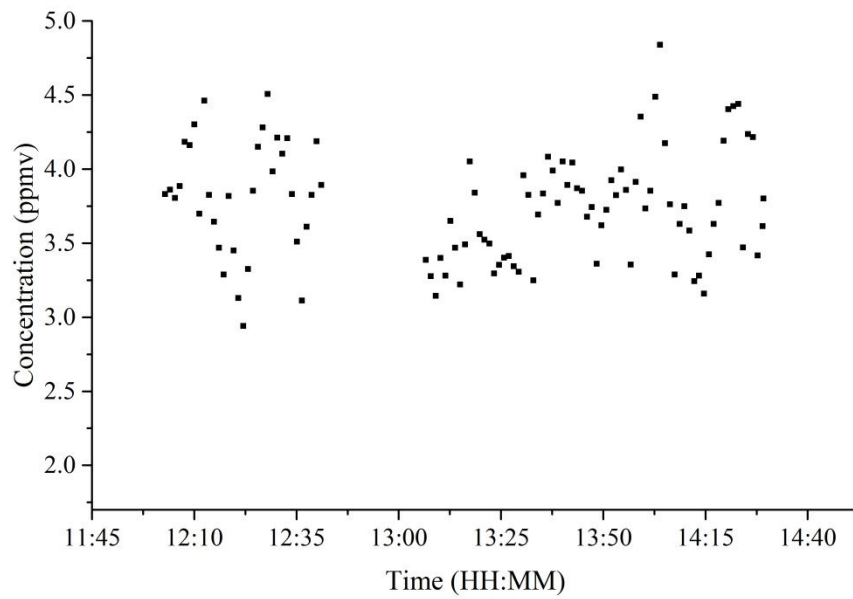


Figure 4-9 Time series of methane concentrations measured using OP-FTIR close to EC system on Day 5

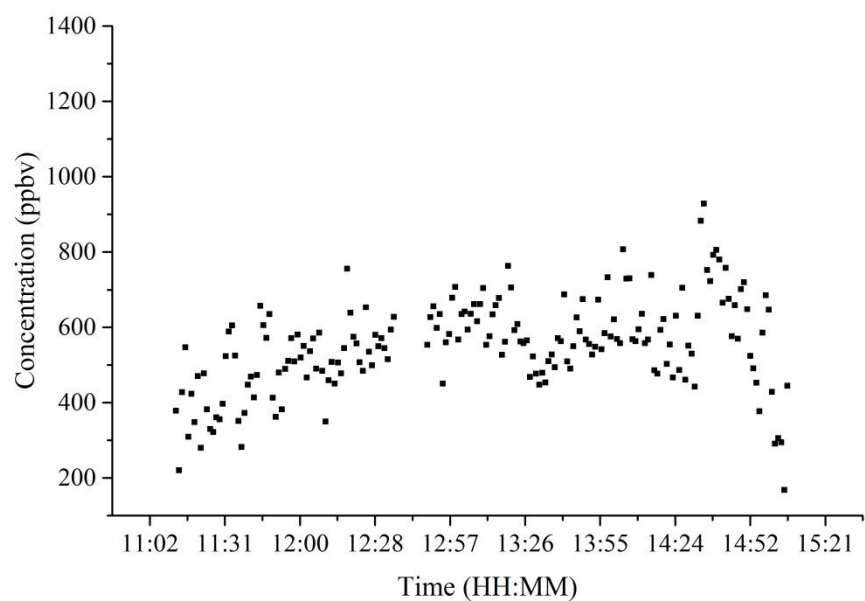


Figure 4-10 Time series of NH<sub>3</sub> concentrations measured using OP-FTIR at upwind side (west side) on Day 1

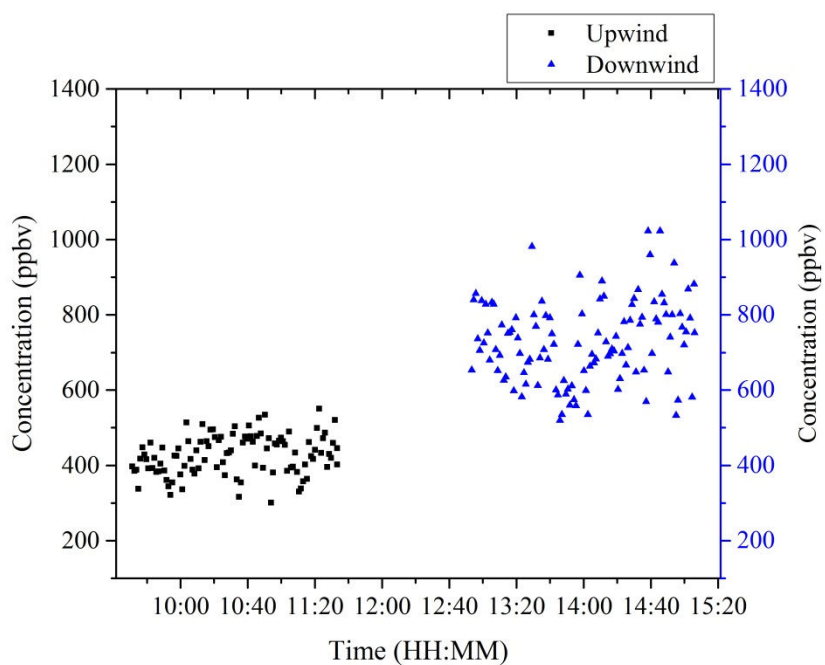


Figure 4-11 Time series of ammonia concentrations measured using OP-FTIR at both upwind (west) and downwind (east) on Day 3

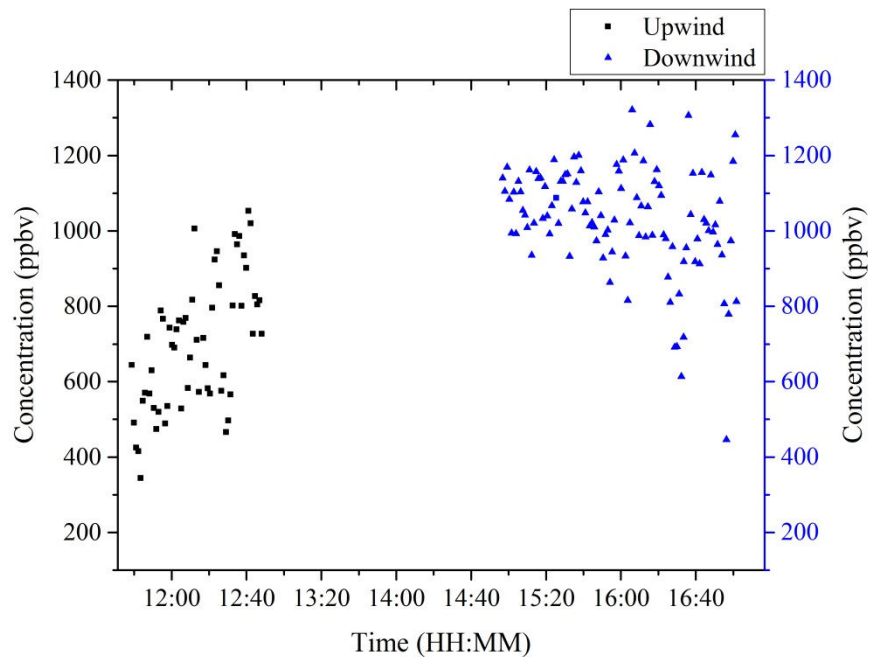


Figure 4-12 Time series of ammonia concentrations measured using OP-FTIR at both upwind (south) and downwind (north) sides on Day 4

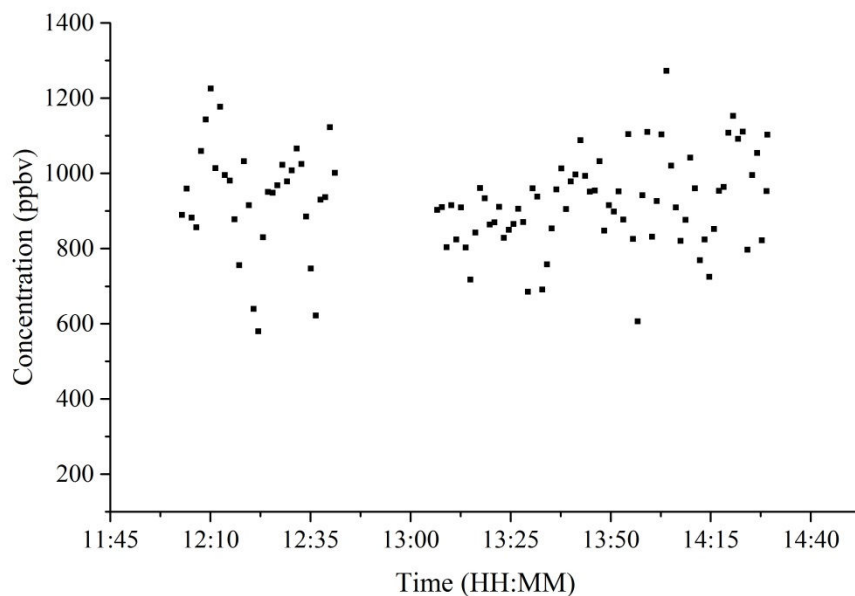


Figure 4-13 Time series of ammonia concentrations measured using OP-FTIR close to EC system on Day 5 of the OP-FTIR field campaign

Table 4-5 shows the minimum, maximum and median concentrations of NH<sub>3</sub>. For convenience, the time duration and the basic meteorological values are also shown in this table, although they are the same as those presented in Table 4-4. It can be seen that the concentration of NH<sub>3</sub> during the whole OP-FTIR field campaign ranges from 168 ppbv to 1321 ppbv (or, 1.3 ppmv). Compared to the concentrations of CH<sub>4</sub>, the concentrations of NH<sub>3</sub> have more variations in different scenarios. The differences between upwind and downwind concentrations are larger (up to ~75%). Possibly, the larger differences are probably because there were fewer emission sources upwind of the lagoon.

Table 4-5 Summary of NH<sub>3</sub> concentrations and meteorological conditions of the OP-FTIR field campaign

NH <sub>3</sub>	Day 1	Day 3		Day 4		Day 5
		Up-wind	Down-wind	Up-wind	Down-wind	
Min (ppbv)	168	300	520	344	446	579
Max (ppbv)	928	550	1023	1053	1321	1272
Median (ppbv)	557	429	721	713	1041	932
Time duration (hours)	4	2	2	1	2	2.5
β (°)	258	293	273	151	198	63
U (m/s)	3.2	3.9	4.6	0.8	1.5	2.5
Mean T (°C)	20	18	18	20	24	24

Note: concentration data are averages over 1-min. Other data are averages for each day.

### 4.3 Concentrations from EC

An overview of the minimum, maximum and median concentrations of CH<sub>4</sub> and CO<sub>2</sub> measured by EC during the whole field campaign is shown in Table 4-6. Time series of CH<sub>4</sub> and CO<sub>2</sub> concentrations, as well as the relationships between concentrations and typical meteorological observations are discussed in Sections 4.3.1 to 4.3.5. All data points in the plots are averages over 30-minute, unless otherwise stated.

Table 4-6 Minimum, maximum and median concentrations of CH<sub>4</sub> and CO<sub>2</sub> measured by EC

<b>Statistics</b>	<b>CH<sub>4</sub></b>	<b>CO<sub>2</sub></b>
Min (ppmv)	2.7	248.7
Max (ppmv)	40.0	588.3
Median (ppmv)	5.3	384.4

Note: values shown are 30-min averages for EC data.

#### 4.3.1 Time Series of CH<sub>4</sub> Concentration Measurements

Figure 4-14 (A) presents the time series of measurements of CH<sub>4</sub> concentrations (from LI-7700). The majority of the concentrations are around 5 ppmv. A closer look at the variation of the concentrations, as shown in Figure 4-14 (B), indicates that the concentrations of CH<sub>4</sub> are typically higher at night (highest concentrations occurred around midnight) than in the day. These results are consistent with those from previous studies and are attributable to reduced mixing caused by the radiation inversion at night (Brown 2013).

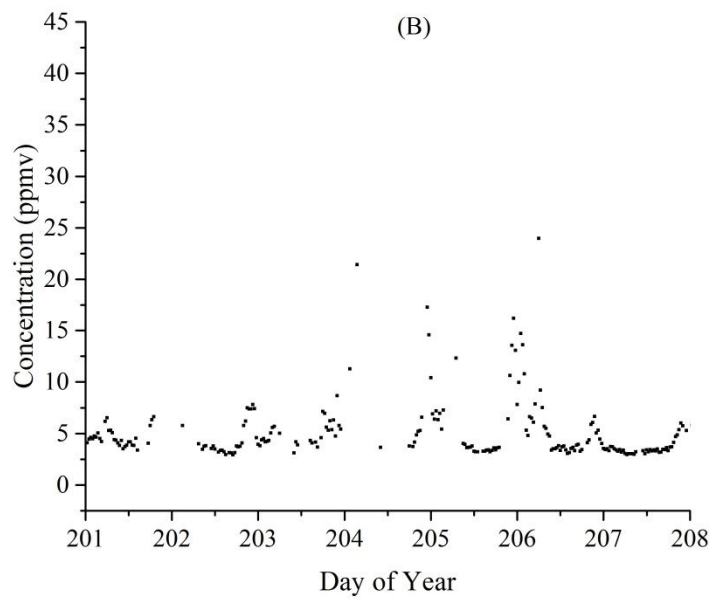
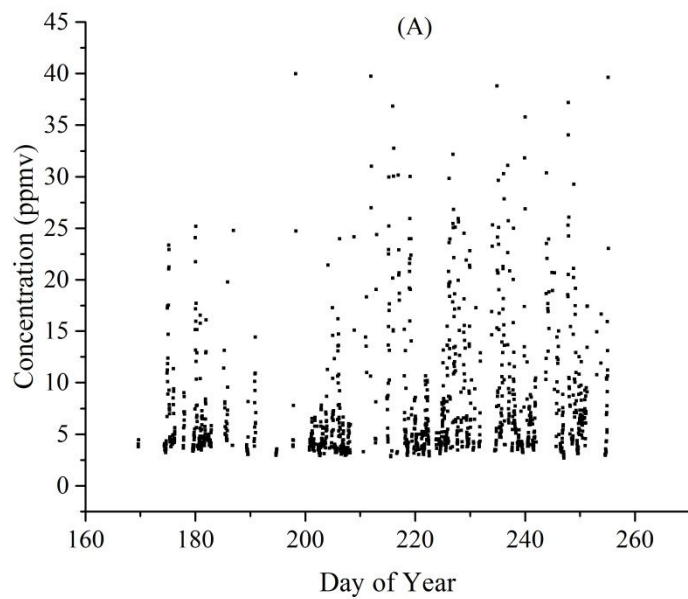


Figure 4-14 Time series of CH<sub>4</sub> concentration measurements (filtered data). (A): full scale; (B): zoom in

CH<sub>4</sub> concentrations obtained using OP-FTIR on Day 5 of the OP-FTIR campaign are compared to CH<sub>4</sub> concentrations collected using EC system for the same time periods (Figure 4-15). It is obvious that the concentrations of CH<sub>4</sub> measured by OP-FTIR were lower than those by EC most of the time. The dominant reason might be that the OP-FTIR was sampling at a different path (single-trip pathlength = 242 m) than that (single-trip pathlength = 0.5 m) of the LI-7700 methane analyzer. As a result, it is possible that the LI-7700 was sampling at “hot spots” (places where the gas concentration is higher than other places). Another possible reason (if the CH<sub>4</sub> concentration was changing rapidly) might be the difference in the sampling frequency (~2 second for OP-FTIR and 0.1 second for EC) and work flow (Figure 4-16). The EC was sampling continuously at a frequency of 10 HZ. However, the OP-FTIR needed ~14 seconds to process (calculate concentrations) the collected data before start the next data collection.

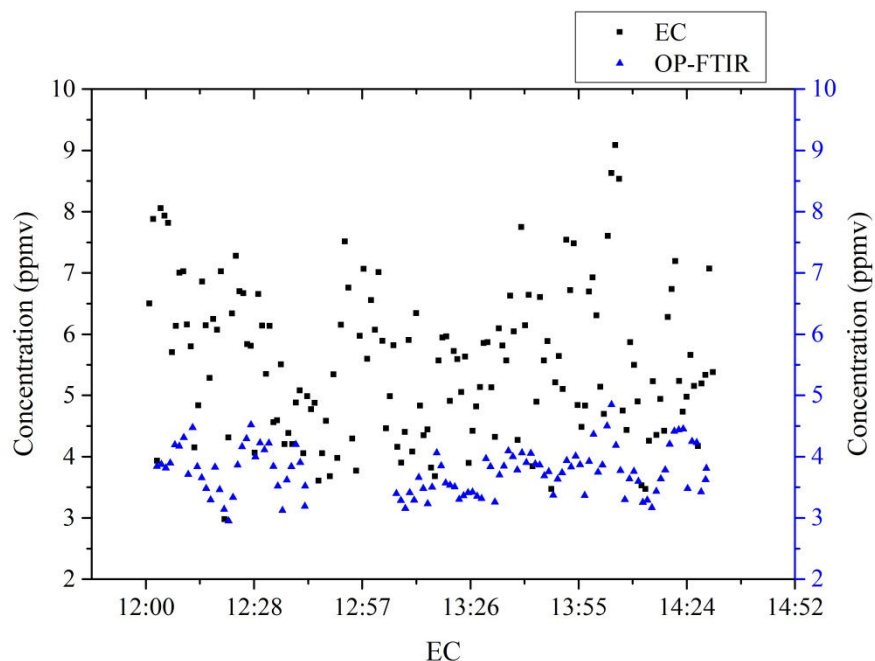


Figure 4-15 Comparison of methane concentrations measured by OP-FTIR and EC on Day 5 of the OP-FTIR field campaign

Note: data points are 1-min averages, different than other plots of EC results (averages over 30-min).

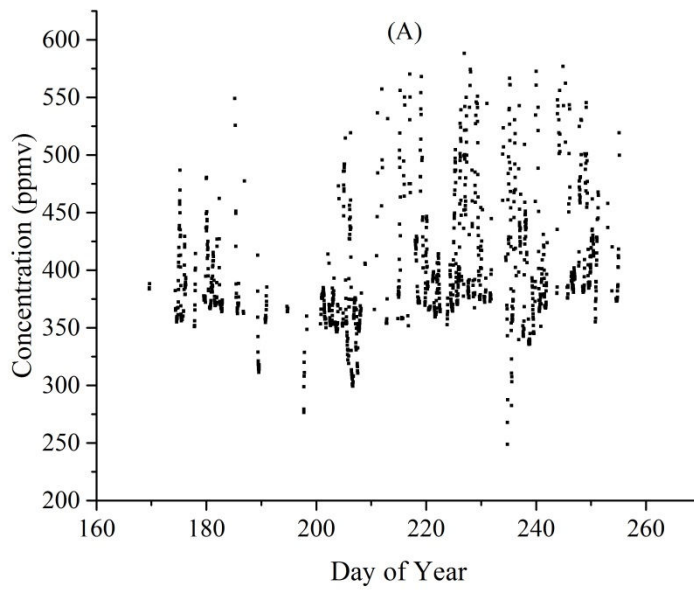


Figure 4-16 Typical work flow of OP-FTIR during the field campaign

#### 4.3.2 Time Series of CO<sub>2</sub> Concentration Measurements

Similar to the time series of CH<sub>4</sub> concentration measurements discussed in Section 4.3.1, the concentrations of CO<sub>2</sub> (from LI-7500A) show lower values at night as depicted in Figure 4-17 (B). However, the peak concentrations of CO<sub>2</sub>

seem to occur in the early morning (before photosynthesis commences), which is consistent with typical diurnal concentration cycle of CO<sub>2</sub>, compared to around midnight for CH<sub>4</sub>.



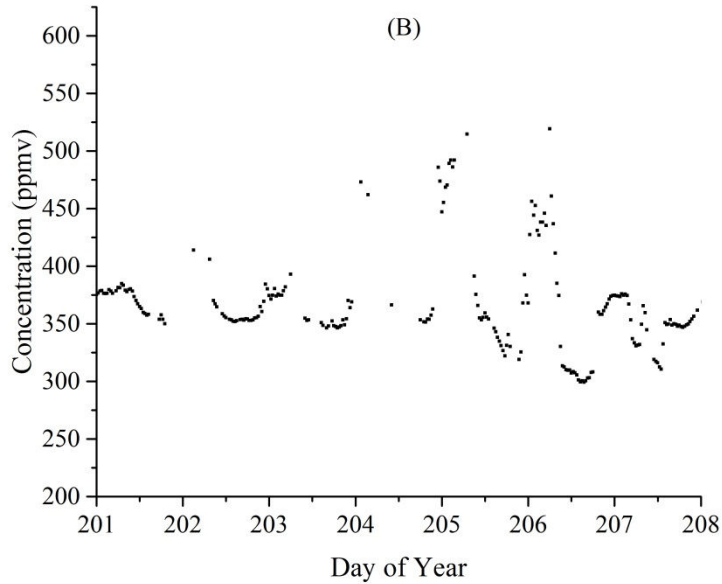


Figure 4-17 Time series of CO<sub>2</sub> concentration measurements (filtered data). (A): full scale; (B): zoom in

#### 4.3.3 Concentrations and Temperature

As discussed in Sections 4.3.1 and 4.3.2, daily concentrations (from EC system) of CH<sub>4</sub> and CO<sub>2</sub> were found to be higher at night when temperatures were generally lower than in the day. As a result, it is reasonable that the concentrations of CH<sub>4</sub> and CO<sub>2</sub> were generally higher (with broad range) at lower temperatures (10-22 °C). As the temperature increased above ~22 °C, the range of the concentrations of CH<sub>4</sub> and CO<sub>2</sub> stayed narrow.

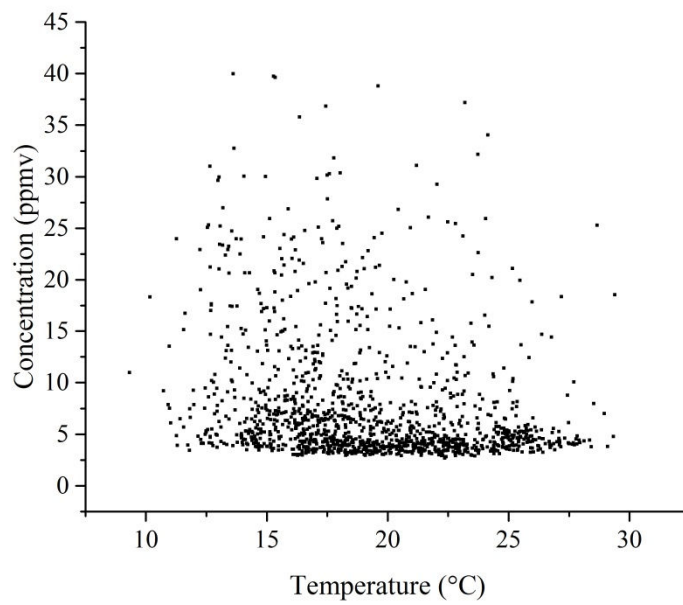


Figure 4-18 Concentrations of CH<sub>4</sub> plotted against temperature (filtered data)

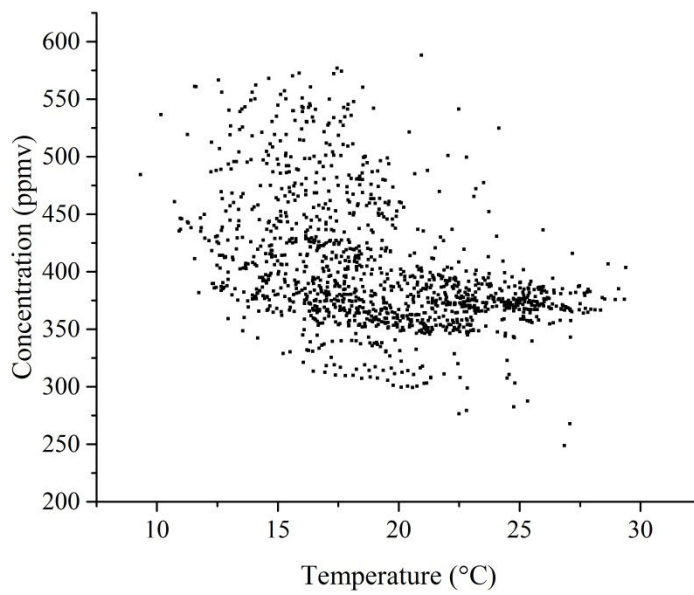


Figure 4-19 Concentrations of CO<sub>2</sub> plotted against temperature (filtered data)

#### 4.3.4 Concentrations and Wind Speed

As depicted in Figures 4-20 and 4-21, concentrations of CH<sub>4</sub> and CO<sub>2</sub> decreased as wind became stronger. The wind can bring cleaner air from upwind direction to the location of the EC system and thus a stronger wind usually means more dilution (smaller gas phase mass transfer resistance), which is reflected by lower concentrations observed, of the compounds of interest.

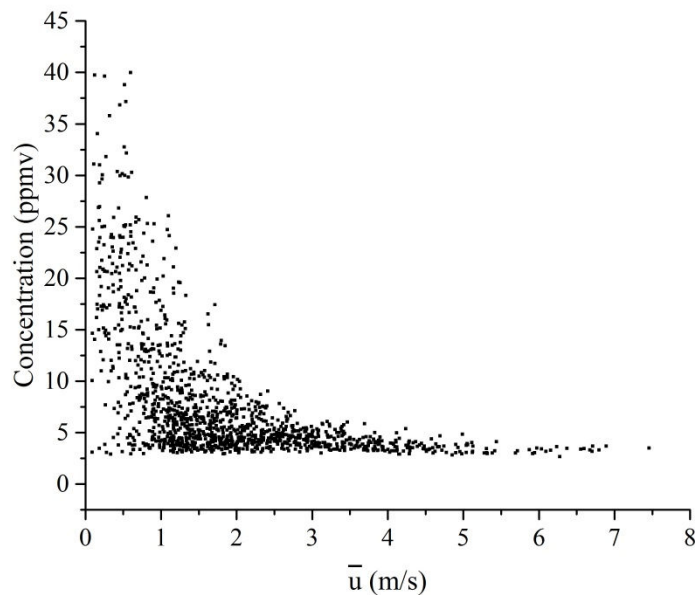


Figure 4-20 Concentrations of CH<sub>4</sub> plotted against wind speed (filtered data). (A): full scale; (B): zoom in

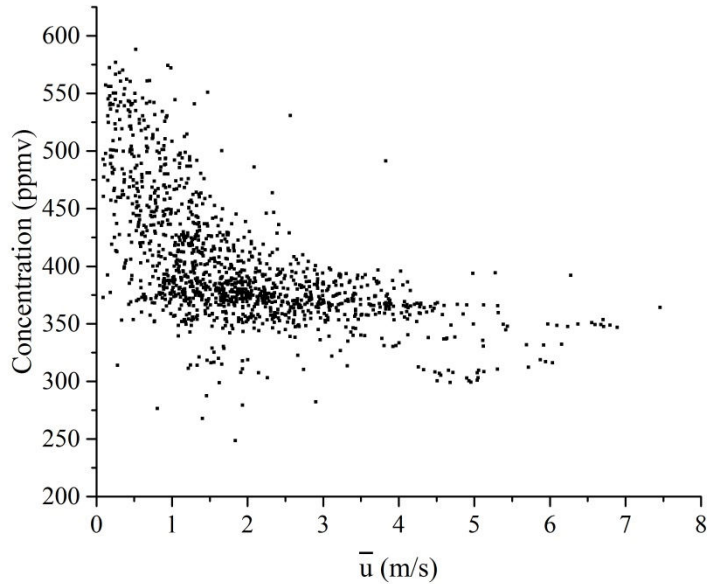


Figure 4-21 CO<sub>2</sub> concentrations plotted against wind speed (filtered data). (A): full scale; (B): zoom in

#### 4.3.5 Concentration Roses

From Figures 4-22 and 4-23, one can see that wind direction had similar impacts on concentrations of CH<sub>4</sub> and CO<sub>2</sub> during the field campaign. When the wind was blowing from around northeast (NE) direction, a larger portion of the concentrations were identified to be higher (5 ppmv to 15 ppmv for CH<sub>4</sub> and 400 ppmv to 500 ppmv for CO<sub>2</sub>) than those concentrations with wind directions around southeast (SE) (2 ppmv to 10 ppmv for CH<sub>4</sub> and 350 ppmv to 400 ppmv for CO<sub>2</sub>). A quick glance at Figure 4-1 will reveal that larger Lagoons #4 and 5 might contribute to the higher concentrations when wind was from around NE. In contrast, as the wind direction changed to SE, fewer emission sources (smaller area of lagoons) could impact the concentrations measured by the EC system

located above the surface of the lagoon in study (Lagoon #1) and therefore the lower concentrations at these wind directions are understandable.

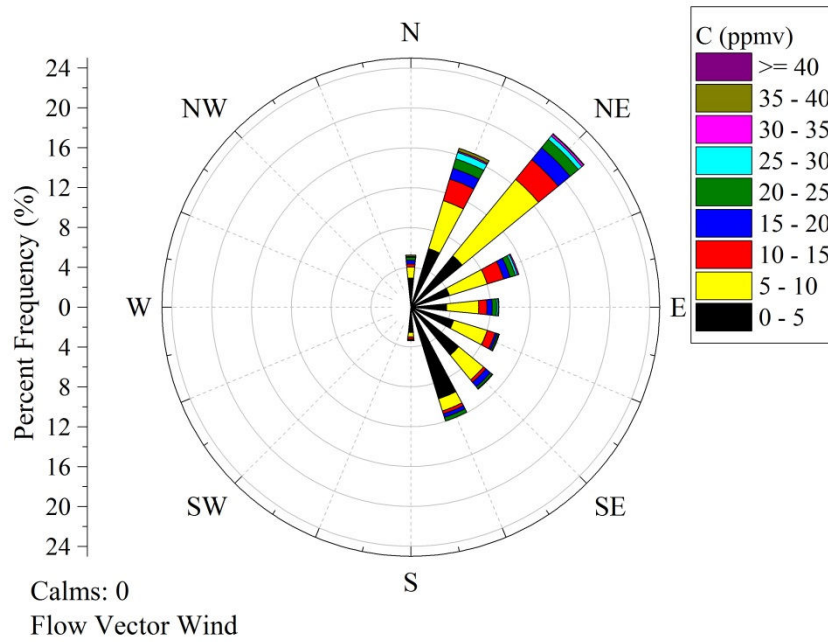


Figure 4-22 CH<sub>4</sub> concentration rose (filtered data). Color indicates CH<sub>4</sub> concentration in ppmv, wedges correspond to wind direction

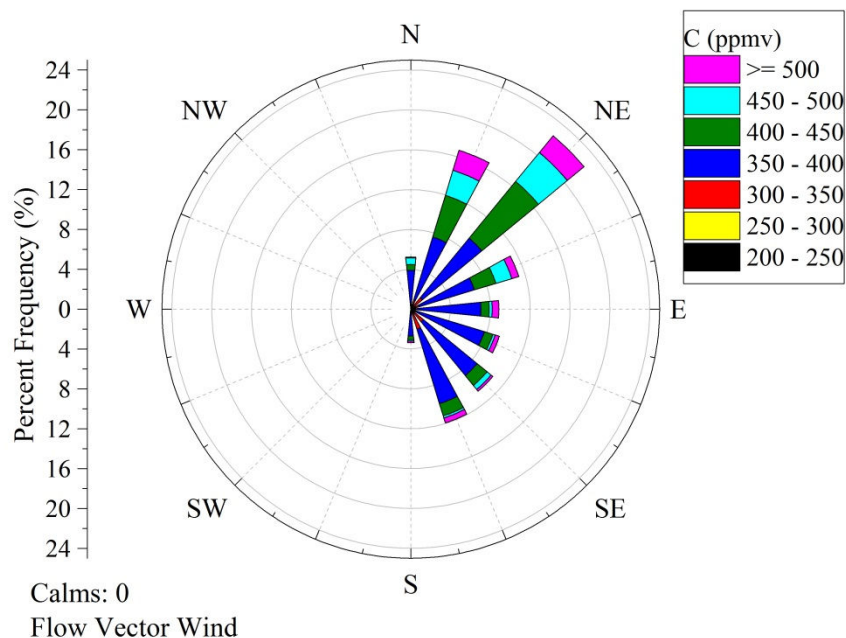


Figure 4-23 CO<sub>2</sub> concentration rose (filtered data). Color indicates CO<sub>2</sub> concentration in ppmv, wedges correspond to wind direction

#### 4.4 Emission Fluxes Derived Using Inverse Dispersion

##### 4.4.1 Input Parameters

Simulation of emission fluxes using ID are only performed for OP-FTIR data collected on Day 3 (Aug. 21, 2013) of the OP-FTIR field campaign. On Day 3, the prevailing wind was from west, where there were fewer emission sources upwind of the studied lagoon (Lagoon #1). For other days, ID simulations are not performed as the wind directions were not acceptable (due to complicated upwind emission sources) or data not available for both upwind and downwind concentrations. The meteorological conditions and concentrations of CH<sub>4</sub> and NH<sub>3</sub> are listed in Table 4-7 as input parameters of WindTrax. Of the meteorological conditions, the roughness length ( $z_0$ ) was chosen based on the

surface conditions at the lagoons (Arya 2001). Other meteorological conditions were from the results produced by EddyPro using raw data from the EC system. Downwind concentrations of CH<sub>4</sub> and NH<sub>3</sub> were measured by OP-FTIR for each time period while the upwind concentrations of CH<sub>4</sub> and NH<sub>3</sub> were chosen arbitrarily based on the upwind concentrations measured by OP-FTIR (during 9:30 to 11:30 am) on the same day before the OP-FTIR was moved to the downwind location.

Table 4-7 Meteorological conditions and concentrations of CH<sub>4</sub> and NH<sub>3</sub> as input parameters for the WindTrax simulations

Time	T	P	$\beta$	$u^*$	L	$z_0$	CH <sub>4,upwind</sub>	CH <sub>4,downwind</sub>	NH <sub>3,upwind</sub>	NH <sub>3,downwind</sub>
1330	19.5	94591.3	285.6	0.3	-74.3	0.0015	2.9	2.4	0.72	0.44
1400	19.7	94580.2	264.2	0.3	-329.6	0.0015	2.6	2.4	0.68	0.44
1430	20.0	94570.6	268.5	0.3	2994.5	0.0015	2.6	2.4	0.71	0.44
1500	20.4	94563.8	275.4	0.2	-55.3	0.0015	2.8	2.4	0.78	0.44

Note: input parameters include temperature (T, °C), pressure (P, Pa), wind direction ( $\beta$ , ° from North), friction velocity ( $u^*$ , m/s),

Obukhov length (L, m), roughness length ( $z_0$ , m), and downwind/upwind concentrations (ppmv) of CH<sub>4</sub> (CH<sub>4,downwind</sub>/CH<sub>4,upwind</sub>) and NH<sub>3</sub>

(NH<sub>3,downwind</sub>/NH<sub>3,upwind</sub>).

The simulation was performed using  $N_p = 50,000$  particles released from each sensor location with 30 points along the OP-FTIR optical paths used to represent path averaged concentrations. The height of the OP-FTIR optical paths was 1.5 m above the ground. Figure 4-24 shows an example of the touchdown fields of backward trajectories using WindTrax. Results are presented and compared in Section 4.4.2.



Figure 4-24 A screenshot of the WindTrax main screen during a simulation to compute fluxes at the lagoons.

Note: Two OP-FTIR beams were put on the map (west and east edge of the Lagoon #1). Green area means emission source of the lagoon in study; yellow areas mean interfering emission sources. (Red dots indicate the released particles are touching down within the boundary of a source while grey dots show touching down outside the boundary).

#### 4.4.2 Results

Results from WindTrax simulations are given in Table 4-8. The average emission fluxes/rates of CH<sub>4</sub> and NH<sub>3</sub> were  $4.66 \times 10^{-3}$  kg/(m<sup>2</sup>-day) (or 6.9 kg/day) and  $4.19 \times 10^{-3}$  kg/(m<sup>2</sup>-day) (or 6.2 kg/day), respectively. The emission fluxes of CH<sub>4</sub> determined in this study were about 50% lower than the emission flux [ $9.5 \times 10^{-3}$  kg/(m<sup>2</sup>-day)] determined at the same lagoon in April, 2012 (Brown 2013). However, since in both studies only a few data points were calculated using ID technique, the emission fluxes might still be comparable considering the fact that the weather conditions were different. Actually, the emission fluxes determined by ID are consistent with the emission fluxes calculated by EC for the same time periods in this study (see Section 4.5.5 for further information). However, the CH<sub>4</sub> emission fluxes by EC shown in Table 4-8 were found to be about 60% lower than the median emission fluxes during the whole EC field campaign. Since in this study the ID and EC techniques shared the same set of meteorological measurements by the sonic anemometer of the EC system, the lower emission fluxes during the OP-FTIR field campaign could be due to the disturbance caused by the structures of the EC system and the poles at an unfavorable wind direction (west wind).

While direct comparison of emission fluxes between the test lagoon and other lagoons (with different compositions and environment) may not contribute much to understanding the accuracy of the results obtained in this study, it can give an idea of the strength of emission fluxes of the test lagoon compared to others. The

emission fluxes of NH<sub>3</sub> shown in Table 4-8 are of the same order of magnitude as the average emission fluxes [(2.72×10<sup>-3</sup> kg/(m<sup>2</sup>-day) and 4.36×10<sup>-3</sup> kg/(m<sup>2</sup>-day)) of NH<sub>3</sub> measured using a flow-through dynamic chamber system and two sets of OP-FTIRs at two biosolids lagoons of a swine farm as reported by Aneja et al. (2008) and (Rumsey 2004). However, the NH<sub>3</sub> results in Table 4-8 are about one order of magnitude lower than NH<sub>3</sub> results reported by Zahn et al. (2001) and about one order of magnitude higher than the values (see Chapter 2) reported by Rose (2003) As can be seen from Table 4-8, the Relative Standard Deviation (RSD) for emission fluxes of CH<sub>4</sub> is small compared to that for NH<sub>3</sub>, indicating that the emission fluxes of CH<sub>4</sub> were more stable than those of NH<sub>3</sub> during the field study.

Table 4-8 Emission fluxes/rates of CH<sub>4</sub> and NH<sub>3</sub> simulated using WindTrax. Area (3.56×10<sup>4</sup> m<sup>2</sup>) of the lagoon was calculated by WindTrax.

Time	CH <sub>4</sub>	CH <sub>4</sub>	NH <sub>3</sub>	NH <sub>3</sub>
	kg/(m <sup>2</sup> -day)	kg/hour	kg/(m <sup>2</sup> -day)	kg/hour
1330	4.7×10 <sup>-3</sup>	6.9	2.4×10 <sup>-3</sup>	3.5
1400	5.2×10 <sup>-3</sup>	7.8	5.5×10 <sup>-3</sup>	8.2
1430	4.3×10 <sup>-3</sup>	6.3	4.8×10 <sup>-3</sup>	7.1
1500	4.5×10 <sup>-3</sup>	6.7	4.1×10 <sup>-3</sup>	6.1
Average	4.7×10 <sup>-3</sup>	6.9	4.2×10 <sup>-3</sup>	6.2
RSD (%)	9%	9%	32%	32%

#### 4.5 Emission Fluxes Derived Using EC

Raw data collected by EC system were processed using EddyPro (version 4.2) Express Mode (refer to Section 3.2.2 for major functions of EddyPro). Table 4-9 presents the minimum, maximum and median emission fluxes and emission rates

of CH<sub>4</sub> and CO<sub>2</sub>. The emission rates (in kg/hour) were calculated by multiplying the fluxes (in kg/(m<sup>2</sup>-day)) by the area determined by WindTrax, the same as stated in Section 4.4.2. Note that the minimum or maximum values shown here might not be representative of the overall emission fluxes. Detailed time series plots are provided in Sections 4.5.1 and 4.5.2.

Table 4-9 Overview of emission fluxes/rates of CH<sub>4</sub> and CO<sub>2</sub> calculated by EddyPro.

	<b>CH<sub>4</sub> kg/(m<sup>2</sup>-day)</b>	<b>CH<sub>4</sub> kg/hour</b>	<b>CO<sub>2</sub> kg/(m<sup>2</sup>-day)</b>	<b>CO<sub>2</sub> (kg/hour)</b>
Min	-0.2	-288.2	-0.7	-1024.4
Max	0.1	201.0	1.4	2118.8
Median	9.2×10 <sup>-3</sup>	13.7	3.9×10 <sup>-2</sup>	58.0
Average	9.7×10 <sup>-3</sup>	14.4	5.4×10 <sup>-2</sup>	80.6

Note: concentrations shown are 30-min averages for EC data.

#### 4.5.1 Time Series of CH<sub>4</sub> Emission flux

As shown in Figure 4-25 (A), the emission fluxes of CH<sub>4</sub> were around 9.2 × 10<sup>-3</sup> kg/m<sup>2</sup>-day (median value). The median emission flux is consistent with a previous study (8.0 × 10<sup>-3</sup> kg/m<sup>2</sup>-day) on the same lagoon (Brown 2013). A close look at the majority of the CH<sub>4</sub> emission fluxes (Figure 4-25 (B)) indicates a similar trend (increase, drop, and then rise) with that of the time series of temperature (Figure 4-4) for the whole field campaign. Emission fluxes of CH<sub>4</sub> are also plotted against temperature given in Section 4.5.3.

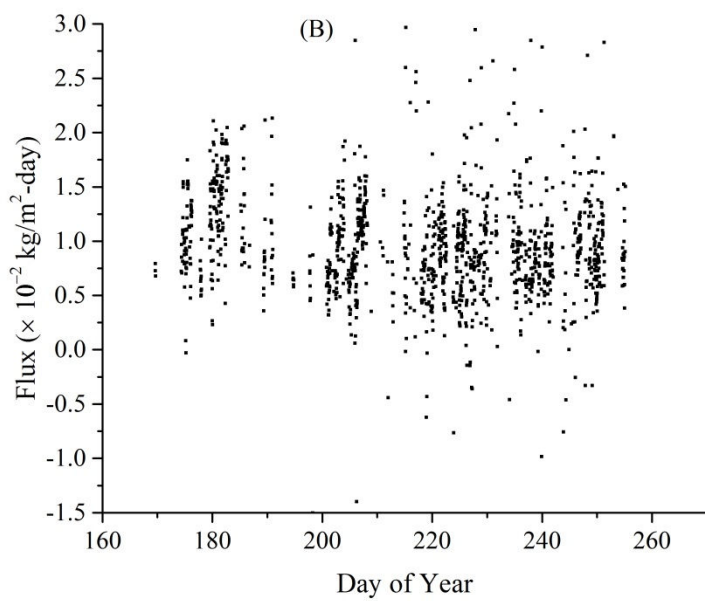
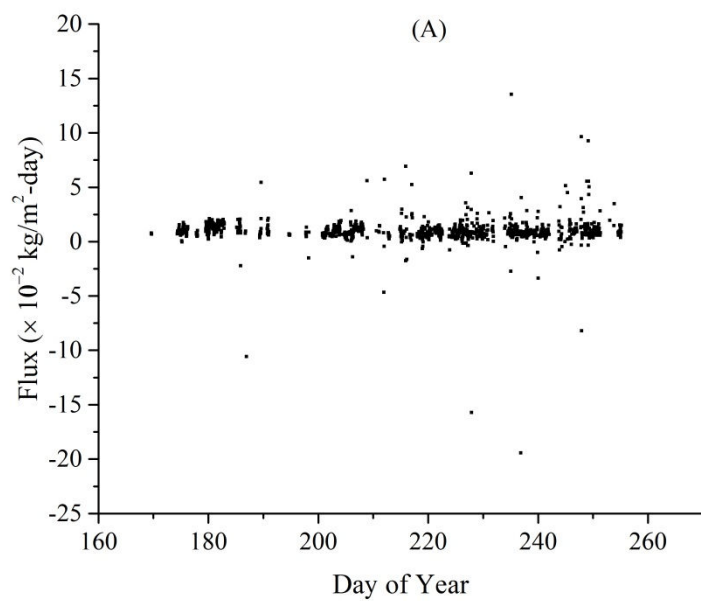
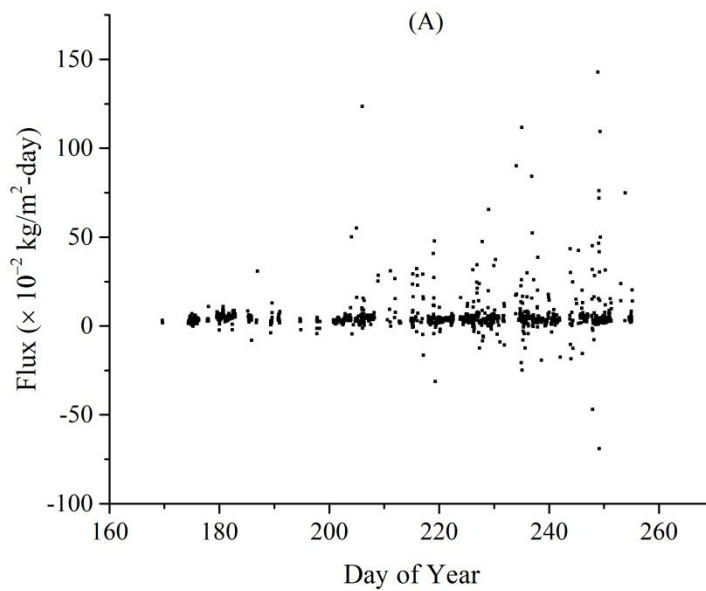


Figure 4-25 Time series of CH<sub>4</sub> emission fluxes (filtered data). (A): full scale; (B): zoom in.

#### 4.5.2 Time Series of CO<sub>2</sub> Emission flux

The median emission flux of CO<sub>2</sub> ( $3.9 \times 10^{-2}$  kg/m<sup>2</sup>-day), as depicted in Figure 4-26, is comparable to that ( $2.4 \times 10^{-2}$  kg/m<sup>2</sup>-day) reported by a previous study on the same lagoon (Brown 2013). Similar to the case for CH<sub>4</sub>, a zoomed in view of the time series of emission fluxes of CO<sub>2</sub> shows a consistent trend with that of the time series of temperature as indicated in Figure 4-4. The emission fluxes of CO<sub>2</sub> are also potted against temperature, shown in Section 4.5.3.



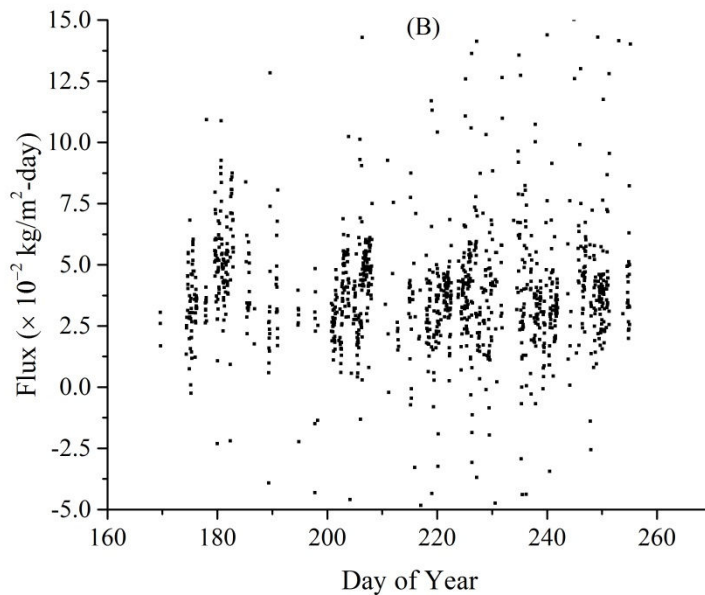
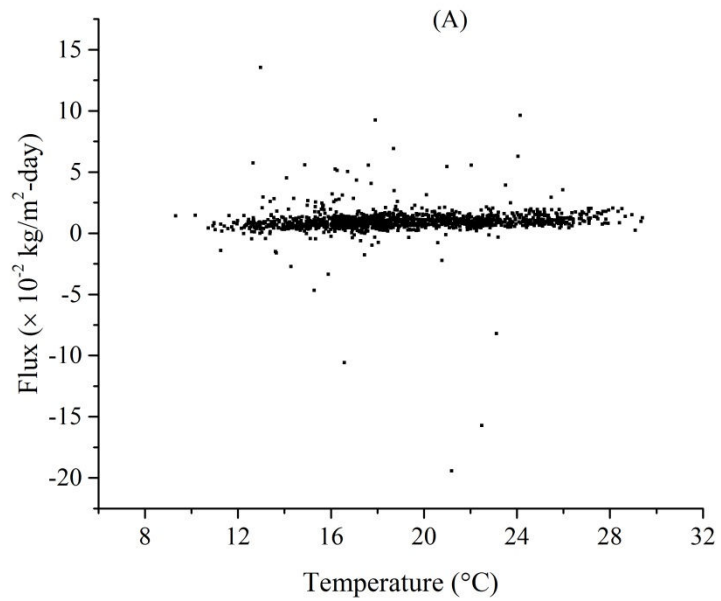


Figure 4-26 Time series of CO<sub>2</sub> emission (filtered data). (A): full scale; (B): composite diurnal variation (averages of all days data for each 30-min time interval).

#### 4.5.3 Emission Flux and Temperature

It is stated in previous Sections 4.5.1 and 4.5.2 that the time series of emission fluxes of CH<sub>4</sub> and CO<sub>2</sub> are found to be correlated to the time series of temperature. Thus, it would be interesting to see emission fluxes plotted against temperature directly (given as Figures 4-27 and 4-28). For CH<sub>4</sub>, the emission flux increased from around  $0.5 \times 10^{-2} \text{ kg/m}^2\text{-day}$  to  $1.2 \times 10^{-2} \text{ kg/m}^2\text{-day}$  (140% increase), as the temperature increased from around 12 °C to 29 °C. For CO<sub>2</sub>, the emission flux increased from around  $1.7 \times 10^{-2} \text{ kg/m}^2\text{-day}$  to  $5.1 \times 10^{-2} \text{ kg/m}^2\text{-day}$ , a 200% jump, as the temperature increased from around 12 °C to around 29 °C. The reason for

the increasing emission fluxes might be that microorganisms' activities are stronger at higher temperatures and thus more gases can be emitted. No diurnal trend of the emission fluxes is evident.



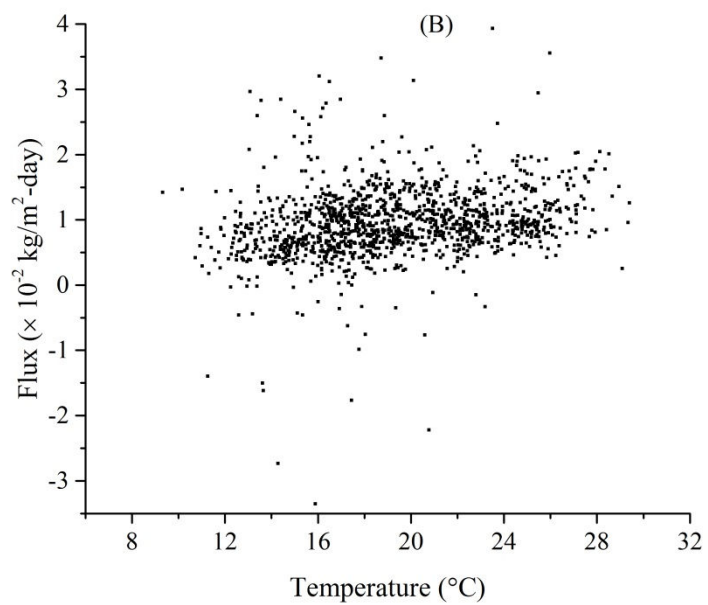


Figure 4-27 CH<sub>4</sub> emission fluxes potted against temperature (filtered data). (A): full scale; (B): zoom in.

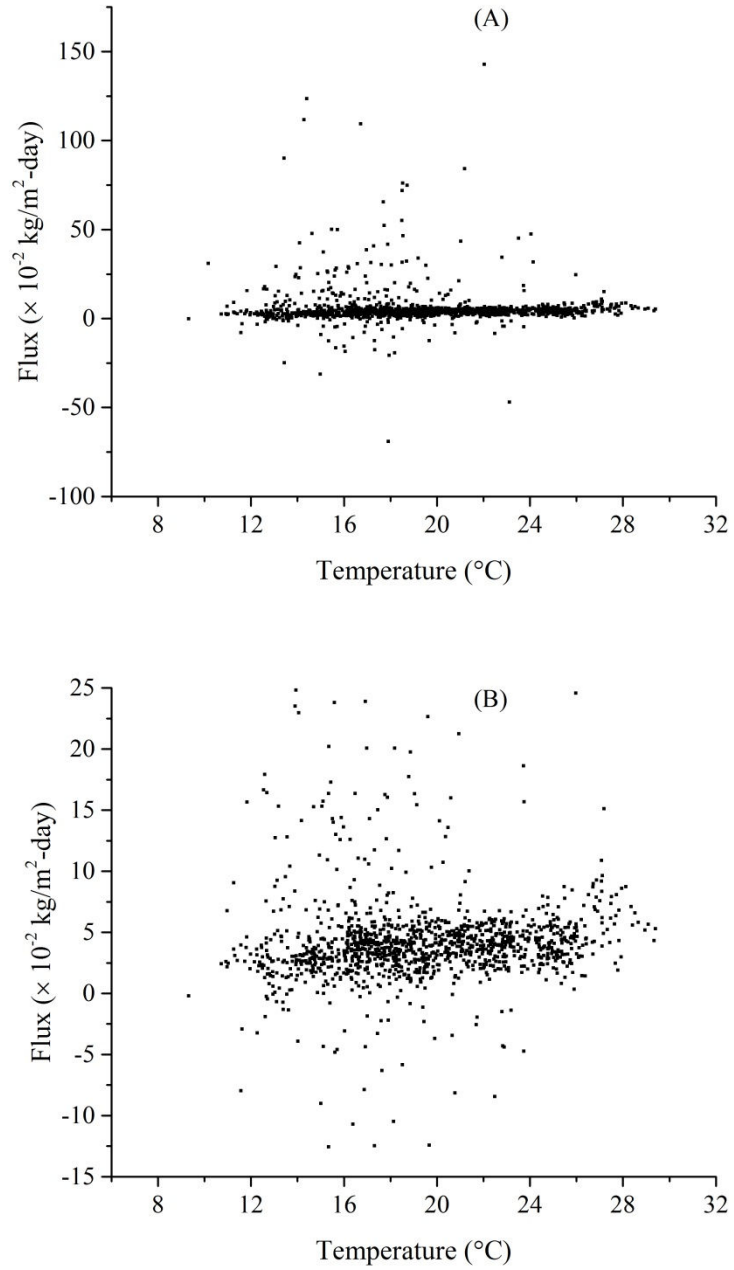


Figure 4-28 CO<sub>2</sub> emission fluxes plotted against temperature (filtered data). (A): full scale; (B): zoom in.

#### 4.5.4 Emission Flux and Wind Speed

Time series of CH<sub>4</sub> and CO<sub>2</sub> emission fluxes are shown in Figures 4-29 and 4-30. Similar patterns (triangles) are noted for the relationships between emission fluxes and wind speeds for CH<sub>4</sub> and CO<sub>2</sub>. Extreme flux values (including negative values) were recorded at low wind speeds (0 m/s – 2 m/s), which might be caused by the fact that sonic anemometers do not work well at low wind speed when turbulent transport may not be dominant. As the wind speed increased to 4 m/s, the minimum emission fluxes of CH<sub>4</sub> and CO<sub>2</sub> increased; however, their maximum emission fluxes decreased. In other words, the spreads of CH<sub>4</sub> and CO<sub>2</sub> emission fluxes narrowed as the wind speeds increased. Lowest and highest emission fluxes were observed at low wind speeds. For wind speeds between 4 m/s and 8 m/s, only a small amount of data points are available and thus no clear trend could be recognized. As discussed in Section 4.3.4, concentrations of CH<sub>4</sub> and CO<sub>2</sub> decrease with increasing  $\bar{u}$  while standard deviation of vertical speed ( $\sigma_w$ ) increases with increasing  $\bar{u}$  (Figure 4-31). In other words, the flux can either increase or decrease as  $\bar{u}$  increases, which might explain the relationship between emission fluxes and wind speeds discussed above.

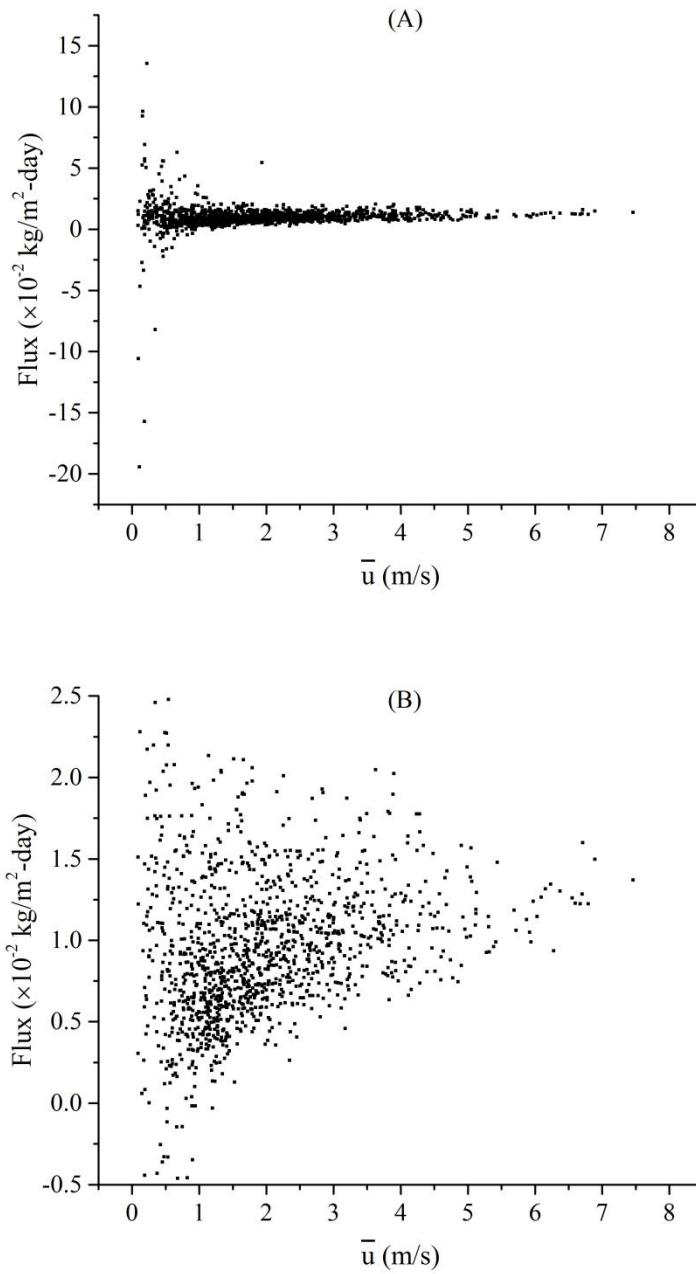


Figure 4-29 Emission fluxes of CH<sub>4</sub> plotted against wind speed (filtered data). (A): full scale; (B): zoom in.

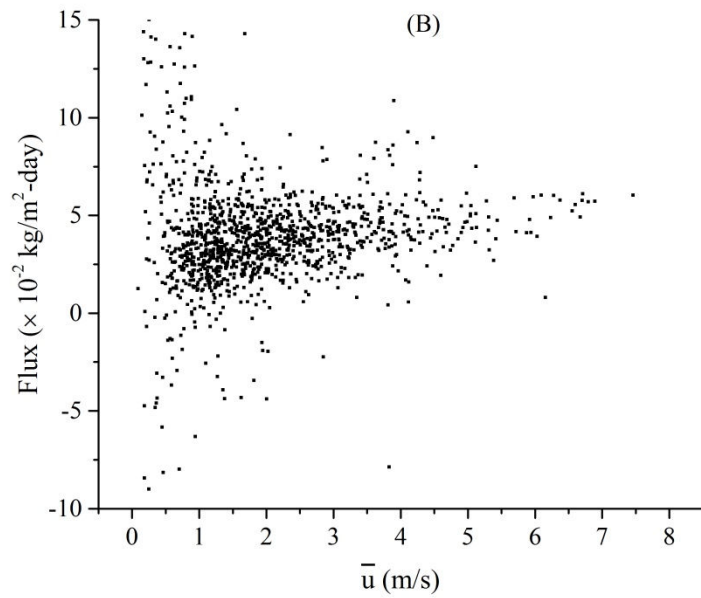
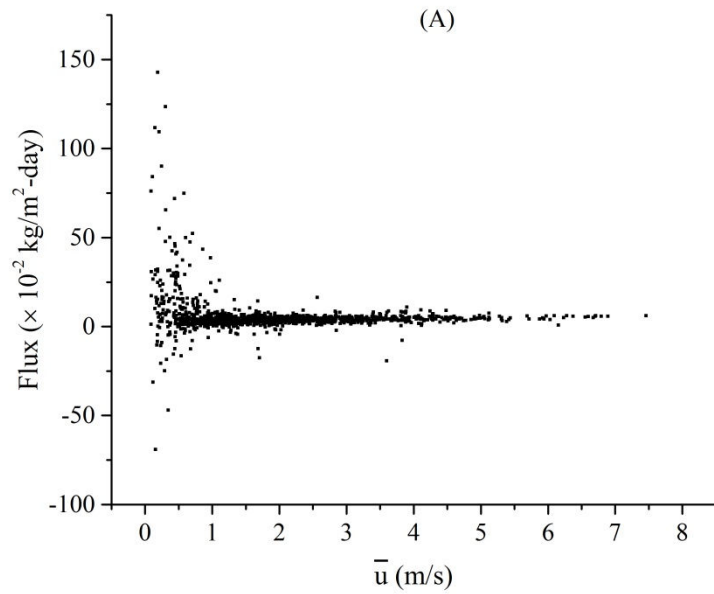


Figure 4-30 Emission fluxes of CO<sub>2</sub> plotted against wind speed (filtered data). (A): full scale; (B): zoom in.

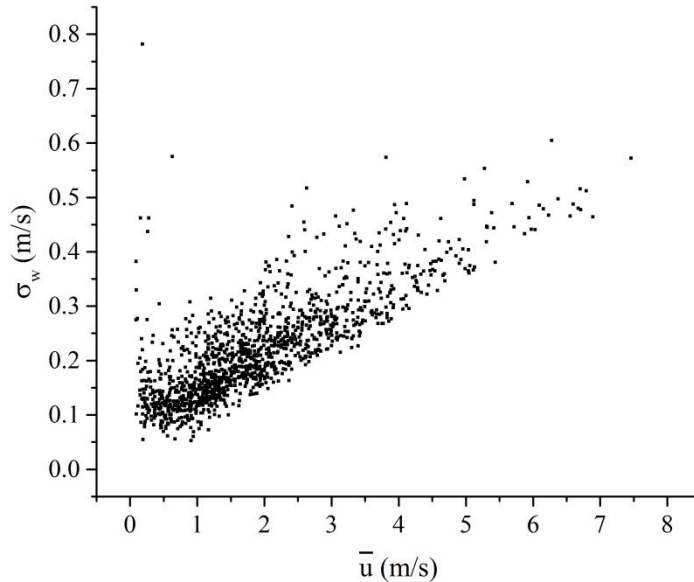
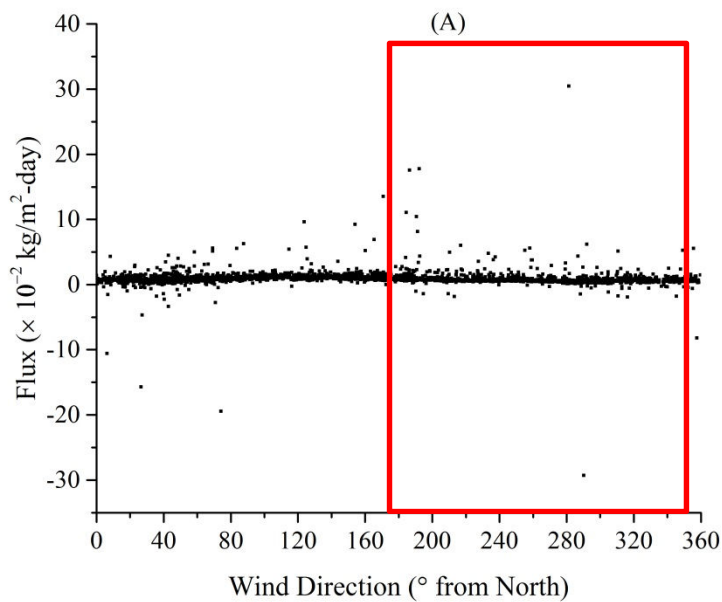


Figure 4-31 Vertical wind speed standard deviation plotted against mean horizontal wind speed (filtered data).

#### 4.5.5 Emission flux and Wind Direction

As stated in Section 4.1.3, only 27% of the data were obtained under favorable mean wind directions (between  $90^\circ$  and  $150^\circ$  or  $120^\circ \pm 30^\circ$ ). To identify the impact of the air flow disturbances by the EC system on fluxes, data deemed to be of uncertain quality are included (in red boxes in Figures 4-32 and 4-33). As can be seen from Figures 4-32 (B) and 4-33 (B), emission fluxes of  $\text{CH}_4$  were highest ( $\sim 1.2 \times 10^{-2} \text{ kg/m}^2\text{-day}$ ) at wind directions around  $120^\circ$ , the ideal wind direction as discussed above and in Section 4.1.3;  $\text{CO}_2$  emission fluxes were higher ( $\sim 3.7 \times 10^{-2} \text{ kg/m}^2\text{-day}$ ) at around  $120^\circ$  than at  $0^\circ$  to  $90^\circ$ . For the discarded data, the emission fluxes are at lowest levels at around  $280^\circ$  for both  $\text{CH}_4$  and  $\text{CO}_2$ . Note

that at around 280° (west wind), the wind was coming almost directly from the back of the sonic anemometer while the L<sub>90</sub> was representative of the lagoon (details will be given in Section 4.5.8). Thus, it is possible that the decreased levels of emission fluxes at west wind are caused to some extent by the flow disturbance of the structure of the mounting hardware, the sonic head, as well as other instruments mounted beside the sonic anemometer (refer to Figure 4-2).



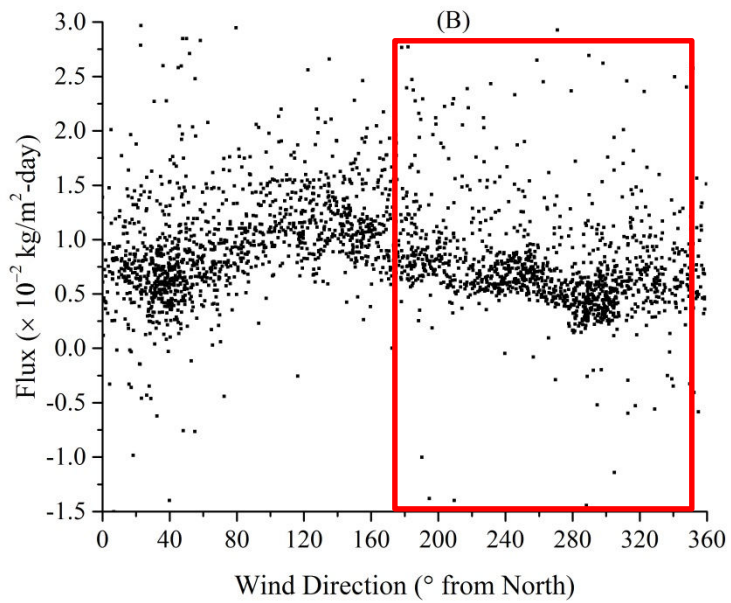
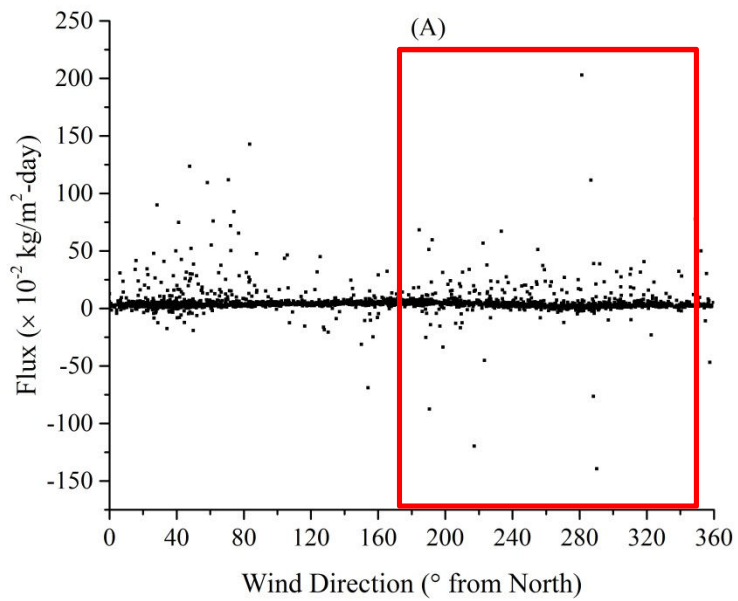


Figure 4-32 Emission flux of CH<sub>4</sub> plotted against wind direction (filtered data).

(A): full scale; (B): zoom in.



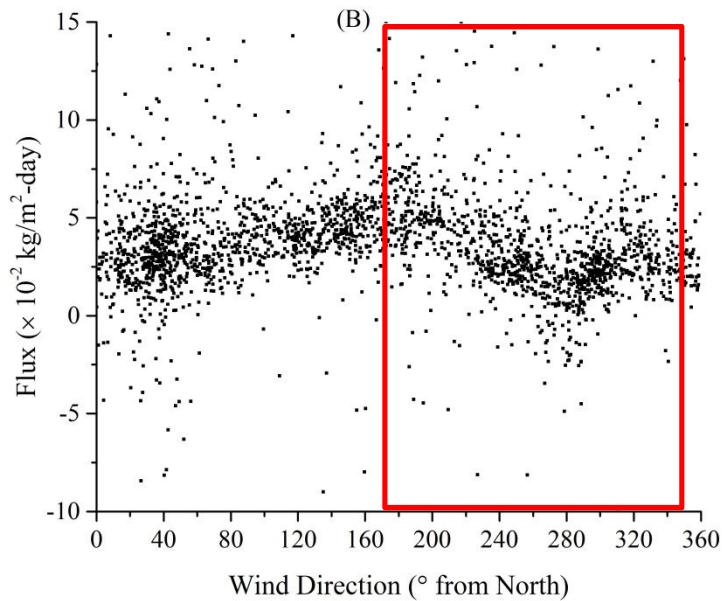


Figure 4-33 Emission flux of CO<sub>2</sub> plotted against wind direction (filtered data). (A): full scale; (B): zoom in.

Table 4-10 shows emission fluxes of CH<sub>4</sub> and CO<sub>2</sub> derived using ID and EC techniques. As discussed in Section 4-2, the prevailing wind for Day 3 (August 21, 2013) of the OP-FTIR field campaign was west wind. Thus the meteorological measurements, including some of the input parameters (e.g.  $u_*$  and  $L$ ) for WindTrax, are of uncertain quality for the reason discussed above. However, since there were very limited data from the short-term OP-FTIR field campaign, the emission fluxes calculated by EddyPro for the corresponding time periods were pulled out just for comparison. Interestingly, despite of the concerns discussed, the emission fluxes calculated by the two methods were comparable (see Table 4-10). In addition, the  $L_{90}$  during the comparison time periods was just beyond the upwind (west) edge of the studied lagoon, indicating that the emission

fluxes by the EC technique were at least representative of the west part of the lagoon in study. In other words, by using the same set of meteorological observations (parameters), though questionable in terms of the accuracy of the sonic anemometer data and associated EC fluxes, the two techniques (ID and EC) yielded consistent results for CH<sub>4</sub> emission fluxes. Note that the emission fluxes calculated by EC technique in Table 4-10 were typical values (see Figure 4-32) for a west wind during the whole EC field campaign.

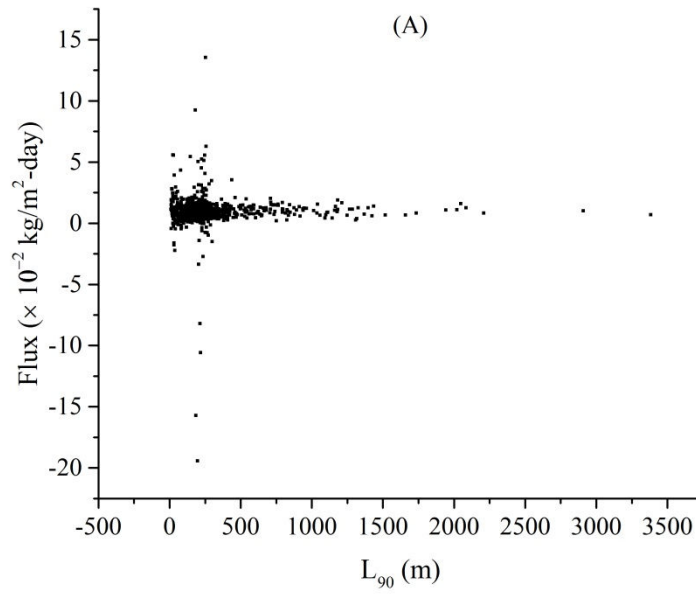
Table 4-10 Comparison of emission fluxes of CH<sub>4</sub> calculated by ID and EC techniques

Date	Time	CH <sub>4</sub> ID	CH <sub>4</sub> EC	ID/EC	EC L <sub>90</sub>	EC to Upwind Edge
		× 10 <sup>-3</sup> kg/m <sup>2</sup> -day	× 10 <sup>-3</sup> kg/m <sup>2</sup> -day	%	m	m
08/21/2013	1330	4.7	4.2	111	132	111
08/21/2013	1400	5.2	4.3	122	127	111
08/21/2013	1430	4.3	3.3	129	129	111
08/21/2013	1500	4.5	4.0	111	113	111

#### 4.5.6 Emission Flux and L<sub>90</sub>

The L<sub>90</sub> estimates presented are calculated by EddyPro using models from the literature (Kljun et al. 2004, Kormann and Meixner 2001). As mentioned in Section 2.4, details of these models are provided in Appendix B. As depicted in Figures 4-34 and 4-35, the majority of the emission fluxes are around  $0.9 \times 10^{-2}$  kg/m<sup>2</sup>-day (median) for CH<sub>4</sub> and  $3.9 \times 10^{-2}$  kg/m<sup>2</sup>-day (median) for CO<sub>2</sub> at L<sub>90</sub> of about 150 m. Based on the size and shape of the lagoon as depicted in Section 4.1, at fetch of about 150 m, wind directions should approximately be between 90°

and  $150^\circ$ , in order for the fetch to be representative of the lagoon. More details about fetch and wind direction will be given in Section 4.5.8.



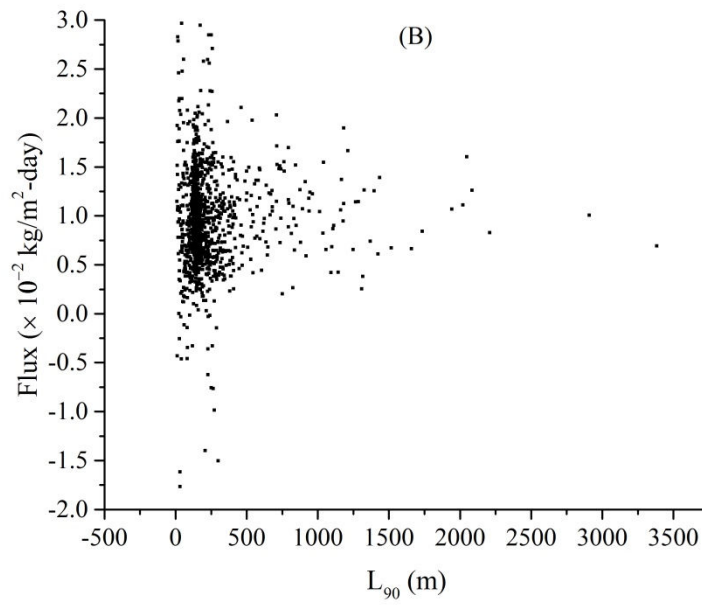


Figure 4-34 Emission Flux of CH<sub>4</sub> plotted against L<sub>90</sub> (filtered data). (A): full scale; (B): zoom in.

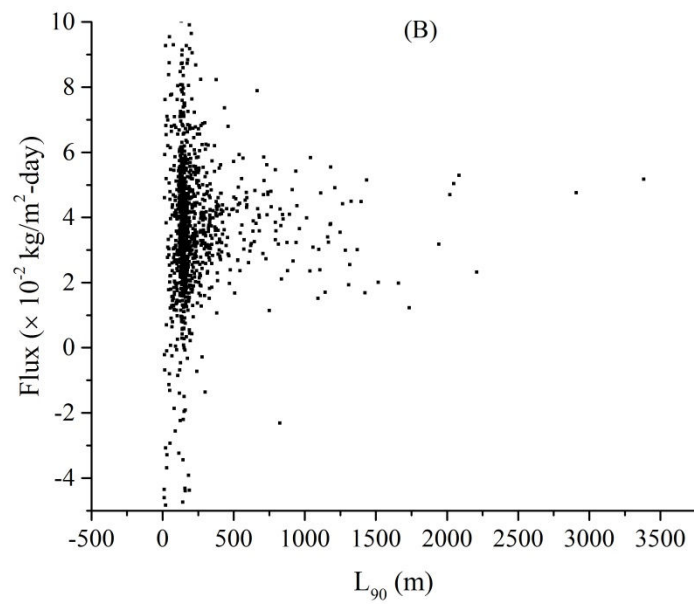
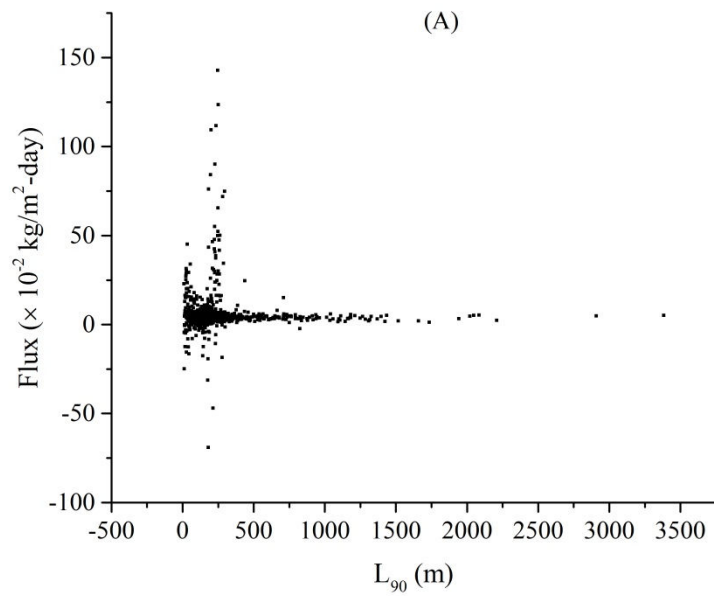


Figure 4-35 Emission flux of CO<sub>2</sub> plotted against  $L_{90}$  (filtered data). (A): full scale; (B): zoom in.

#### 4.5.7 $L_{90}$ and Wind Speed

It is reported that footprint estimates can vary strongly with different receptor height, atmospheric stability, and surface roughness (Kljun et al. 2004). Although  $\bar{u}$  is not reported to impact footprint estimates, it would still be interesting to see how fetch would change with  $\bar{u}$  as it is a common meteorological observation. As shown in Figure 4-36, a turn point at around 1.5 m/s is easily identified. At higher wind speeds ( $2 \text{ m/s} < \bar{u} < 8 \text{ m/s}$ ), the majority of the  $L_{90}$  are fairly stable ( $\sim 150 \text{ m}$ ) compared to those ( $\sim 10 \text{ m}$  to hundreds of meters) at lower wind speeds ( $\bar{u} < 2 \text{ m/s}$ ). A close look at the relationship between wind speed and stability (see Figure 4-37) shows that at higher wind speeds, the span of the stability narrows down to around neutral condition. In contrast, at lower wind speeds, more unstable and stable conditions were observed. Since  $L$  is proportional to  $u_*^3$  (Equation 2-2) and  $\bar{u}$  is proportional to  $u_*$ , thus,  $z/L$  is closer to 0 (neutral) at higher  $\bar{u}$ . A direct look at the relationship between  $L_{90}$  and stability, as presented in Figure 4-38, indicates that at unstable to neutral conditions ( $-12 < z_m/L < 0$ ) the majority of the  $L_{90}$  were within 250 m. However, once the atmosphere became stable, fetches became widely spread because vertical transport is suppressed in stable stratification.

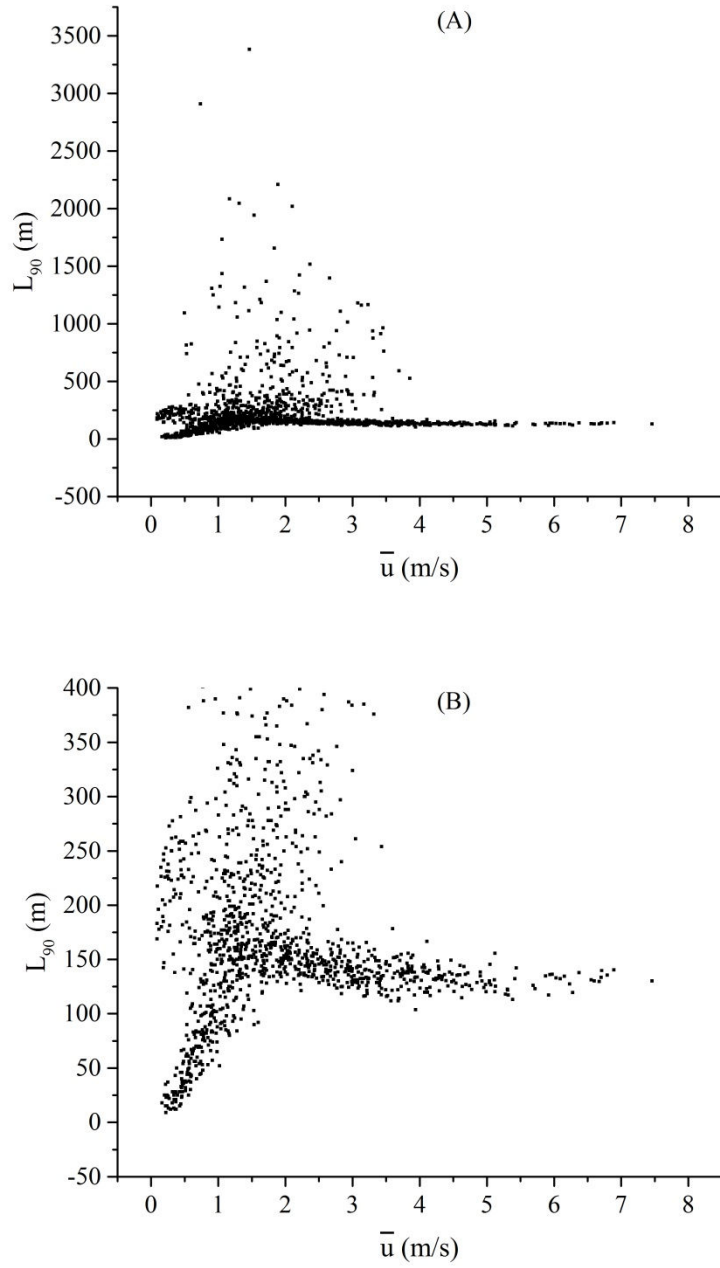


Figure 4-36  $L_{90}$  calculated by EddyPro plotted against  $\bar{u}$  (filtered data). (A): full scale; (B): zoom in.

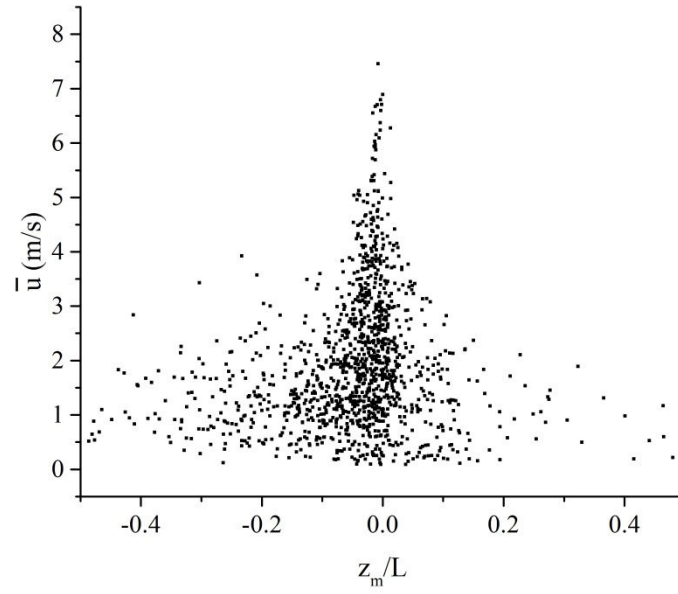


Figure 4-37  $\bar{u}$  plotted against  $z_m/L$  (filtered data).

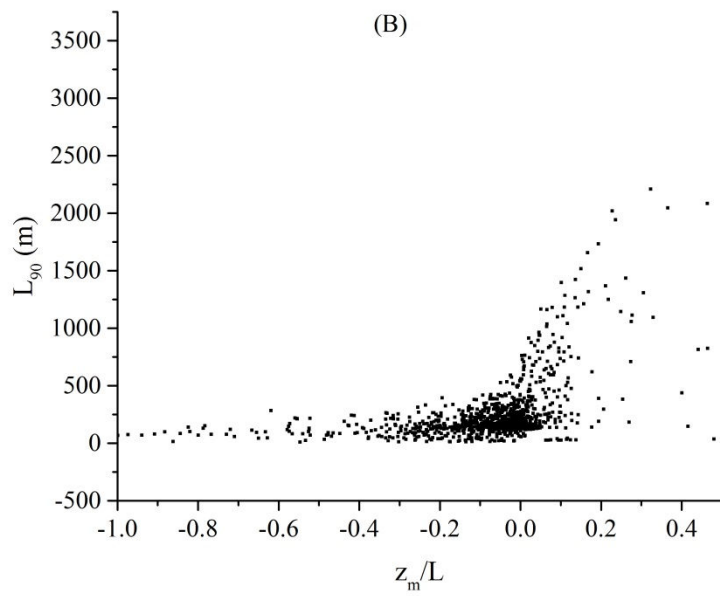
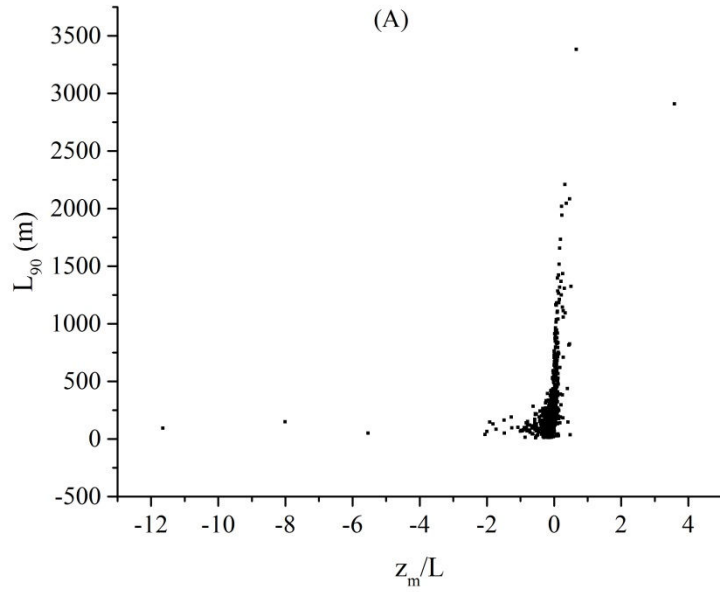


Figure 4-38  $L_{90}$  calculated by EddyPro plotted against  $z_m/L$  (filtered data). (A): full scale; (B): zoom in.

#### 4.5.8 $L_{90}$ and Wind Direction

Schematic indication of fetches (lengths and angles of the lines are sized and positioned approximately relative to the lagoon) are sketched on aerial image of the lagoon in Figure 4-39. As discussed in Section 4.1.3, most of the time the wind was from the northeast (shown as the green line). At a typical wind direction, the fetch (typically ~150 m) would reach the lagoon #4 (refer to Figure 4-1) and thus the emission fluxes at this wind direction are generally not representative of the lagoon in study (Lagoon #1). However, the emission fluxes measured at wind directions of  $120^\circ \pm 30^\circ$  (shown as the red line at about  $120^\circ$ ) can be chosen as the most representative values for the lagoon. As discussed in Section 4.5.5, at around  $120^\circ$ , the emission fluxes of  $\text{CH}_4$  and  $\text{CO}_2$  are around  $1.1 \times 10^{-2} \text{ kg/m}^2\text{-day}$  and  $3.7 \times 10^{-2} \text{ kg/m}^2\text{-day}$ , respectively. For the OP-FTIR field campaign, despite the fact that the wind directions were not favorable, the typical  $L_{90}$  (shown as the blue line) was just across the west edge of the lagoon, making it most representative of the west part of the lagoon (from EC sensors, shown as yellow cross, to the west edge). The  $L_{90}$  are also plotted against wind directions given as Figure 4-40, which can help determine the wind directions (green and red lines) in Figure 4-39.

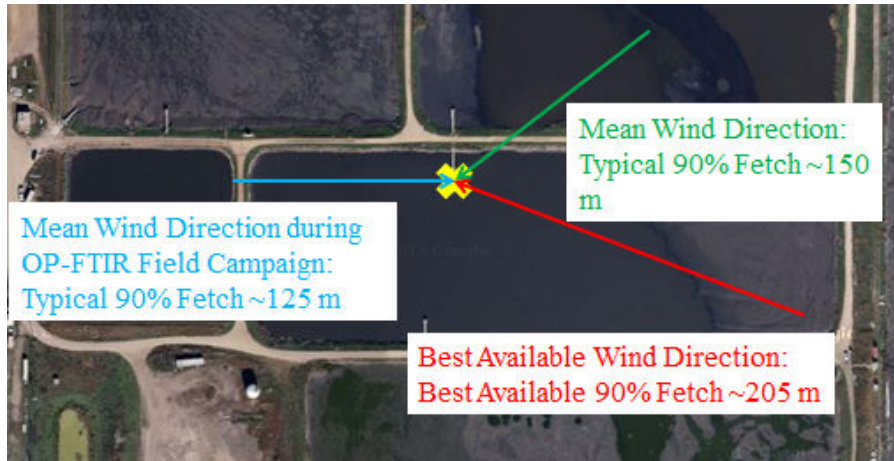


Figure 4-39 Schematic of  $L_{90}$  and wind directions at certain conditions.

Note: typical  $L_{90}$  at mean horizontal wind direction (around  $70^\circ$ ) (Green line); best available  $L_{90}$  at best available (optimal) wind direction (around  $120^\circ$ ) (red line); and typical  $L_{90}$  during the OP-FTIR field campaign (blue line).

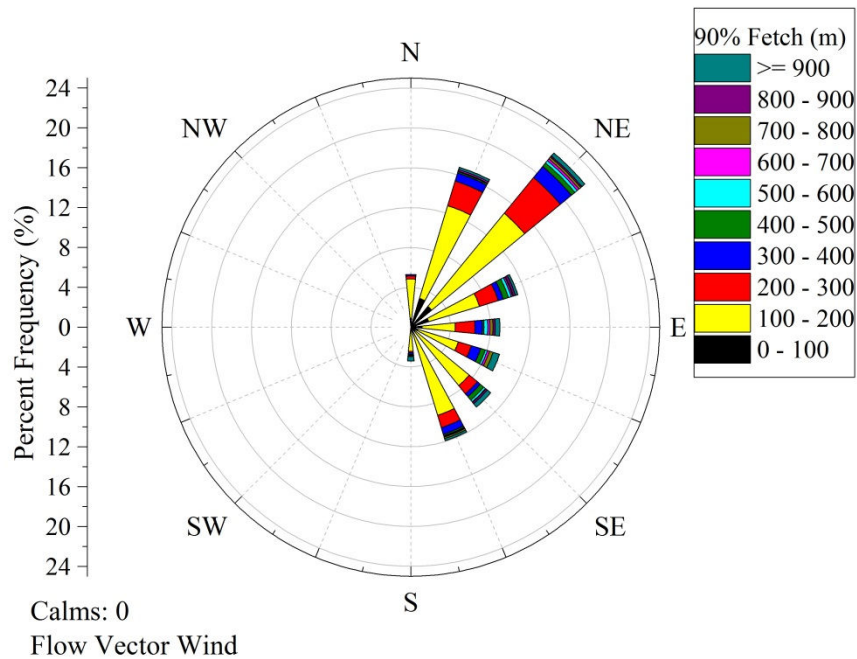


Figure 4-40  $L_{90}$  rose (filtered data)

#### 4.5.9 50% Source Area

A parameterized scalar flux-source area model (mini-FSAM) (Schmid 1994) was used to estimate the 50% source area of the flux measurements. As mentioned in Section 2.4, details of the model are given in Appendix A. A sample of the input data and the VBA code for the calculation are also provided in Appendix G. Calculated parameters defining the position and shape of the 50% source area for Day 3 of the OP-FTIR field campaign and for the whole EC field campaign are presented in Table 4-11 and 4-12, respectively. As can be seen from the Tables, most of the parameters are consistent with each other except the maximum width (“d”) for the two campaigns. As a result, as shown in Figure 4-41, the 50% area during the EC campaign (blue area) is narrower than that during the OP-FTIR campaign (green area). The 50% source area during the OP-FTIR campaign is sketched using the average of the parameters in Table 4-11 at west wind (prevailing wind) while the 50% source area during the EC campaign is sketched using the median values given in Table 4-12 at southeast wind (favorable wind direction). In general, the majority of the 50% source areas spreads from about 12 m to about 38 m upwind along the wind direction with maximum widths of less than 10 meters.

Table 4-11 Calculated parameters using mini-FSAM model for estimating 50% source area for Day 3 of the OP-FTIR field campaign

Time	a (m)	e (m)	d (m)	$x_d$ (m)	$x_m$ (m)	$A_r$ (m <sup>2</sup> )
1330	12.1	37.6	7.2	25.8	18.7	288
1400	13.5	41.4	8.8	28.0	21.3	379
1430	14.2	40.7	7.9	28.1	22.0	370
1500	11.7	36.3	9.3	24.9	17.8	358
Average	12.9	39.0	8.3	26.7	20.0	349

Table 4-12 Medians of the calculated parameters for estimating 50% source area using mini-FSAM model for the whole EC field campaign

Time	a (m)	e (m)	d (m)	$x_d$ (m)	$x_m$ (m)	$A_r$ (m <sup>2</sup> )
All	12.1	37.5	5.1	25.6	18.6	195.9

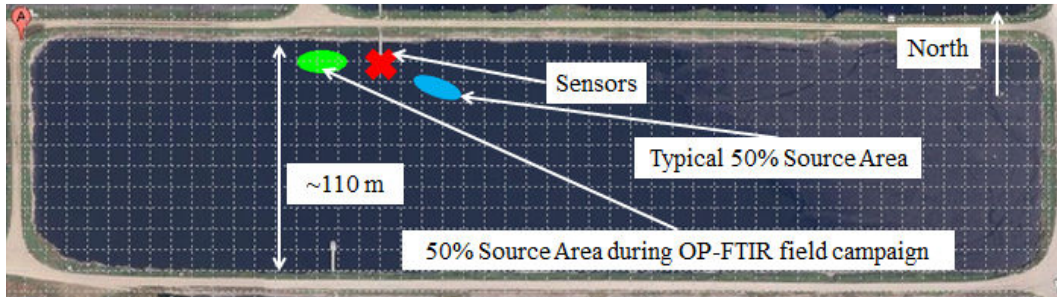


Figure 4-41 Schematic representation of the 50% source area for the average of Day 3 of OP-FTIR field campaign and for the median of the whole EC field campaign (filtered data).

#### 4.6 Limitations of the Measurement Techniques

As depicted in Figure 4-1, the studied lagoon is surrounded by several other lagoons. Lagoon #5 is a couple of meters higher than the Lagoon #1 and thus the air flow could be disturbed. Even so, the relationship between the vertical velocity

turbulent intensity and stability agrees with the model given by Wilson (2008) for an undisturbed surface layer, as depicted in Figure 4-5. The almost three month duration of the EC field campaign allowed favorable wind directions and fetches to be obtained.

The OP-FTIR needs liquid nitrogen for cooling purpose and a gasoline generator for power supply. In addition, OP-FTIR is not rain-proof and thereby it was necessary to transport the OP-FTIR system back and forth daily when the weather permitted. Another limitation was that only one OP-FTIR was available for the OP-FTIR field campaign, though two OP-FTIRs were necessary for quantifying emission fluxes using the ID technique, ideally. Unfortunately, the wind directions during the OP-FTIR field campaign were not favorable (mostly west wind) based on the orientation of the sonic anemometer. As a result, the emission fluxes calculated using the ID technique should be evaluated carefully. Nevertheless, the OP-FTIR field campaign provided valuable information including the concentrations of CH<sub>4</sub> and NH<sub>3</sub> and allowed calculating the emission fluxes and rates of CH<sub>4</sub> and NH<sub>3</sub>.

## Chapter 5 Conclusions

An Eddy Covariance system was used to continuously measure fugitive emissions of methane and carbon dioxide off a biosolids lagoon for about three months (from mid-June to mid-September). Open Path Fourier Transform Infrared (OP-FTIR) was also used to quantify concentrations of methane and ammonia at several locations along the lagoon edges for five days. Both Eddy Covariance and Inverse Dispersion techniques were used to quantify fugitive emission fluxes of methane, carbon dioxide and/or ammonia.

The relationship between the normalized standard deviation of vertical velocity ( $\sigma_w/u^*$ ) and stability  $|z/L|$  (unstable conditions only) agreed with the relationship expected (Wilson 2008) for an undisturbed surface layer. For the Eddy Covariance results, diurnal patterns of concentrations of  $\text{CH}_4$  and  $\text{CO}_2$  were identified. The highest concentrations of  $\text{CH}_4$  and  $\text{CO}_2$  were observed at around midnights and in the early mornings, respectively. Concentrations of  $\text{CH}_4$  and  $\text{CO}_2$  were typically higher at lower wind speeds and lower temperatures at nights when inversion could often happen. Higher concentrations of  $\text{CH}_4$  and  $\text{CO}_2$  were recorded during northeast wind directions while lower concentrations were seen during southeast winds. Generally, emission fluxes of  $\text{CH}_4$  and  $\text{CO}_2$  were found to be higher at higher temperatures, higher wind speeds and southeast wind directions. At favorable wind directions ( $-4.9^\circ$  to  $175.1^\circ$ ,  $\sim 27\%$  of the data points after filtering)  $L_{90}$  with acceptable flux footprints ( $\sim 150$  m), the typical emission

fluxes of CH<sub>4</sub> and CO<sub>2</sub> were around  $1.1 \times 10^{-2}$  kg/m<sup>2</sup>-day and  $3.7 \times 10^{-2}$  kg/m<sup>2</sup>-day, respectively. These emission fluxes are close to the median emission fluxes ( $0.9 \times 10^{-2}$  kg/m<sup>2</sup>-day and  $3.9 \times 10^{-2}$  kg/m<sup>2</sup>-day, respectively) of the whole field campaign. Although the wind direction was not favorable for the EC system on the one day that ID estimates of fluxes were available, by sharing the same set of meteorological data, results from the OP-FTIR field campaign showed that the emission fluxes of CH<sub>4</sub> simulated using Inverse Dispersion technique were consistent with the CH<sub>4</sub> emission fluxes derived using Eddy Covariance technique.

## References

- Allen, D.T., Torres, V.M., Thomas, J., et al. 2013. Measurements of methane emissions at natural gas production sites in the united states. *Proceedings of the National Academy of Sciences* **110**(44): 17768-17773.
- Amstel, A.v., Reay, D., and Smith, P. 2010. *Methane and climate change*. London; Washington, DC: Earthscan.
- Aneja, V.P., Arya, S.P., Rumsey, I.C., et al. 2008. Characterizing ammonia emissions from swine farms in eastern north carolina: Part 2—potential environmentally superior technologies for waste treatment. *Journal of the Air & Waste Management Association* **58**(9): 1145-1157.
- Aneja, V.P., Malik, B.P., Tong, Q., et al. 2001. Measurement and modelling of ammonia emissions at waste treatment lagoon-atmospheric interface. *Water, Air and Soil Pollution: Focus* **1**(5-6): 177-188.
- Arya, P.S. 2001. *Introduction to micrometeorology*. Academic Press, San Diego, California.
- Asman, W.A., Sutton, M.A., and Schjørring, J.K. 1998. Ammonia: Emission, atmospheric transport and deposition. *New Phytologist* **139**(1): 27-48.
- Baker, J., Norman, J., and Bland, W. 1992. Field-scale application of flux measurement by conditional sampling. *Agricultural and Forest Meteorology* **62**(1): 31-52.
- Battye, W., Aneja, V.P., and Roelle, P.A. 2003. Evaluation and improvement of ammonia emissions inventories. *Atmospheric Environment* **37**(27): 3873-3883.
- Bjorneberg, D., Leytem, A., Westermann, D., et al. 2009. Measurement of atmospheric ammonia, methane, and nitrous oxide at a concentrated dairy production facility in southern idaho using open-path fir spectrometry. *Transactions of the ASABE* **52**(5): 1749-1756.
- Brown, C. 2013. Quantifying methane emissions from an oil sands tailings pond using micrometeorological flux measurement techniques. Master's Thesis, Department of Earth and Atmospheric Sciences, University of Alberta, Edmonton, Alberta.
- Brown, S., Beecher, N., and Carpenter, A. 2010. Calculator tool for determining greenhouse gas emissions for biosolids processing and end use. *Environmental Science & Technology* **44**(24): 9509-9515.

Burba, G. 2013. Eddy covariance method for scientific, industrial, agricultural, and regulatory applications. LI-COR, Inc., Lincoln, Nebraska.

City of Edmonton. 2013. Biosolids management. [http://www.edmonton.ca/environmental/wastewater\\_sewers/biosolids-management.aspx](http://www.edmonton.ca/environmental/wastewater_sewers/biosolids-management.aspx) (Retrieved as of Nov. 1, 2013).

Czepiel, P., Mosher, B., Harriss, R., et al. 1996. Landfill methane emissions measured by enclosure and atmospheric tracer methods. *Journal of Geophysical Research: Atmospheres* (1984–2012) **101**(D11): 16711-16719.

Denmead, O.T. 2008. Approaches to measuring fluxes of methane and nitrous oxide between landscapes and the atmosphere. *Plant and Soil* **309**(1-2): 5-24.

Desjardins, R., Buckley, D., and Amour, G.S. 1984. Eddy flux measurements of CO<sub>2</sub> above corn using a microcomputer system. *Agricultural and Forest Meteorology* **32**(3): 257-265.

Dyer, A.J., and Bradley, E.F. 1982. An alternative analysis of flux-gradient relationships at the 1976 itce. *Boundary-Layer Meteorology* **22**(1): 3-19.

Environment Canada. 2013. Ammonia emissions. <http://www.ec.gc.ca/indicateurs-indicators/default.asp?lang=en&n=FE578F55-1> (Retrieved as of Nov. 1, 2013).

Flesch, T., Wilson, J., Harper, L., et al. 2007. Determining ammonia emissions from a cattle feedlot with an inverse dispersion technique. *Agricultural and Forest Meteorology* **144**(1): 139-155.

Flesch, T.K., Wilson, J.D., Harper, L.A., et al. 2005. Estimating gas emissions from a farm with an inverse-dispersion technique. *Atmospheric Environment* **39**(27): 4863-4874.

Flesch, T.K., Wilson, J.D., and Yee, E. 1995. Backward-time lagrangian stochastic dispersion models and their application to estimate gaseous emissions. *Journal of Applied Meteorology* **34**(6): 1320-1332.

Franks, P.J., Adams, M.A., Amthor, J.S., et al. 2013. Sensitivity of plants to changing atmospheric CO<sub>2</sub> concentration: From the geological past to the next century. *New Phytologist* **197**(4): 1077-1094.

Griffith, D.W., Bryant, G.R., Hsu, D., et al. 2008. Methane emissions from free-ranging cattle: Comparison of tracer and integrated horizontal flux techniques. *Journal of Environmental Quality* **37**(2): 582-591.

Hashisho, Z., Small, C.C., and Morshed, G. 2012. Review of technologies for the characterization and monitoring of vocs, reduced sulphur compounds and ch<sub>4</sub>. Oil Sands Research and Information Network, University of Alberta, School of Energy and the Environment, Edmonton, Alberta.

Hashmonay, R.A., Varma, R.M., Modrak, M.T., et al. 2008. Radial plume mapping: A u.S. Epa test method for area and fugitive source emission monitoring using optical remote sensing. *In* Advanced environmental monitoring. *Edited by* Y.J. Kim and U. Platt. Springer Netherlands.

Hewitt, C.N., and Jackson, A.V. 2009. Atmospheric science for environmental scientists. Chichester, UK ; Hoboken, NJ : Wiley-Blackwell.

Horst, T. 1999. The footprint for estimation of atmosphere-surface exchange fluxes by profile techniques. *Boundary-Layer Meteorology* **90**(2): 171-188.

IPCC. 2007. Climate change 2007: Working group i: The physical science basis. Cambridge University Press, Cambridge, UK.

IPCC. 2007a. Climate change 2007: Synthesis report. Cambridge University Press, Cambridge, UK.

Jacobson, M.Z. 2005. Fundamentals of atmospheric modeling. Cambridge University Press, New York.

Kaimal, J.C., and Finnigan, J.J. 1994. Atmospheric boundary layer flows: Their structure and measurement. Oxford University Press, New York.

Kirschke, S., Bousquet, P., Ciais, P., et al. 2013. Three decades of methane sources and sinks: Budgets and variations. *Nature Geoscience*.

Kljun, N., Calanca, P., Rotach, M., et al. 2004. A simple parameterisation for flux footprint predictions. *Boundary-Layer Meteorology* **112**(3): 503-523.

Kormann, R., and Meixner, F.X. 2001. An analytical footprint model for non-neutral stratification. *Boundary-Layer Meteorology* **99**(2): 207-224.

Lamb, B.K., McManus, J.B., Shorter, J.H., et al. 1995. Development of atmospheric tracer methods to measure methane emissions from natural gas facilities and urban areas. *Environmental Science & Technology* **29**(6): 1468-1479.

Laubach, J., and Kelliher, F.M. 2004. Measuring methane emission rates of a dairy cow herd by two micrometeorological techniques. *Agricultural and Forest Meteorology* **125**(3): 279-303.

- Lenschow, D.H. 2012. Atmospheric boundary layer. *In* Encyclopedia of Global Warming and Climate Change. Sage Publications.
- LI-COR Inc. 2012. Estimating the flux footprint. [http://envsupport.Licor.Com/help/eddypro3/content/topics/estimating\\_flux\\_footprint.Htm](http://envsupport.Licor.Com/help/eddypro3/content/topics/estimating_flux_footprint.Htm) (retrieved as of dec. 5, 2013).
- Mahzabin, T. 2012. Quantifying methane emission from surface sources using the backward lagrangian stochastic method. Master's Thesis, Department of Earth and Atmospheric Sciences, University of Alberta, Edmonton.
- Park, K.-H., Wagner-Riddle, C., and Gordon, R.J. 2010. Comparing methane fluxes from stored liquid manure using micrometeorological mass balance and floating chamber methods. *Agricultural and Forest Meteorology* **150**(2): 175-181.
- Rose, A.J. 2003. Development of an ammonia emission protocol and preliminary emission factor for a central texas dairy. Master's Thesis, Biological and Agricultural Engineering, Texas A&M University.
- Rumsey, I. 2004. An assessment of ammonia emissions from water-holding structures for hog farms: Lagoon and spray technology and potential environmentally superior technologies. Master's Thesis, Department of Marine, Earth and Atmospheric Sciences, North Carolina State University.
- Russwurm, G.M., and Childers, J.W. 2002. Open-path fourier transform infrared spectroscopy. *In* Handbook of vibrational spectroscopy. John Wiley & Sons, Ltd.
- Schmid, H. 1994. Source areas for scalars and scalar fluxes. *Boundary-Layer Meteorology* **67**(3): 293-318.
- Schuepp, P., Leclerc, M., MacPherson, J., et al. 1990. Footprint prediction of scalar fluxes from analytical solutions of the diffusion equation. *Boundary-Layer Meteorology* **50**(1-4): 355-373.
- Sommer, S.G., and Hutchings, N. 2001. Ammonia emission from field applied manure and its reduction—invited paper. *European Journal of Agronomy* **15**(1): 1-15.
- Stull, R.B. 1988. An introduction to boundary layer meteorology. Kluwer Academic Publishers, AH Dordrecht, The Netherlands.
- Turner, D.B. 1970. Workbook of atmospheric dispersion estimates. US Department of Health, Education, and Welfare, National Center for Air Pollution Control.

- U.S. EPA. 1999. Ft-ir open-path monitoring guidance document [3rd edition]. ManTech Environmental Technology, Inc., Research Triangle Park, NC.
- U.S. EPA. 1999a. Compendium method to-16: Long-path open-path fourier transform infrared monitoring of atmospheric gases. Cincinnati, OH.
- U.S. EPA. 2010. Methane and nitrous oxide emissions from natural sources. [Http://www.Epa.Gov/outreach/pdfs/methane-and-nitrous-oxide-emissions-from-natural-sources.Pdf](http://www.Epa.Gov/outreach/pdfs/methane-and-nitrous-oxide-emissions-from-natural-sources.Pdf) (retrived as of nov. 1, 2013).
- U.S. EPA. 2012. Inventory of u.S. Greenhouse gas emissions and sinks: 1990-2010. [Http://www.Epa.Gov/climatechange/ghgemissions/usinventoryreport/archive.html](http://www.Epa.Gov/climatechange/ghgemissions/usinventoryreport/archive.html) (retrived as of nov. 2013).
- Warneck, P. 1999. Chemistry of the natural atmosphere. Academic Press Inc., San Diego.
- Webb, E.K., Pearman, G.I., and Leuning, R. 1980. Correction of flux measurements for density effects due to heat and water vapour transfer. Quarterly Journal of the Royal Meteorological Society **106**(447): 85-100.
- Wilson, J. 2008. Monin-obukhov functions for standard deviations of velocity. Boundary-Layer Meteorology **129**(3): 353-369.
- Wilson, J., Thurtell, G., Kidd, G., et al. 1982. Estimation of the rate of gaseous mass transfer from a surface source plot to the atmosphere. Atmospheric Environment (1967) **16**(8): 1861-1867.
- Wyngaard, J.C., and Moeng, C.-H. 1992. Parameterizing turbulent diffusion through the joint probability density. Boundary-Layer Meteorology **60**(1-2): 1-13.
- Yusuf, R.O., Noor, Z.Z., Abba, A.H., et al. 2012. Greenhouse gas emissions: Quantifying methane emissions from livestock. American Journal of Engineering and Applied Sciences **5**(1): 1-8.
- Zahn, J., Tung, A., Roberts, B., et al. 2001. Abatement of ammonia and hydrogen sulfide emissions from a swine lagoon using a polymer biocover. Journal of the Air & Waste Management Association **51**(4): 562-573.

## Appendix A The Parameterized Scalar Flux-source Area

### Model

As stated in Schmid (1994), for unstable stratification, to determine the dimensions of the 50% source area isopleth, the following equation should be used:

$$D_N = \alpha_1 \frac{z_m^{\alpha_2}}{z_0} \left(1 - \alpha_3 \frac{z_m}{L}\right)^{\alpha_4} \left(\frac{\sigma_v}{u_*}\right)^{\alpha_5}$$

For stable stratification, the equation is:

$$D_N = \alpha_1 \left(\frac{z_m}{z_0}\right)^{\alpha_2} \exp\left[\alpha_3 \left(\frac{z_m}{L}\right)^{\alpha_4}\right] \left(\frac{\sigma_v}{u_*}\right)^{\alpha_5}$$

where  $D_N$  is the normalized dimension of the bounding isopleth,  $z_m$  is the measurement height,  $L$  is the Obukhov length,  $\sigma_v$  is the standard deviation of the lateral wind fluctuations,  $u_*$  is the friction velocity, and the parameter values  $\alpha_1$  through  $\alpha_5$  are given as normalized dimensions in Tables A-1 and A-2. In the Tables, “a” is the distance to the downwind edge of the isopleth, “e” is the distance to the upwind edge of the isopleth, “d” is the maximum width of the isopleth, “ $x_d$ ” is the distance to the point where the isopleth has the biggest width, “ $x_m$ ” is the distance to the location with maximum source strength, and  $A_r$  is the area of the isopleth.

Table A-1 Values of parameters used for the passive scalar flux-source area model under unstable stratification in Schmid (1994)

<b>Unstable</b>	<b><math>\alpha_1</math></b>	<b><math>\alpha_2</math></b>	<b><math>\alpha_3</math></b>	<b><math>\alpha_4</math></b>	<b><math>\alpha_5</math></b>
a/z <sub>0</sub>	2.79	1.11	14.1	-0.399	0
e/z <sub>0</sub>	8.54	1.11	12.8	-0.39	0
d/z <sub>0</sub>	3.25	0.832	28.2	-0.272	1
x <sub>d</sub> /z <sub>0</sub>	4.29	1.15	10.3	-0.408	0
x <sub>m</sub> /z <sub>0</sub>	1.72	1.24	8.65	-0.746	0
Ar/z <sub>0</sub> <sup>2</sup>	31.4	1.93	17.8	-0.642	1

Table A-2 Values of parameters used for the passive scalar flux source area model under stable stratification in Schmid (1994)

<b>Stable</b>	<b><math>\alpha_1</math></b>	<b><math>\alpha_2</math></b>	<b><math>\alpha_3</math></b>	<b><math>\alpha_4</math></b>	<b><math>\alpha_5</math></b>
a/z <sub>0</sub>	3.28	1.09	3.53	1.05	0
e/z <sub>0</sub>	10.1	1.08	3.84	1.07	0
d/z <sub>0</sub>	4.07	0.79	2.97	0.977	1
x <sub>d</sub> /z <sub>0</sub>	4.84	1.13	3.83	1.1	0
x <sub>m</sub> /z <sub>0</sub>	1.58	1.25	2.91	1.02	0
Ar/z <sub>0</sub> <sup>2</sup>	51.3	1.86	7.29	1.05	1

## Appendix B Models Used for Calculating 90% Fetches

A footprint estimation is provided in EddyPro according to the “simple footprint parameterization” described in Kljun et al. (2004), according to LI-COR Inc. (2012). The following equations are used to calculate the set of distances.

$$\text{Peak contributing distance (m): } X_{peak} = X_{peak}^* h_m \left( \frac{\sigma_w}{u_*} \right)^{-0.8}, X^* = c - d$$

$$\text{NN\% contribution (m): } X_{NN\%} = X_{NN\%}^* h_m \left( \frac{\sigma_w}{u_*} \right)^{-0.8}, X_{NN\%}^* = L'_{NN\%} \cdot c - d$$

In the above equations, the parameters c and d are calculated using the following equations provided by Kljun et al. (2004).

$$a \approx \frac{A_F}{(B - \ln z_0)}$$

$$\exp(b) b^{-b} \Gamma(b) = \frac{1}{ac} \approx \frac{1}{A_F A_C} \approx \text{constant}$$

$$c \approx A_C (B - \ln z_0)$$

$$d \approx A_D (B - \ln z_0)$$

Where  $A_F$ ,  $B$ ,  $A_C$ , and  $A_D$  are constant parameters provided in Kljun et al. (2004).

The applicable micrometeorological conditions are specified in Kljun et al. (2004):

- The measurement height is larger than 1 m (LI-COR Inc. 2012);
- The measurement height is lower than the boundary layer height;
- The terrain is dynamically homogeneous;
- The stability parameter is in the range of  $-200 < z/L < 1$ ;
- The friction velocity is larger than a specific threshold:  $u_* \geq 0.2$  m/s.

EddyPro checks for the last three conditions and uses the model given by Kormann and Meixner (2001) if either condition is not met.

The footprint model from Kormann and Meixner (2001) is a cross-wind integrated model using the dimensional advection-diffusion equation for power-law profiles in wind velocity and eddy diffusivity (LI-COR Inc. 2012). The equation used for calculating footprint is given as follows.

$$f_x = \frac{1}{\Gamma(\mu)} \frac{\xi^\mu}{x^{1+\mu}} e^{-\xi/x}$$

Where  $x$  is the distance from the location of the anemometer,  $\xi$  is a flux length scale as a function of the height above ground  $z$ ,  $\mu$  is a dimensionless model constant and  $\Gamma(\mu)$  is the gamma function (LI-COR Inc. 2012). To calculate the peak distance, the following equation should be used.

$$X_{peak} = \frac{\xi}{1 + \mu}$$

## Appendix C OP-FTIR Operating Procedure in Field

(1) Deploy the OP-FTIR system at the site. Fill in LN2 before power on: use ~200 mL to cool down the dewar for 2 minutes, then fill in another ~200 mL; refill the dewar using ~200 mL when LN2 is running out or the dewar is hot (every 8 to 12 hours); shut down the OP-FTIR before refill. Allow the system to warm up for 30 to 60 minutes.

(2) Align the OP-FTIR system through RMMSOft (Version 6.1.3; ITT Corp.) to get maximum return signal strength.

(3) Check the nonlinear response of the system using the single beam spectrum in step (2): for wavenumber region  $650\text{-}680\text{ cm}^{-1}$ , check whether there is a dip, or for wavenumbers below 650, check whether the baseline is above zero (U.S. EPA 1999a). If yes, the system's response might be non-linear.

(4) Perform a Noise Equivalent Absorption (NEA) test. For wavenumber region  $968\text{ to }1008\text{ cm}^{-1}$ , reference average NEA =  $900\text{ }\mu\text{Au}$ .

(5) Determine (e.g. using a laser range finder) and record the pathlength of the OP-FTIR system.

(6) Collect sample spectra. Typically, in RMMSOft, 26 was chosen as the co-add number of scans to form one spectrum (it takes about 1 min to collect each spectrum).

(7) Determine and record the geographic coordinates of the IR sensor and retro-reflector.

(8) Post-measurements analysis review of data.

- Target gas concentration vs. time. Check for unexpected trends.
- Target gas concentration vs. water vapor concentration. Check for correlation.
- One target gas concentration (e.g. CO<sub>2</sub>) vs. another. Check if the gas concentrations are expected to be correlated to each other.
- Analyze the spectra for N<sub>2</sub>O (315 ppb +/- 10%, or 282~387 ppb).
- Errors calculated by Classical Least Square (CLS). Watch for abrupt changes.

## **Appendix D Steps for OP-FTIR Data Processing Using GRAMS/AI and RMMSoft**

(1) Average the spectra collected during a certain time period. Use the averaged spectrum as a background to perform a routine analysis to select the cleanest spectra in a data set (say, data points collected within a 2-hour period). Check the curvature of the baseline to determine if the selected spectra are valid for being used to create a synthetic background spectrum for the data set.

(2) Open RMMSoft, average the signal spectra selected in step 1) by “tools\_create spectrum file\_select single beam\_ select signal file\_choose coadd\_select output file/directory”.

(3) Open the file in step 1) using GRAMS/AI and then click applications\_utilites\_zap. Zap out all of the absorbance features within required wavenumber ranges (typical ranges are 700-1200, 2030-2223 and 2500-3100) of the spectrum. Caution must be taken in order to avoid distortions of the baseline of the spectrum.

(4) Produce a water vapor reference (absorbance) spectrum by following the steps listed in Section 8.5 of Compendium Method TO-16 (U.S. EPA 1999a). Specify the path of the newly produced spectrum in SPI.

(5) Use the synthetic background generated in step 2), the preliminary SPI, as well as the water vapor reference spectrum in step 3) to analyze the signal spectra.

(6) Based on the results in step 4), confirm the presence of each analyte by examining the single beam/absorbance spectra for each analyte by comparing

each absorbance spectrum to the specific reference spectrum using GRAMS/AI. Also, look for possible extra analytes that are present in the plume but not included in the preliminary SPI by examining the Spectral Library Search results and the single beam spectra. Any extra analyte found should be included in refining SPI file in next step. In addition, clean air single-beam spectra and zero-path single-beam spectra can be used for comparison to identify any analytes that are not common in clean air.

(7) According to the analytes confirmed in step 5), refine the preliminary SPI by adding necessary interferences and then re-analyze the signal spectra to get final concentration results for each confirmed analyte. Repeat any previous steps if necessary. To refine a SPI file, pick one analyte in the confirmed analyte list and then compare, using GRAMS/AI, the reference spectrum of this analyte with reference spectra of other analytes in the list, one by one, to identify any interferences that have overlapping (interfering) absorbance features over the specific analysis region. Interferences should be added into the SPI file in RMMSoft.

## Appendix E Detailed Quality Control/Assurance

### Information for OP-FTIR

As mentioned in Section 3.1.4, more detailed quality control/assurance information is given as follows:

- Perform NEA noise tests regularly. For wavenumber region 968 to 1008  $\text{cm}^{-1}$ , reference average NEA = 900  $\mu\text{Au}$ . The expected absorbance at site should be more than 4 times the NEA
- Check the return beam intensity, at least once every day. Path length, water vapor and other atmospheric conditions (fog, rain, pollen, etc.) may affect the intensity. Watch for unacceptable degradation of the return beam signal intensity. Try to maintain the return beam strength at about 10 volts (by changing the gain or path length, if necessary)
- Watch for sudden change of detection limits ( $3\sigma$ , RMMSoft: window-analysis results-concentrations-text)
- Check the nonlinear instrument response. Reasons for nonlinear instrument response may include a) too large gain, A/D converter saturated; b) light source too intense, too many photons to be converted to electrical signal at the same time. In everyday operation, the easiest way to detect the second kind of nonlinearity is to examine the portion of the single beam spectrum at wavenumbers below the detector cutoff. This is in the 650-680  $\text{cm}^{-1}$  region for most HgCdTe detectors. If a dip below zero

occurs in that region or if the signal is above zero at wavenumbers below that region, the system's response may be nonlinear

- Look for unexpected chemical compounds during the data acquisition phase. These compounds must be accounted for in the analysis for the most accurate data (U.S. EPA 1999a)
- Carefully rinse the retro-reflector with distilled water if the signal is reduced by more than 35%.

## **Appendix F VBA Code for Filtering Wind Directions and Removing “Errors”**

The VBA code used in this study for removing unfavorable wind directions and instrument output “Errors” are provided below. A screenshot of a Microsoft™ EXCEL document outputted by EddyPro is also given as Figure F-1 to help with understanding the code.

```
Sub main()  
  
Dim i As Integer  
  
For i = 4 To 4000 'user input, row 4 to row the last  
  
If Sheet1.Cells(i, "BM") >= 175.1 And Sheet1.Cells(i, "BM") <= 355.1 Then 'user  
input, orientation of sonic + 90 or 270 degree  
  
Sheet1.Rows(i).Delete  
  
i = i - 1  
  
ElseIf Sheet1.Cells(i, "A") = "not_enough_data" Then  
  
Sheet1.Rows(i).Delete  
  
i = i - 1  
  
ElseIf Sheet1.Cells(i, "N") = "Error" Then  
  
Sheet1.Rows(i).Delete  
  
i = i - 1  
  
ElseIf Sheet1.Cells(i, "R") = "Error" Then  
  
Sheet1.Rows(i).Delete
```

$i = i - 1$

End If

Next

End Sub

A8		not_enough_data																		
A	B	C	D	E	F	G	H	I	J	BM	BN	BO	BP	BQ	BR	BS	BT	BU	BV	BW
file_info	filename	time	DOY	daytime	file_recor	used_recc	qc_Tau	corrected_fluxes_and_quality	H	wind_dir	rotation_angles_for_yaw	pitch	roll	u*	TKE	L	(z-d)/L	bowen_raT*		footpr
[#]	[#]	[#]	[#]	[#]	[#]	[#]	[#]	[#]	[#]	[#]	[#]	[#]	[#]	[#]	[#]	[#]	[#]	[#]	[#]	[#]
1	not_enou	14:30	169.604	Error	Error	Error	Error	Error	Error	Error	Error	Error	Error	Error	Error	Error	Error	Error	Error	Error
2	not_enou	15:00	169.624	T	18000	17144	0.104497	1	-5.17874	65.57121	19.52879	3.55176	Error	0.306723	0.523635	465.5566	4.80E-03	-4.12E-02	-1.50E-02	kljun
3	not_enou	15:30	169.645	T	18000	16861	5.39E-02	2	-3.23406	70.35364	14.74636	3.223788	Error	0.220294	0.324338	276.198	8.09E-03	-3.88E-02	-1.30E-02	kljun
4	not_enou	16:00	169.666	T	18000	16982	3.80E-02	1	-5.50708	67.10997	17.99003	2.696024	Error	0.184707	0.221203	95.60175	2.34E-02	-6.15E-02	-2.64E-02	korma
5	not_enou	16:30	169.687	Error	Error	Error	Error	Error	Error	Error	Error	Error	Error	Error	Error	Error	Error	Error	Error	Error
6	not_enou	17:00	169.708	Error	Error	Error	Error	Error	Error	Error	Error	Error	Error	Error	Error	Error	Error	Error	Error	Error
7	not_enou	17:30	169.729	Error	Error	Error	Error	Error	Error	Error	Error	Error	Error	Error	Error	Error	Error	Error	Error	Error
8	not_enou	18:00	169.749	Error	Error	Error	Error	Error	Error	Error	Error	Error	Error	Error	Error	Error	Error	Error	Error	Error
9	not_enou	18:30	169.77	Error	Error	Error	Error	Error	Error	Error	Error	Error	Error	Error	Error	Error	Error	Error	Error	Error
10	not_enou	19:00	169.791	Error	Error	Error	Error	Error	Error	Error	Error	Error	Error	Error	Error	Error	Error	Error	Error	Error
11	not_enou	21:00	186.874	F	18000	17736	6.95E-02	2	13.35193	345.6454	99.45461	-1.62738	Error	0.249849	0.449406	-97.4246	-2.29E-02	0.121236	4.73E-02	kljun
12	not_enou	21:30	186.895	F	18000	18000	4.54E-02	2	3.456237	349.2792	95.82083	-0.83808	Error	0.201849	0.268645	-198.417	-1.13E-02	5.81E-02	1.52E-02	kljun
13	not_enou	22:00	186.916	F	18000	18000	4.71E-02	1	-8.93703	294.7335	150.3665	13.2965	Error	0.205176	0.186876	80.6001	2.77E-02	-7.88E-02	-3.84E-02	kljun
14	not_enou	22:30	186.937	F	18000	18000	0.274745	1	91.59774	6.220238	78.87976	23.21009	Error	0.494842	0.403467	-110.38	-2.02E-02	-0.29364	0.162652	kljun
15	not_enou	23:00	186.958	F	18000	18000	1.31E-02	2	-3.58237	239.6326	205.4674	4.236888	Error	0.108032	0.217489	29.37379	7.60E-02	-0.12131	-2.91E-02	korma
16	not_enou	23:30	186.979	F	18000	18000	2.31E-02	2	-7.75232	295.0969	150.0031	1.667686	Error	0.143117	0.285746	31.55801	7.08E-02	-0.43572	-4.75E-02	korma
17	not_enou	0:00	187	F	18000	18000	3.75E-02	2	-14.8214	296.8925	148.2075	1.306948	Error	0.182398	0.309056	34.17599	6.53E-02	-0.77842	-7.11E-02	korma
18	not_enou	0:30	187.02	F	18000	18000	2.78E-02	2	-10.3993	307.5119	137.5881	2.213916	Error	0.156794	0.243533	30.94462	7.22E-02	-0.65104	-5.79E-02	korma
19	not_enou	1:00	187.041	F	18000	18000	2.51E-02	2	-9.83204	296.0485	149.0515	1.327903	Error	0.148833	0.278462	27.9938	7.98E-02	-0.75082	-5.76E-02	korma
20	not_enou	1:30	187.062	F	18000	18000	4.06E-02	2	-8.72638	294.1981	150.9019	1.637935	Error	0.189508	0.408036	65.11642	3.43E-02	-0.70523	-4.01E-02	korma
21	not_enou	2:00	187.083	F	18000	18000	6.35E-02	2	-11.1266	302.2252	142.8748	1.877593	Error	0.236634	0.690144	99.42493	2.25E-02	-0.52509	-4.10E-02	kljun
22	not_enou	2:30	187.104	F	18000	18000	5.28E-02	2	-7.57125	305.1445	139.9555	1.781362	Error	0.21567	0.50619	110.635	2.02E-02	-0.35473	-3.05E-02	kljun

Figure F-1 A screenshot of an EddyPro output document

## Appendix G VBA Code for Calculating 50% Source

The VBA code for calculating 50% sources using equations given by Schmid (1994) is provided as follows. A screenshot of layout of the data in an Microsoft™ EXCEL document is given as Figure G-1 to help understanding of the code.

```
Sub main()  
Dim i, j As Integer  
For i = 3 To 1333  
If Sheet1.Cells(i, "e") < 0 Then  
    k = 11  
    For j = 2 To 7  
        a1 = Sheet2.Cells(j, "b")  
        a2 = Sheet2.Cells(j, "c")  
        a3 = Sheet2.Cells(j, "d")  
        a4 = Sheet2.Cells(j, "e")  
        a5 = Sheet2.Cells(j, "f")  
        dn = a1 * (Sheet1.Cells(i, "h") / Sheet1.Cells(i, "i")) ^ a2 * (1 - a3 *  
Sheet1.Cells(i, "h") / Sheet1.Cells(i, "e")) ^ a4 * (Sheet1.Cells(i, "g") /  
Sheet1.Cells(i, "d")) ^ a5  
        Sheet1.Cells(i, k) = dn  
        k = k + 1  
    End For  
End If  
End For  
End Sub
```

```

Next
ElseIf Sheet1.Cells(i, "e") > 0 Then
    k = 11
    For j = 2 To 7
        a1 = Sheet2.Cells(j, "i")
        a2 = Sheet2.Cells(j, "j")
        a3 = Sheet2.Cells(j, "k")
        a4 = Sheet2.Cells(j, "l")
        a5 = Sheet2.Cells(j, "m")
        dn = a1 * (Sheet1.Cells(i, "h") / Sheet1.Cells(i, "i")) ^ a2 * Exp(a3 *
(Sheet1.Cells(i, "h") / Sheet1.Cells(i, "e")) ^ a4) * (Sheet1.Cells(i, "g") /
Sheet1.Cells(i, "d")) ^ a5
        Sheet1.Cells(i, k) = dn
        k = k + 1
    Next
End If
Next
End Sub

```

N1335																				
A	B	C	D	E	F	G	H	I	J	K	L	M	N	O	P	Q	R	S	T	
1	date	time	DOY	u*	L	v_var	Sigma v	z0		a/z0	e/z0	d/z0	xd/z0	xm/z0	Ar/z0	a	e	d	xd	
2	[YYYY-mm-dd]	[HH:MM]	[ddd.ddd]	[m+1s-1]	[m]	[m+2s-2]	m/s													
3	06/18/2013	15:00	169.624	0.306723	465.5566	0.466201	0.682789	2.24	0.0015	9579.733	27411.54	2963.024	18894.52	14853.14	94027484	14.3696	41.1173	4.444537	28.3417	
4	06/18/2013	15:30	169.645	0.220294	276.198	0.232882	0.482578	2.24	0.0015	9671.146	27673.63	2947.334	19053.63	14985.17	94362048	14.50672	41.51045	4.421	28.5804	
5	06/18/2013	16:00	169.666	0.184707	95.60175	0.175019	0.418353	2.24	0.0015	10126.94	29003.9	3200.26	19880.09	15625.1	1.07E+08	15.19041	43.50585	4.80039	29.8201	
6	06/23/2013	9:00	174.374	9.76E-02	-1.78061	0.143618	0.37897	2.24	0.0015	2891.375	9416.307	2075.789	6541.213	2342.207	21546327	4.337063	14.12446	3.113684	9.8118	
7	06/23/2013	9:30	174.395	0.165997	-8.82582	0.265323	0.515095	2.24	0.0015	5073.25	16208.92	2492.467	11351.97	6238.92	43514336	7.609875	24.31338	3.7387	17.0279	
8	06/23/2013	10:00	174.416	0.154708	-6.47977	0.51835	0.719965	2.24	0.0015	4593.105	14735.36	3467.797	10324.19	5286.139	55240476	6.889658	22.10304	5.201696	15.4862	
9	06/23/2013	10:30	174.437	0.126543	-3.8597	0.279773	0.528936	2.24	0.0015	3843.148	12408.76	2733.686	8679.684	3889.553	36931238	5.764722	18.61313	4.100529	13.0195	
10	06/23/2013	14:00	174.583	0.193017	-5.84106	0.509508	0.713798	2.24	0.0015	4436.663	14252.47	2685.743	9984.808	4984.498	41435562	6.654995	21.3787	4.028614	14.9772	
11	06/23/2013	14:30	174.604	0.191041	-5.93037	0.694864	0.833585	2.24	0.0015	4459.365	14322.62	3180.893	10034.18	5027.967	49306588	6.689047	21.48393	4.77134	15.0512	
12	06/23/2013	15:00	174.624	0.185545	-5.51712	0.937365	0.968176	2.24	0.0015	4351.871	13990.18	3735.993	9800.005	4823.087	56620494	6.527807	20.98527	5.60399	14.7000	
1325	09/11/2013	22:00	254.916	0.15965	23.41387	0.109497	0.330903	2.24	0.0015	12768.3	36964.73	3663.992	24973.95	19130.06	1.58E+08	19.15246	55.4471	5.495988	37.4609	
1326	09/11/2013	22:30	254.937	0.124132	24.81767	6.45E-02	0.254018	2.24	0.0015	12542.9	36275.26	3557.951	24528.99	18839.28	1.51E+08	18.81435	54.41289	5.336926	36.7934	
1327	09/11/2013	23:00	254.958	0.134927	19.01812	0.215611	0.464339	2.24	0.0015	13739.09	39950.44	6508.73	26904.8	20369.14	3.06E+08	20.60863	59.92565	9.763095	40.357	
1328	09/11/2013	23:30	254.979	0.160919	30.08645	0.138455	0.372095	2.24	0.0015	11910.83	34350.31	3829.756	23289.08	18016.98	1.53E+08	17.86625	51.52546	5.744633	34.9336	
1329	09/12/2013	0:00	255	0.116822	28.63536	6.41E-02	0.253216	2.24	0.0015	12058.19	34797.93	3631.909	23577.05	18209.64	1.47E+08	18.08729	52.1969	5.447863	35.3655	
1330	09/12/2013	0:30	255.02	8.76E-02	13.21274	0.101344	0.318346	2.24	0.0015	16350.85	48096.19	8044.544	32194.33	23612.25	4.63E+08	24.52627	72.14428	12.06682	48.2914	
1331	09/12/2013	1:00	255.041	0.144515	197.2366	0.103614	0.321892	2.24	0.0015	9763.89	27941.78	3028.391	19218.27	15117.37	97856113	14.64584	41.91268	4.542587	28.827	
1332	09/12/2013	3:00	255.124	0.13795	24.54506	4.85E-02	0.220325	2.24	0.0015	12584.3	36401.79	2785.457	24610.62	18892.78	1.19E+08	18.87645	54.60269	4.178186	36.9159	
1333	09/12/2013	3:30	255.145	7.81E-02	12.62784	7.07E-02	0.265886	2.24	0.0015	16792.7	49488.65	7718.405	33100.76	24149.67	4.59E+08	25.18904	74.23298	11.57761	49.6511	
1334																1.817266	6.046831	1.079454	4.0598	
1335																10728624	1.48E+08	500830.6	1.77E+0	
1336																12.05989	37.45451	5.143583	25.6480	
1337																				

Figure G-1 A screenshot of the layout of the data for calculating 50% source area